



Manipulating the Structural and Electronic Properties of Epitaxial NaNbO_3 Films via Strain and Stoichiometry

Inaugural-Dissertation

zur

Erlangung des Doktorgrades

der Mathematisch-Naturwissenschaftlichen Fakultät

der Universität zu Köln

vorgelegt von

Biya Cai

aus Yiyang, PR China

Jülich, 2016

Berichtersteller: Prof. Dr. Roger Wördenweber

Prof. Dr. Markus Grüninger

Tag der mündlichen Prüfung: Nov. 04, 2016

Abstract

Due to their intriguing dielectric, pyroelectric, elasto-electric, or opto-electric properties, oxide ferroelectrics are vital candidates for the fabrication of most electronics. However, these extraordinary properties exist mainly in the temperature regime around the ferroelectric phase transition, which is usually several hundreds of K away from room temperature. Therefore, the manipulation of oxide ferroelectrics, especially moving the ferroelectric transition towards room temperature, is of great interest for application and also basic research.

In this thesis, we demonstrate this using examples of NaNbO_3 films. We show that the transition temperature of these films can be modified via plastic strain caused by epitaxial film growth on a structurally mismatched substrate, and this strain can be fixed by controlling the stoichiometry.

The structural and electronic properties of $\text{Na}_{1+x}\text{NbO}_{3+\delta}$ thin films are carefully examined by among others XRD (e.g. RSM) and TEM and cryoelectronic measurements. Especially the electronic features are carefully analyzed via specially developed interdigitated electrodes in combination with integrated temperature sensor and heater. The electronic data are interpreted using existing as well as novel theories and models, they are proved to be closely correlated to the structural characteristics. The major results are:

- $\text{Na}_{1+x}\text{NbO}_{3+\delta}$ thin films can be grown epitaxially on $(110)\text{NdGaO}_3$ with a thickness up to 140 nm (thicker films have not been studied). Plastic relaxation of the compressive strain sets in when the thickness of the film exceeds approximately 10 – 15 nm. Films with excess Na are mainly composed of NaNbO_3 with minor contribution of Na_3NbO_4 . The latter phase seems to form nanoprecipitates that are homogeneously distributed in the NaNbO_3 film which helps to stabilize the film and reduce the relaxation of the strain.
- For the nominally stoichiometric films, the compressive strain leads to a broad and frequency-dispersive phase transition at lower temperature (125 – 147 K). This could be either a new transition or a shift in temperature of a known transition. Considering the broadness and frequency dispersion of the transition, this is actually a transition from the dielectric state at high temperature to a relaxor-type ferroelectric state at low temperature. The latter is based on the formation of polar nano-regions (PNRs). Using the electric field dependence of the freezing temperature, allows a direct estimation of the volume (70 to 270 nm³) and diameter (5.2 to 8 nm, spherical approximation) of the PNRs. The values confirm with literature values which were measured by other technologies.

-
- In case of the off-stoichiometric samples, we observe again the classical ferroelectric behavior. However, the thermally hysteretic phase transition which is observed around 620 – 660 K for unstrained material is shifted to room temperature due to the compressive strain. Beside to the temperature shift, the temperature dependence of the permittivity is nearly identical for strained and unstrained materials.
 - The last but not least, in all cases, a significant anisotropy in the electronic and structural properties is observed which arises automatically from the anisotropic strain caused by the orthorhombic structure of the substrate. However, this anisotropy cannot be explained by the classical model which tries to fit an orthorhombic film onto an orthorhombic substrate. A novel “square lattice” model in which the films adapt a “square” shaped lattice in the plane of the film during the epitaxial growth at elevated temperature (~1000 K) nicely explains the experimental results.

In this thesis we sketch a way to manipulate the ferroelectricity of NaNbO_3 films via strain and stoichiometry. The results indicate that compressive strain which is generated by the epitaxial growth of the film on mismatched substrate is able to reduce the ferroelectric transition temperature or induce a phase transition at low temperature. Moreover, by adding Na in the NaNbO_3 film a secondary phase Na_3NbO_4 is formed which seems to stabilize the main phase NaNbO_3 and the strain and, thus, is able to engineer the ferroelectric behavior from the expected classical ferroelectric for perfect stoichiometry to relaxor-type ferroelectric for slightly off-stoichiometry, back to classical ferroelectric for larger off-stoichiometry. Both strain and stoichiometry are proven as perfect methods to optimize the ferroelectric properties of oxide films.

Zusammenfassung

Auf Grund ihrer einzigartigen dielektrischen, pyroelektrischen, elastoelektrischen und auch optoelektrischen Eigenschaften sind oxydische Ferroelektrika essentielle Kandidaten für die Herstellung elektrischer Bauelemente. Allerdings werden die optimalen Eigenschaften hauptsächlich im Bereich des ferroelektrischen Phasenüberganges erreicht, der jedoch üblicherweise einige hundert Kelvin oberhalb der Arbeitstemperatur (Raumtemperatur) dieser Bauelemente liegt. Daher ist es von hohem Interesse die Materialien so zu verändern, dass deren Übergangstemperaturen in den Bereich der Raumtemperatur verschoben werden.

In dieser Arbeit wird dies an Hand des Beispiels von epitaktischen NaNbO_3 -Schichten demonstriert. Die Übergangstemperatur wird mittel mechanischer Verspannung durch das Aufwachsen der Schicht auf strukturell fehlangepasste Substrate modifiziert. Zusätzlich wird durch Stöchiometrieänderung diese Verspannung fixiert.

Es werden in dieser Arbeit sowohl die strukturellen als auch elektronischen Eigenschaften von $\text{Na}_{1+x}\text{NbO}_{3+\delta}$ -Schichten auf $(110)\text{NdGaO}_3$ -Substraten mittels Röntgen (u.a. RSM), TEM bzw. kryoelektronischen Messungen analysiert. Insbesondere durch die Entwicklung spezieller interdigitalen Elektrodenstrukturen, integrierten Temperatursensoren und Heizer ist es möglich, die elektronischen Eigenschaften genauestens zu bestimmen und mit den strukturellen Eigenschaften zu korrelieren. Die Hauptergebnisse der Arbeit sind:

- Die $\text{Na}_{1+x}\text{NbO}_{3+\delta}$ -Schichten wachsen bis zu eine Dicke von 140nm (dickere Schichten wurden nicht untersucht) epitaktisch und daher verspannt auf den $(110)\text{NdGaO}_3$ -Substraten auf. Ab einer Dicke von ca. 10 – 15 nm setzt allerdings schon eine plastische Relaxation der Verspannung ein. Durch die Zugabe von Na wächst zusätzlich zur Hauptphase NaNbO_3 eine zweite Phase, $\text{Na}_3\text{NbO}_{3+\delta}$. Diese scheint in Form von Nanopräzipitaten zu wachsen, die gleichmäßig verteilt die Verspannung der Hauptphase stabilisieren kann.
- Die nominell stöchiometrischen Proben zeigen einen breiten, frequenzdispersiven Übergang bei niedrigen Temperaturen (125 – 147 K). Dies kann sowohl ein neuer Phasenübergang sein als auch ein bekannter Phasenübergang, der durch die kompressive Verspannung zu niedrigeren Temperaturen verschoben ist. Die Breite und Frequenzdispersion des Überganges weist jedoch klar auf einen Übergang vom dielektrische bei hohen Temperaturen zu einem relaxorartigen ferroelektrische Zustand bei niedrigen Temperaturen. Letzterer basiert auf der Bildung von sogenannten polaren Nanoregionen (PNR). Durch eine spezielle Kombination von frequenz- und feldabhängigen

Bestimmungen der sogenannten ‚Freezing Temperature‘, ist es gelungen die Größe (70 bis 270 nm³) und den resultierenden Durchmesser (5.2 bis 8 nm, sphärische Näherung) der PNRs zu ermitteln. Die Werte bestätigen Literaturwerte die anhand anderer Technologien ermittelt wurden.

- Im Falle der nominal nicht-stöchiometrischen Proben finden wir nun erstaunlicherweise ein klassisches Verhalten. Allerdings wird der Übergang, der für nicht verspannte Proben bei 620-650K liegt, nun durch die hohe kompressive Verspannung zur Raumtemperatur verschoben. Ansonsten ist die Temperaturabhängigkeit der Permittivität nahezu identisch zu der der unverspannten Proben.
- Letzter wichtiger Punkt ist die Anisotropie aller Eigenschaften, die automatisch durch die anisotrope Verspannung durch die orthorhombische Struktur der Substrate entsteht. Sie findet sich in den strukturellen und elektronischen Eigenschaften der Schicht wieder. Allerdings lassen sich die Verspannungen nicht mit dem klassischen Model erklären, das prinzipiell versucht, die orthorhombische Struktur des Films auf der orthorhombischen Struktur des Substrates abzubilden. Hier schlagen wir ein modifiziertes ‚Square lattice model‘ vor, das von einer quadratischen Grundfläche eine Kubischen Filmstruktur beim Aufwachsen der Schicht bei hohen Temperaturen (ca. 1000 K). Dieses Model führt zu anderen Verspannungen in der Schichtebene und erklärt die beobachtete Anisotropie der elektronischen Eigenschaften sehr gut.

In dieser Arbeit zeigen wir am Beispiel des NaNbO₃ einen Weg auf, wie die ferroelektrischen Eigenschaften von oxydischen Schichten durch Verspannung und Stöchiometrieänderungen gezielt manipuliert werden können. Die kompressive Verspannung in der Schichtebene, die durch das epitaktische Aufwachsen der Schicht auf fehlangepasste Substrate erzeugt wird, führt zu einem ferroelektrischen Phasenübergang bei niedrigen Temperaturen. Durch die Zugabe von Na wird eine zweite Phase erzeugt, die augenscheinlich die Hauptphase und deren Verspannung stabilisiert. So kann durch die Veränderung der Stöchiometrie das klassische ferroelektrische Verhalten von perfekt stöchiometrischen Filmen erst in ein relaxorartiges Verhalten bei leichter Nichtstöchiometrie und anschließend ein klassisches Verhalten allerdings mit stark veränderter Übergangstemperatur bei starker Abweichung von der Stöchiometrie erreicht werden. Verspannung und Stöchiometrieänderung erweisen sich somit als probate Mittel zur Optimierung von ferroelektrischen Eigenschaften oxydischer Schichten.

Contents

1. Introduction	1
2. Theoretical background	5
2.1. Introduction to ferroelectrics	5
2.2. Ferroelectric materials	9
2.2.1. Introduction to NaNbO ₃	10
2.3. Ferroelectric phase transitions.....	14
2.3.1. First-order and second-order phase transitions.....	14
2.3.2. Displacive and order-disorder phase transitions.....	15
2.4. Relaxor-type ferroelectrics	16
2.4.1. Vogel-Fulcher behavior.....	20
2.4.2. Lorentz fit of the phase transition.....	21
2.4.3. Models for relaxor-type ferroelectrics.....	22
2.5. Engineering of ferroelectricity	24
2.5.1. Doping.....	25
2.5.2. Strain	26
3. Sample preparation and experimental techniques	29
3.1. Sample preparation.....	29
3.1.1. Metal organic chemical vapor deposition.....	29
3.1.2. Pulsed laser deposition	31
3.1.3. Evaporation deposition.....	32
3.2. Characterization of structure and stoichiometry.....	33
3.2.1. X-ray diffraction.....	33
3.2.2. Reciprocal space mapping.....	35
3.2.3. Transmission electron microscopy	37
3.2.4. Rutherford backscattering spectrometry.....	38
3.3. Device design for the electronic characterization.....	40
3.3.1. Interdigitated electrodes	40
3.3.2. Integrated Pt temperature sensor	41
3.3.3. Integrated Pt heater.....	43
3.4. Device fabrication techniques	44
3.5. Electronic characterization.....	46

3.5.1. Experimental setup	47
3.5.2. Capacitive measurements and evaluation.....	49
4. Engineering of ferroelectric properties of NaNbO₃ via strain.....	54
4.1. Structural properties: epitaxy, strain and strain relaxation	55
4.2. Electronic properties.....	57
4.3. Anisotropy	59
4.4. Ferroelectric state	65
4.5. Summary	68
5. Relaxor behavior and polar nanoregions in strained NaNbO₃	69
5.1. Relaxor-type behavior	71
5.1.1. Vogel-Fulcher behavior.....	71
5.1.2. Lorentz fit.....	72
5.2. Electric field dependence of the permittivity	74
5.3. Polar nanoregions	76
5.4. Reversible and irreversible behavior.....	80
5.5. Summary	84
6. Stoichiometry dependence and Na₃NbO₄ nanoprecipitates.....	85
6.1. Structural properties of strained Na _{1+x} NbO _{3+δ} films.....	86
6.2. Electric properties of strained Na _{1.17} NbO _{3+δ} film	91
6.3. Rayleigh analysis of the strained Na _{1.17} NbO _{3+δ} film.....	95
6.4. Summary	98
7. Conclusions	99
References	102
Acknowledgements.....	109
Statutory declaration in lieu of an oath.....	111
CURRICULUM VITAE	112

1. Introduction

In 1919, the French scientist J. Valasek was the first to observe a dielectric and piezoelectric response of the Rochelle salt ($\text{NaKC}_4\text{H}_4\text{O}_6 \cdot 4\text{H}_2\text{O}$). He presented his observation of an anomalous hysteresis (see Fig. 1.1) at the meeting of the American Physical Society in Washington in 1920. This was the first report on 'ferroelectricity' [1].

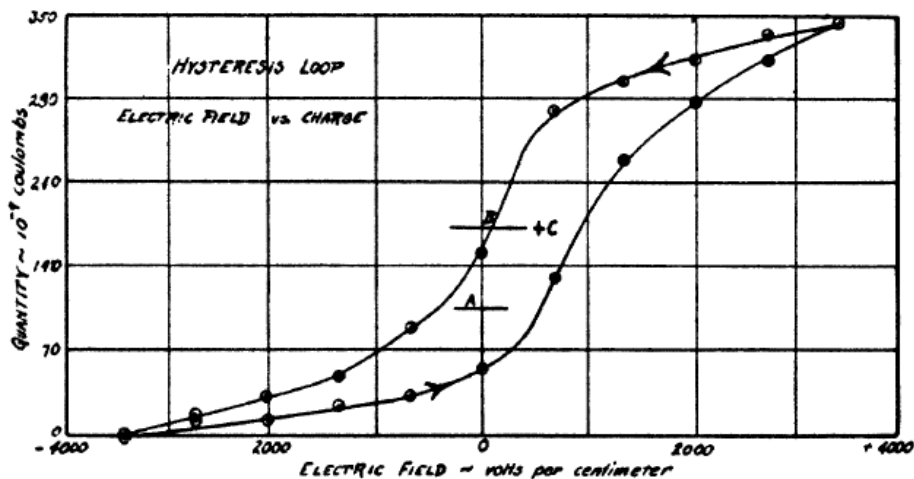


Fig. 1.1: The first published ferroelectric hysteresis by J. Valasek in Physical Review in 1921, adapted from [1].

15 years later, Busch and Scherrer discovered a new type of ferroelectric crystal, KH_2PO_4 [2]. Since then, it was thought that a hydrogen bond is necessary for a ferroelectric material until ferroelectricity was discovered in BaTiO_3 in the 1940s [3]. The simplicity of the structure (perovskite structure) and the excellence of the electronic properties of BaTiO_3 have attracted a lot of interest for academic and theoretical research as well as practical applications since then. Due to this material, ferroelectric oxides became an "electronic ceramics" for industry. Billions of BaTiO_3 "condensers" are still made annually, at a cost of less than one cent per capacitor, even including expensive Ag/Pd electrodes [4]. In the following decades, there were some breakthroughs in ferroelectrics, which mainly focused on the theoretical modelling of the description of the ferroelectricity and the discoveries of new sorts of ferroelectrics, e.g. lead zirconate titanate, lead lanthanum zirconate titanate, and lead magnesium niobate [5]. During this so-called perovskite era (1940s to 1970s), these ferroelectrics were widely used for the fabrication of actuators, piezoelectric transducers and pyroelectric detectors. The

application to sonar was especially well funded. However, these ferroelectrics used for fabrication of devices were restricted to bulk ceramics [4]. The miniaturization became available with the development of the thin film technology in the late 1970s. Since this time, various ferroelectrics, e.g. BaTiO_3 , $(\text{Ba}_x\text{Sr}_{1-x})\text{TiO}_3$, $\text{Pb}(\text{Zr}_x\text{Ti}_{1-x})\text{O}_3$ (PZT), La-doped PZT, Nb-doped PZT, Sn-doped PZT, Ba-doped PZT, PbTiO_3 , BiTiO_3 , LiNbO_3 , and KNbO_3 , can be produced in the form of thin films with a good quality via different preparation techniques.

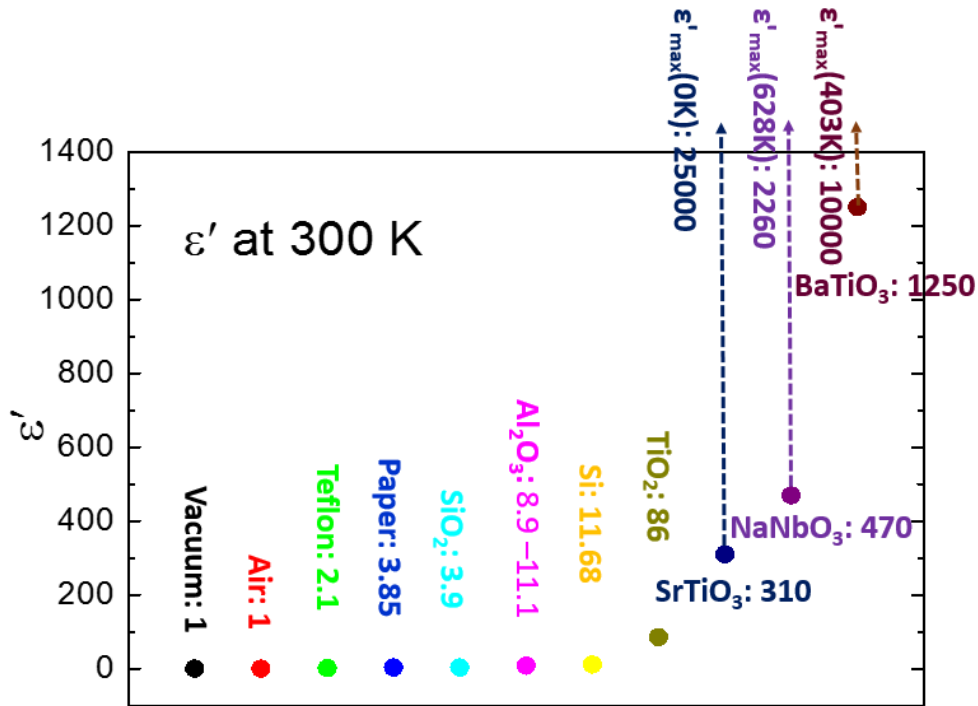


Fig. 1.2: Permittivity of various materials at room temperature, however the maximum permittivity for a number of ferroelectric oxides, e.g. SrTiO_3 , NaNbO_3 and BaTiO_3 , is obtained at temperatures close to the phase transitions far from room temperature.

The next step in this development is the engineering of the properties of these thin film ferroelectrics. This is actually the issue of today. On the one hand, it is known that extreme ferroelectric properties (e.g. permittivity of several thousands) can be obtained in some oxide materials (see Fig. 1.2). However these properties are typically only present at temperatures close to the ferroelectric phase transition which are typically far from room temperature. On the other hand, sophisticated deposition techniques are available that allow to produce “single crystalline” (i.e. epitaxy) films of well defined composition. These techniques might allow to engineer those oxides to achieve ferroelectric thin films with superior properties at

operating temperature (in the ideal case, room temperature). This engineering of the ferroelectric properties can be achieved by chemical doping or mechanical strain. Both options lead, among others, to a modification of the lattice parameters and, therefore, the electronic properties of these materials.

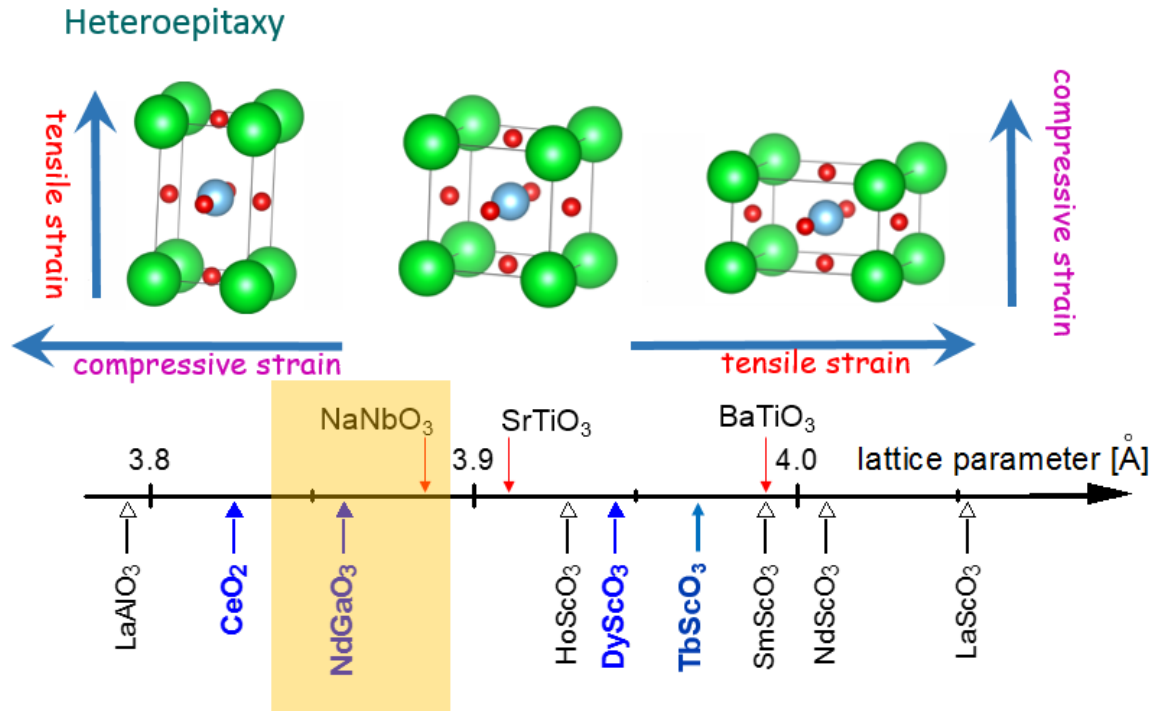


Fig. 1.3: Schematic illustration of the impact of in-plane strain originated by the mismatch of the lattice parameters between film and substrate on the modification of the structure for heteroepitaxial growth of the film. The axis represents the lattice parameter for different candidates for the film (upper) and substrate (lower), respectively.

In case of heteroepitaxial growth of the film, the use of strain provided by the lattice mismatch between substrate and film (see Fig. 1.3) has lately proven to be a very successful tool to modify the ferroelectric properties of oxide film [6-13]. According to the theoretical predictions of Pertsev et al. [14,15], an in-plane tensile strain will enhance the transition temperature along the in-plane direction, whereas an in-plane compressive strain will enhance the transition temperature along the out-of-plane direction. Based on the Poisson effect, these in-plane strain either tensile or compressive will automatically generate an out-of-plane strain with opposite directions (see Fig. 1.3). Since Pertsev et al. only predicted an enhancement of the transition temperature (for the direction of tensile strain) and since the transition temperature is far above room temperature for nearly all technical relevant oxides,

the question arose for us that can we reduce the phase transition temperature to lower temperature by a compressive strain? In order to test this hypothesis, we chose the technically very interesting oxide NaNbO_3 . In bulk form, this system shows the best ferroelectric properties (e.g. permittivity of $\epsilon' \approx 2260$) at temperature around a ferroelectric phase transition around 630 K [16,17]. We grow NaNbO_3 epitaxially on NdGaO_3 . Due to the lattice mismatch a compressive strain is generated at the interface between the film and the substrate (see Fig. 1.3).

In this thesis, we therefore examine and discuss the following issues:

- (i) Does NaNbO_3 grow epitaxially on NdGaO_3 ? And if it does, are the resulting films strained, how are they strained, and does the strain relax with the thickness of the film?
- (ii) How does the strain (and the strain relaxation) affect the ferroelectric properties of the NaNbO_3 film? Especially, can we reduce the temperature of the ferroelectric phase transition or can we induce phase transition at lower temperature via compressive strain? And how does this affect the permittivity and type of ferroelectric behaviors.
- (iii) Does an anisotropic strain lead to anisotropic electronic properties in these NaNbO_3 thin films?
- (iv) What happens, if we, additionally to the strain, change the stoichiometry of the films?

These different questions will be discussed in this thesis. After this introduction, the theoretical background is sketched in Chapter 2. The sample preparation and experimental techniques are introduced in Chapter 3. The following Chapters 4, 5, and 6 concentrate on the experimental results regarding the questions presented in this introduction. At last, the conclusions of this thesis are given in Chapter 7.

2. Theoretical background

In this chapter, ferroelectricity, the classification of ferroelectric materials, ferroelectric phase transitions, and relaxor-type ferroelectrics are introduced. The corresponding theories are sketched, the ferroelectric candidate NaNbO_3 , which is the system examined in this thesis, is shown, and methods for the engineering of ferroelectricity are discussed.

2.1. Introduction to ferroelectrics

In the presence of an applied electric field, each insulator can be electronically polarized, the polarization can be expressed as,

$$P = \varepsilon_0(\varepsilon' - 1)E \quad (2.1)$$

where ε_0 is the permittivity of vacuum, and the parameter ε' is the real part of the dielectric constant,

$$\varepsilon = \varepsilon' + i\varepsilon'' \quad (2.2)$$

where ε' is also called permittivity, which characterizes the polarizability of a material, and ε'' is the imaginary part of dielectric constant, which represents the loss (dissipation) of energy in the material.

Basically there are four different kinds of mechanisms of polarization: electronic, orientation, ionic, and space charge polarization. An applied external electric field with sufficient amplitude is able to not only shift the negatively charged electron cloud or ionic lattice against the positively charged nucleus (electronic polarization) or ionic lattice (ionic polarization), but also reorient the dipoles (orientation polarization) or trapped charged space (space charge polarization) along the direction of the electric field (see Fig. 2.1).

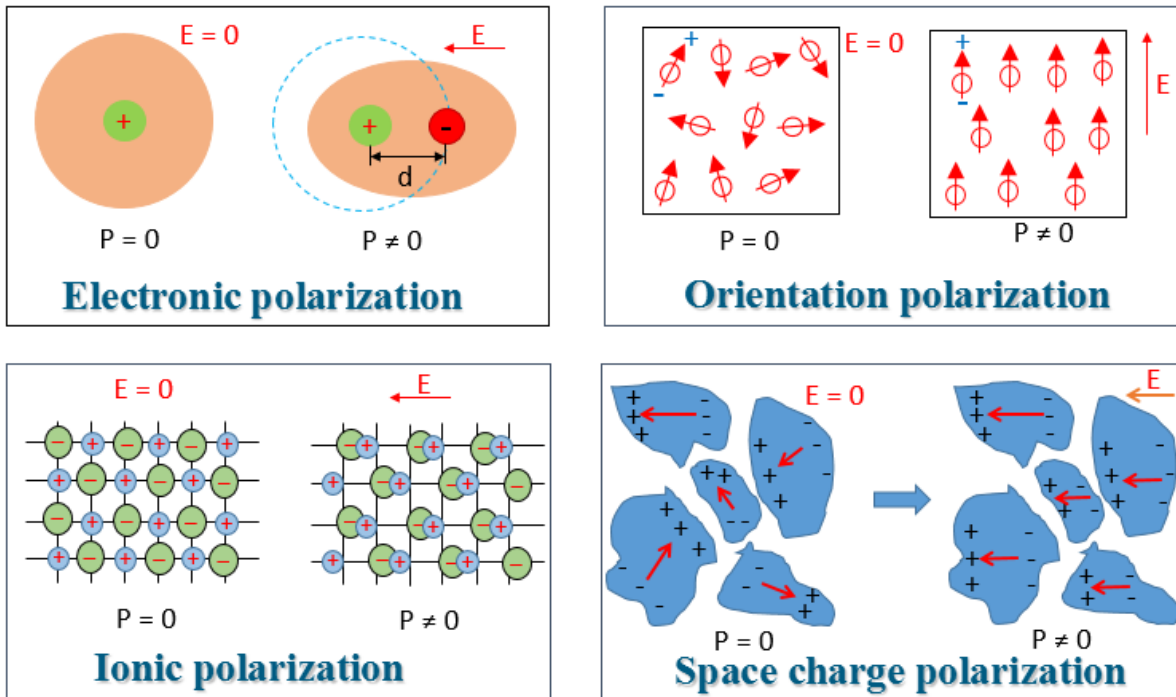


Fig. 2.1: Schematic illustrations of electronic, orientation, ionic, and space charge polarization mechanisms.

These four mechanisms can for instance be distinguished by their reactions to an applied electric field [18]. Fig. 2.2 shows the specific dielectric contributions from different mechanisms. The space charge polarization only contributes at low frequency regime (i.e. 1 – 10 KHz), orientation and ionic polarization fail to follow when the frequency is beyond 100 MHz and 1 THz, respectively, and only electronic polarization is valid at the optical frequency regime. In this thesis, we later discuss the impact of so-called polar nano-regions (PNRs) that are the basis of relaxor-type ferroelectrics. The contribution of PNRs in relaxor-type ferroelectric is typically active in the frequency regime up to MHz (dash line). The peaks in the imaginary part of dielectric constant ϵ'' indicate the changes of the polarization mechanism.

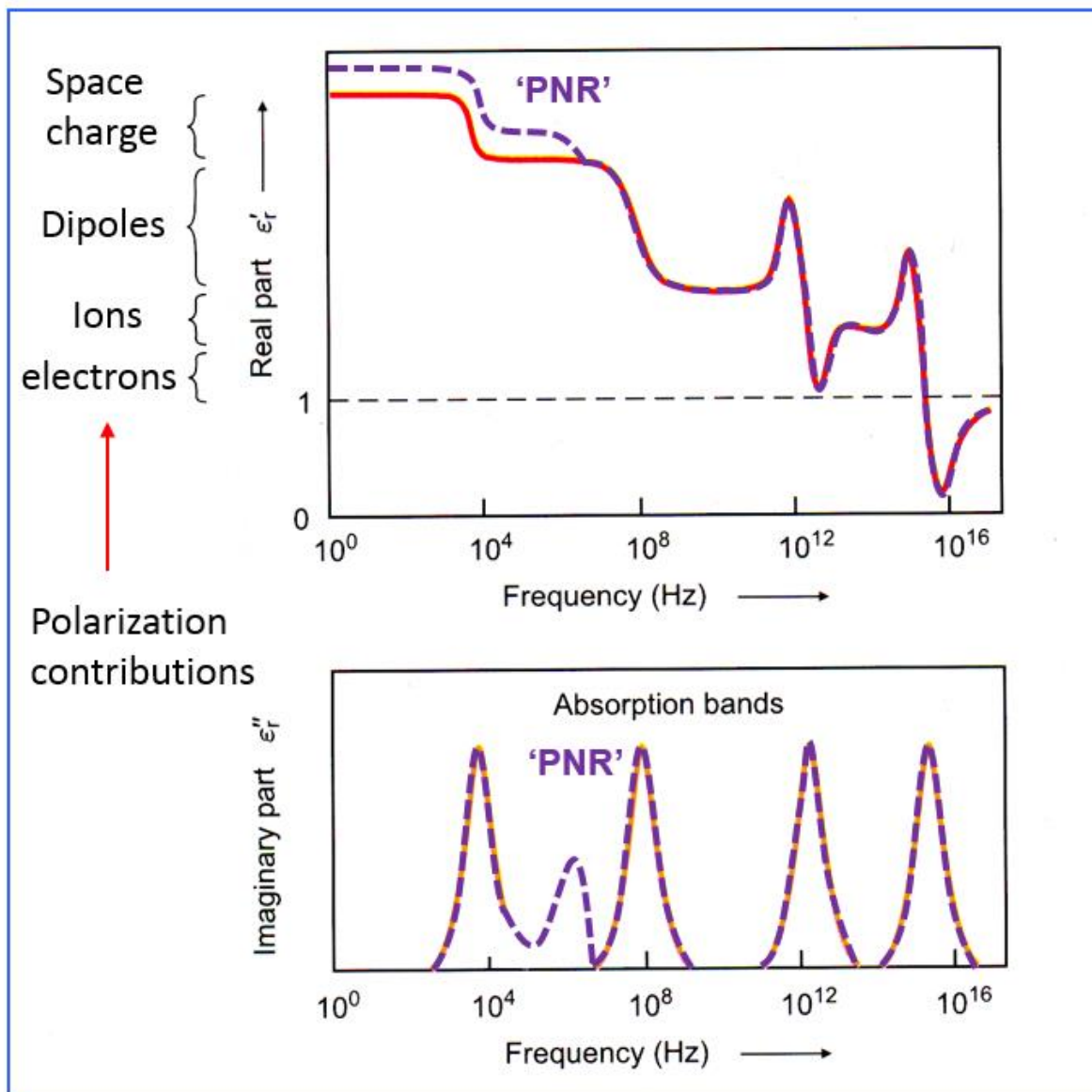


Fig. 2.2: Frequency dependence of the real part ϵ'_r and imaginary part ϵ''_r of the dielectric constant for different polarization mechanisms without (solid) and with (dash) the contribution from polar nano-regions (PNRs). Adapted from [18].

A typical ferroelectric owns a variety of possible mechanisms that induce a polarization. These are for instance:

- (i) Dielectricity: polarization induced and removed by an external electric field
- (ii) Piezoelectricity: polarization generated in response to an applied stress

-
- (iii) Pyroelectricity: polarization created by a change of temperature
 - (iv) Ferroelectricity: natural and permanent polarization (spontaneous polarization) without any external conditions

These properties are closely correlated to the crystallography structures of the material. A trivial change of the structure, or lattice parameter, will influence the internal polarization. This is, for instance, the basis for the engineering of the ferroelectric properties discussed in Chapter 2.5. Especially, the symmetry of the crystal determines the features of the crystal. Among the 32 crystalline classes, 11 classes are centrosymmetric and 21 classes are non-centrosymmetric. Only the non-centrosymmetric can show ferroelectric behavior (see Fig. 2.3).

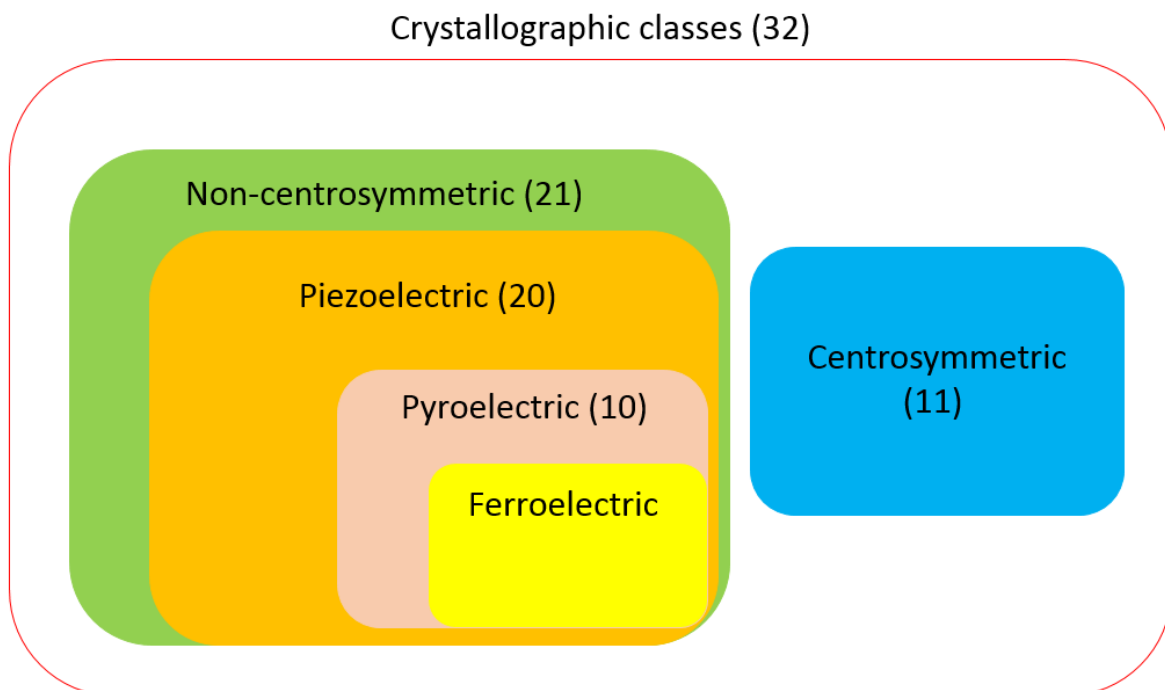


Fig. 2.3: Subordinating correlation among piezoelectric, pyroelectric, and ferroelectric material. Piezoelectricity, pyroelectricity, and ferroelectricity all require a non-centrosymmetric structure.

2.2. Ferroelectric materials

There are several methods to classify ferroelectrics, e.g. by the number of polar axes, existing form, composition, or crystalline structure. Here the main ferroelectric classes according to their crystalline structure will be introduced. Special emphasis will be given to NaNbO_3 which was used in this work. A brief summary of four types of ferroelectrics is shown in Fig. 2.4.

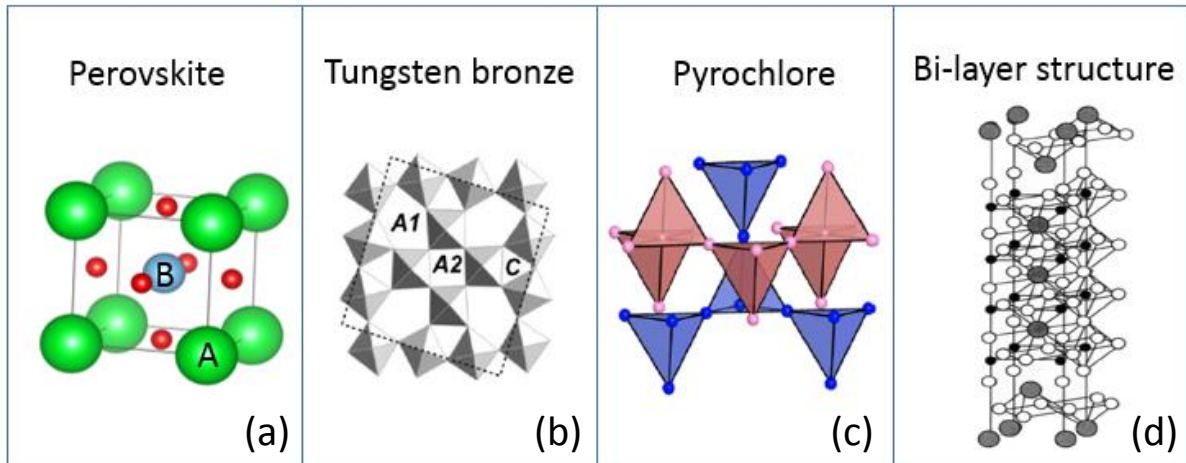


Fig. 2.4: A summary of typical types of ferroelectric materials based on the crystalline structure. (a) Perovskite ABO_3 with the B site cation (light blue) located at the center of the unit cell and surrounded by 6 oxygen (red) anions, which constructs an octahedra of BO_6 . The A site cation is situated at the corners of the unit cell. (b) Tetragonal tungsten bronze (TTB) structure along c axis. A1, A2 and C stand for pentagonal, square and trigonal tunnels, respectively. Adapted from [19]. (c) Sketch of ideal cubic pyrochlore structure which is composed of two interpenetrating corner-sharing tetrahedra lattices (oxygen atoms not shown for clarity). Pink and blue dots represent A site and B site cations, respectively. Adapted from [20]. (d) Sketch of one-half the pseudo-tetragonal unit cell of bismuth layer-structured ferroelectric (BLFS, $m=3$). Adapted from [21].

Perovskite-type ferroelectric: The perovskite represents a type of crystal with a structure of ABO_3 [22]. The perovskite-type ferroelectrics with a cubic or pseudo-cubic structure above the phase transition temperature are classified into simple form and complex form. The simple perovskite-type oxides normally have crystalline structure such as, $\text{A}^{2+}\text{B}^{4+}\text{O}_3$ or $\text{A}^{1+}\text{B}^{5+}\text{O}_3$ (Fig. 2.4(a)). Typical complex perovskite-type oxides have structures with morphotropic substitution at A or B site, for examples, $(\text{A}_1\text{A}_2)\text{BO}_3$, $\text{A}(\text{B}_1\text{B}_2)\text{O}_3$, $\text{A}(\text{B}_1\text{B}_2\text{B}_3)\text{O}_3$, or $(\text{A}_1\text{A}_2)(\text{B}_1\text{B}_2)\text{O}_3$. Ferroelectrics with a perovskite structure are for instance, i.e. CaTiO_3 , BaTiO_3 , SrTiO_3 , PbTiO_3 , LiNbO_3 , KNbO_3 , NaNbO_3 , $(\text{Ba,Sr})\text{TiO}_3$, $\text{Pb}(\text{Zr, Ti})\text{O}_3$, $\text{Pb}(\text{Mg,Nb})\text{O}_3$, and $(\text{K,Na})\text{NbO}_3$.

Tetragonal tungsten bronze-type ferroelectric: Tetragonal tungsten bronze (TTB) denotes a compound with a chemical formula like M_xWO_3 , where M is an alkali metal, e.g. K, Na, Rb, Cs, or alkaline earth metal, e.g. Ag, Ti, and $0 < x < 0.95$. The content of the M cation determines the properties of the oxides. The first TTB ferroelectric, $Pb(NO_3)_2$, was discovered in 1953 [23]. More complex TTB [24-27] consists a complex array of distorted BO_6 octahedra sharing corner in such a way that form pentagonal A1, square A2 and trigonal C interstices (see Fig. 2.4(b)), where the corresponding A site or C site cations are allowed to reside [18]. Typical examples are $Ba_2ReTi_3Nb_2O_{15}$ (Re =rare earth) [28,29] and $Ba_4Sm_2Ti_4Nb_6O_{30}$ [30].

Pyrochlore-type ferroelectric: Pyrochlore represents materials with a chemical formula of $A_2B_2O_6$ and $A_2B_2O_7$, where A and B stand for alkaline, rare-earth or transition metal element. A basic pyrochlore-type ferroelectric has a structure of both A site and B site cations tetrahedra connected in terms of corner-sharing [20] (Fig. 2.4(c)). $Y_2Nb_2O_7$, Y_2NbTiO_7 , $CaYNb_2O_7$, and La_2ScNbO_7 are examples for pyrochlore-type ferroelectrics.

Bismuth layer-structured ferroelectric: Bismuth layer-structured ferroelectrics (BLSFs) are oxides with a chemical formula $(Bi_2O_2)(A_{m-1}B_mO_{3m-1})$, where A is a mono-, di- or trivalent ion (i.e. K^+ , Ba^{2+} , Ca^{2+} , Pb^{2+} , Bi^{3+}), B is a tetra-, penta, or hexavalent ion (e.g. Ti^{4+} , Nb^{5+} , and Ta^{5+}), and m is the number of BO_6 octahedra in the pseudo-perovskite block (m varies from 1 to 5). BLSFs have typical structures which are based on corner linked pseudo-perovskite sheets (e.g. $A_{m-1}B_mO_{3m-1}^{2-}$, separated by bismuth oxide $(Bi_2O_2)^{2+}$ layers [21,31-35] (see Fig. 2.4 (d)). Typical BLSFs are $PbBi_2Nb_2O_9$, $Bi_4Ti_3O_{12}$, $PbBi_4Ti_4O_{15}$, $BaBi_4Ti_4O_{15}$, $Pb_2Bi_4Ti_5O_{18}$, and $Ba_2Bi_4Ti_5O_{18}$.

2.2.1. Introduction to $NaNbO_3$

Due to their ferroelectric and piezoelectric properties that are comparable to lead-zirconate-titanate (PZT)-based materials, alkali niobates have recently attracted significant scientific interest [36-39]. Among the family of alkali niobates, especially $NaNbO_3$ and $NaNbO_3$ -based materials proved to be very promising candidates. Not only their complexity of phase transitions [37,39,40] and their highly interesting electric behavior [9-11] are of interest, they represent also promising candidates for lead-free and therefore eco-friendly thin film applications for instance in sensor and actuator devices [36,41].

At room temperature the orthorhombic (Pbcm) unit cell lattice parameters of bulk $NaNbO_3$ are $a_{NNO} = 0.55047$ nm, $b_{NNO} = 0.55687$ nm, and $c_{NNO} = 1.5523$ nm, respectively [42](see Fig. 2.5(a)). Fig. 2.5(b) shows a comparison of the orthorhombic (solid) and pseudocubic (dash)

unit cell in the a-b plane. The epitaxial growth of NaNbO_3 can best be understood by using the pseudocubic description of the NaNbO_3 structure. In the following discussions, the symbols “o” and “pc” are used to represent orthorhombic and pseudocubic structures, respectively. The pseudocubic lattice parameters of NaNbO_3 are $a^{pc} = 0.3881 \text{ nm}$ and $b^{pc} = c^{pc} = 0.3915 \text{ nm}$ [43].

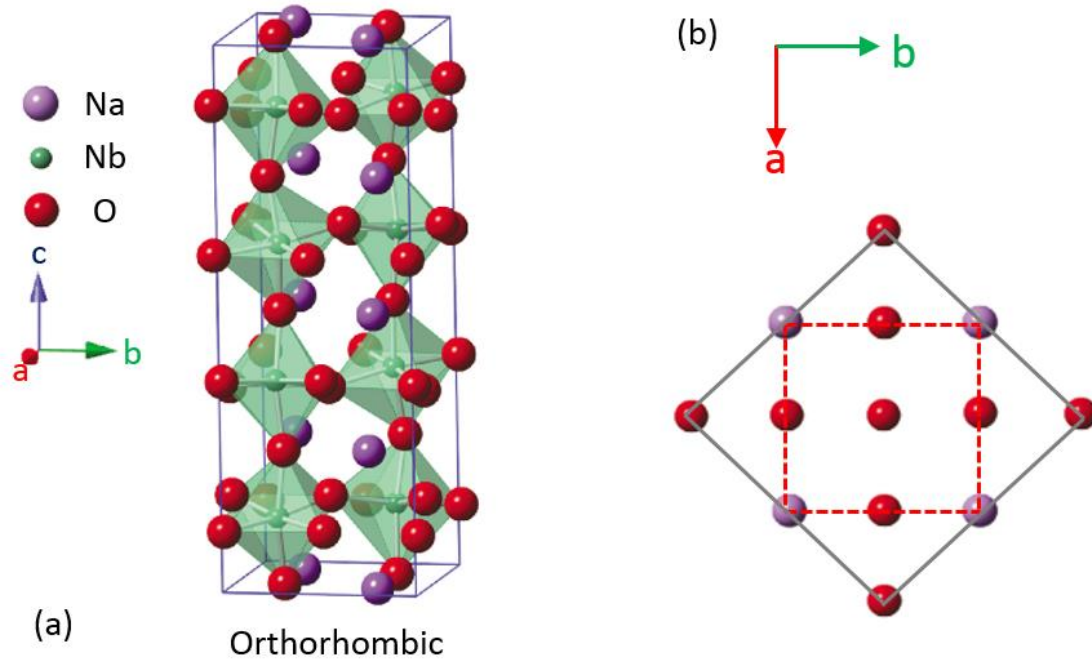


Fig. 2.5 Sketches of (a) the orthorhombic structure of bulk NaNbO_3 at room temperature (Adapted from [44]), and (b) a comparison of the orthorhombic (solid line) and pseudocubic unit cell (dash line) for the a-b plane of NaNbO_3 .

Unstrained NaNbO_3 owns 6 complex phase transitions in the temperature range from 20 K to 1000 K, which attracted a lot of scientific interests [39]. The series of the phase transitions are summarized in Fig. 2.6.

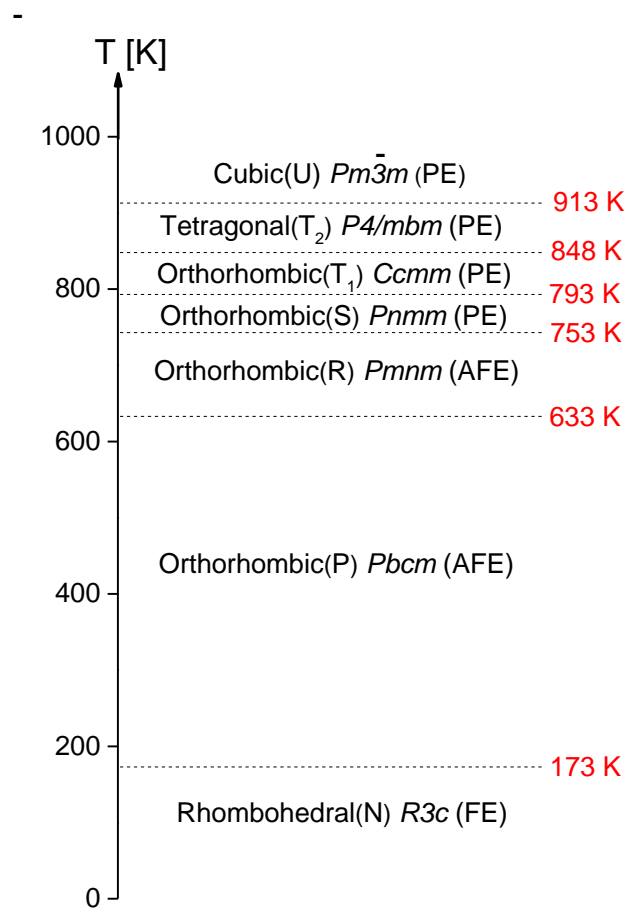


Fig. 2.6: Summary of the reported series of phase transitions of unstrained NaNbO_3 measured by XRD [39]. PE, AFE, and FE represent paraelectric, antiferroelectric, and ferroelectric, respectively.

Dielectric characterization was also applied in order to investigate the phase transition in detail. Fig. 2.7 shows a typical temperature dependence of the dielectric constant of unstrained polycrystalline NaNbO_3 [17]. Two anomalies can be observed:

- (i) a thermal hysteresis around 620 to 660 K, which is caused by a transition from the antiferroelectric P phase to the antiferroelectric R phase, and
- (ii) a small kink around 445 K, which seems to be caused by a commensurate to incommensurate phase transition in the antiferroelectric P phase.

Moreover, an applied electric field is able to induce a phase transition from the antiferroelectric to the ferroelectric state [39, 45].

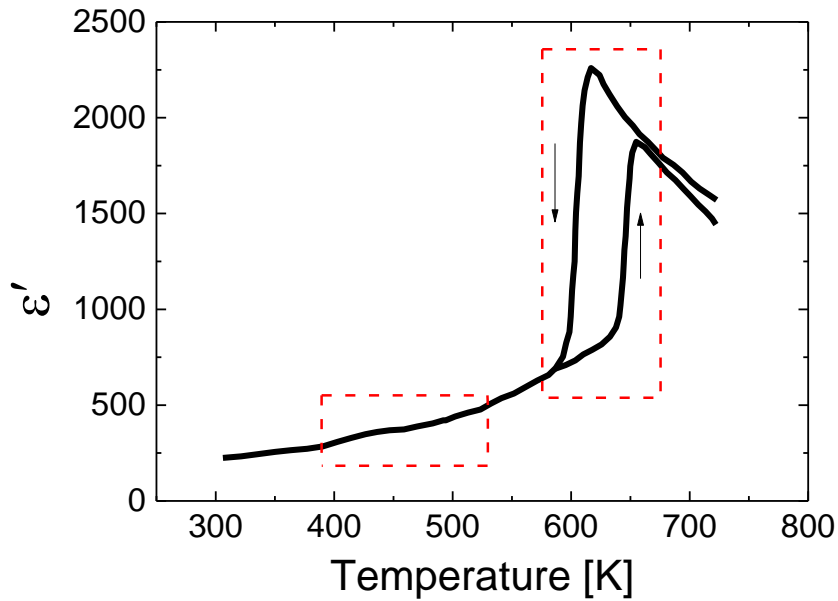


Fig. 2.7: Temperature dependence of the permittivity of unstrained polycrystalline NaNbO_3 . The boxes mark the two transitions. Adapted from [17].

The revolution from ferroelectric ceramic or crystals to thin films gives rise to the reduction of operating field and the size in device [46,47]. Although recently the growth of NaNbO_3 thin films on SrRuO_3 buffered SrTiO_3 [48,49], MgO [50], or Rh [51] or various single crystalline oxide substrates (ranging from SrLaGaO_4 , NdGaO_3 , SrTiO_3 , DyScO_3 , TbScO_3 to GdScO_3) [52] was reported, the corresponding impact of epitaxial strain on the ferroelectric properties has not been studied in detail. In this thesis, we focus on the impact of the in-plane strain, its anisotropy and relaxation, and stoichiometry dependence for epitaxially grown NaNbO_3 on $(110)\text{NdGaO}_3$.

2.3. Ferroelectric phase transitions

Generally ferroelectric phase transitions are accompanied by a structural deformation, i.e. in most cases a variation of crystalline symmetry. During this phase transition, the macroscopic and microscopic properties change a lot, e.g. extrema occur in the dielectric, pyroelectric, elasto-electric, and opto-electric properties at temperatures close to the phase transition. Therefore, this temperature regime is exceedingly interesting and practically important for applications [53]. A typical ferroelectric material will undergo a phase transition from a high-temperature dielectric (or paraelectric) state to a low-temperature ferroelectric state accompanied by a dramatic and sharp peak in the dielectric response as function of temperature.

2.3.1. First-order and second-order phase transitions

In the viewpoint of the thermodynamics, the ferroelectric phase transition can be classified into first order and second order. Based on the general definition, the order of the phase transition is determined by the discontinuity in the partial derivative of the Gibbs energy at the phase transition temperature T_C [24,54]. If the n^{th} order derivative of the Gibbs energy is discontinuous at the phase transition temperature, it is an n^{th} order phase transition [55]. In the case of a first-order ferroelectric phase transition, the spontaneous polarization P_S changes abruptly or discontinuously at T_C (Fig. 2.8(a)), whereas, it changes continuously at T_C for a second-order phase transition (Fig. 2.8(b)). In addition, a Curie-Weiss behavior is observed in the dielectric state of the ferroelectric materials according to:

$$\varepsilon' = \frac{C}{T - T_{CW}} \quad (2.3)$$

where C is the Curie constant, and T_{CW} is the Curie-Weiss temperature.

For a first-order phase transition, the Curie-Weiss temperature T_{CW} is typically smaller than T_C , whereas $T_{CW} \approx T_C$ for a second-order phase transition. BaTiO_3 and LiTaO_3 are typical ferroelectrics with a first-order and second-order phase transitions, respectively [56].

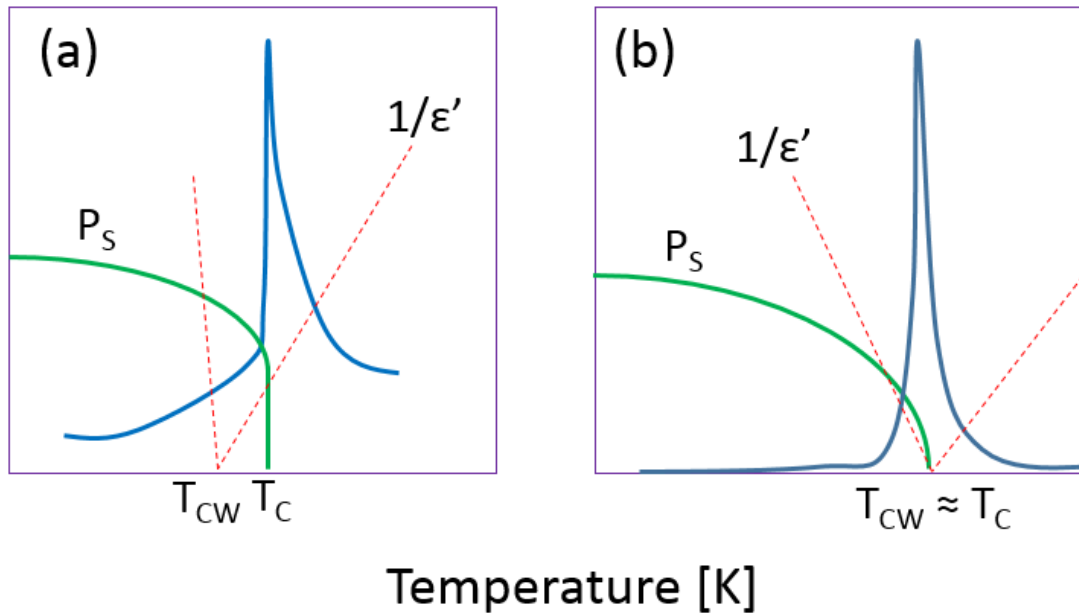


Fig. 2.8: Sketch of the spontaneous polarization and dielectric constant as function of temperature for (a) first-order and (b) second-order phase transitions.

2.3.2. Displacive and order-disorder phase transitions

With respect to their spontaneous polarization, ferroelectric phase transitions can be categorized into displacive and order-disorder phase transitions. In case of a displacive phase transition, ions start to move from their original site in the high temperature centrosymmetric structure, if the material is cooled down below T_c . In case of a perovskite (ABO_3) this could be a displacement of the B site cation from the body center position of the unit cell along the c axis. The displacement of the cations with respect to anions causes a spontaneous polarization of the displacive ferroelectric phase. $BaTiO_3$ is a typical representative of a displacive ferroelectric which has a displacive phase transition at $T_c = 393$ K [57]. In the case of order-disorder ferroelectric phase transition, certain ions are already non-uniformly arranged in the high temperature dielectric state leading to a statistically distributed local polarization with a zero total polarization at high temperature. At low temperature, the ions get ordered leading to a non-zero total polarization and, thus, a ferroelectric state. For example, $NaNO_2$ shows a typical order-disorder phase transition at $T_c = 436$ K [58].

In the microscopic view, the spontaneous polarization originates from a long-range ordering of the elementary dipole moments in the ferroelectric state. However in the high temperature dielectric state, these dipole unit cells can either disappear or distribute in a random way with

a net polarization of zero (see Fig. 2.9). According to the absence or presence of these elementary dipole moments in dielectric state, the ferroelectric phase transition in terms of displacive or order-disorder can be distinguished [24].

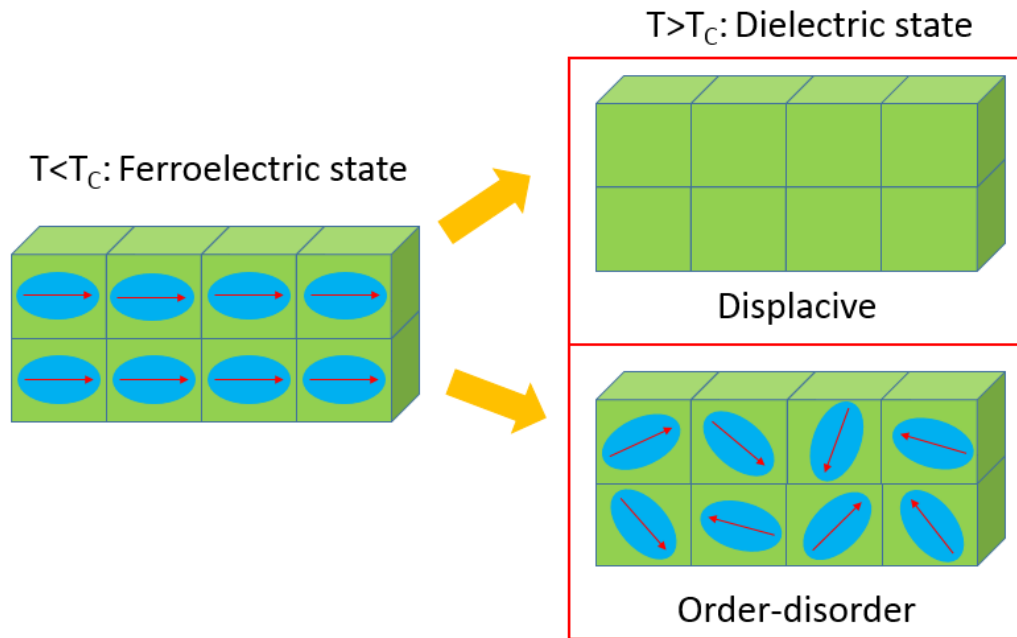


Fig. 2.9: Schematic illustrations of displacive and order-disorder ferroelectric phase transitions.

2.4. Relaxor-type ferroelectrics

Relaxor-type ferroelectricity was first discovered in the $\text{BaTiO}_3\text{-BaSnO}_3$ system in 1954 [59]. This sort of materials own peculiar features which are based on the formation of so-called polar nano-regions (PNRs) which are believed to be extended regimes of uniform polarization. The PNRs are supposed to be randomly distributed in a non-spontaneously polarized ($T_C < T < T_{\text{Burns}}$) or spontaneously polarized ($T < T_C$) matrix in relaxor-type ferroelectrics which are polarizable in the presence of an applied electric field (see Fig. 2.10). Here T_{Burns} is the Burns temperature where all the PNRs start to vanish. More details about relaxo-type ferroelectrics will be discussed in Chapter 5.

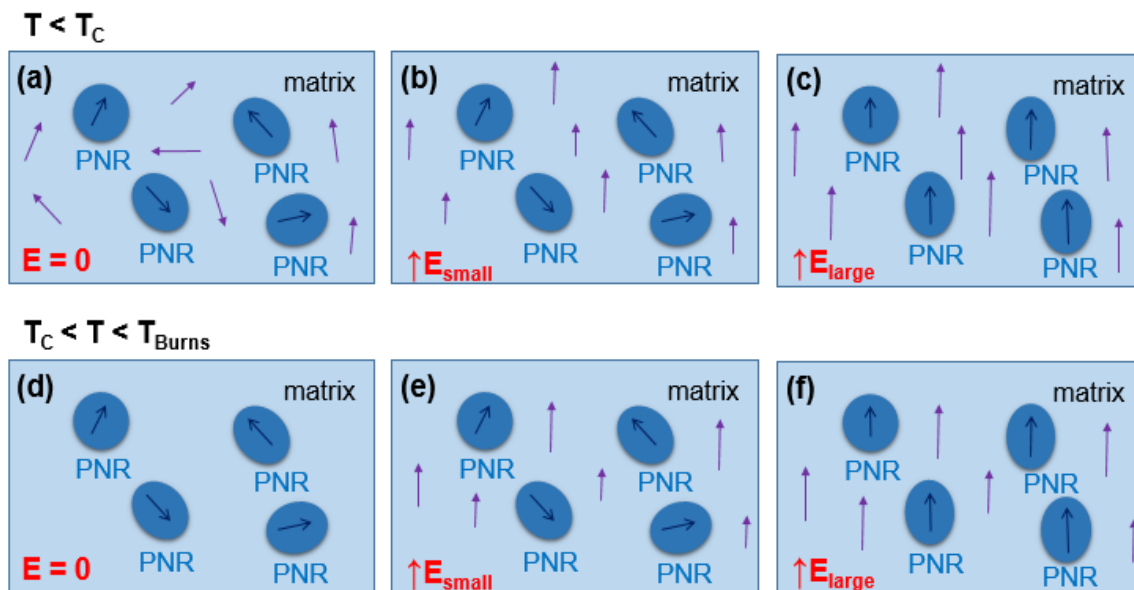


Fig. 2.10: Schematic illustration of the evolution of PNRs (blue) and matrix (light blue) for zero field ($E = 0$) and an applied electric field ($E \neq 0$) in relaxor-type ferroelectrics in the relaxor state ($T < T_C$) and in the paraelectric state below the Burns temperature ($T_C < T_{Burns}$).

As a result of the PNRs, the major differences between relaxor-type ferroelectrics and classical ferroelectrics are [60]:

- (i) Relaxor-type ferroelectrics exhibit a slim hysteresis in polarization-versus-electric field (PE) loop below the temperature T_{max} of the maximum permittivity with a small magnitude of remnant polarization P_R at zero field. This is attributed to the random distribution of PNRs. Whereas, classical ferroelectrics show a typical ferroelectric hysteresis with a large P_R which indicates the presence of the spontaneous polarization (see Fig. 2.11).

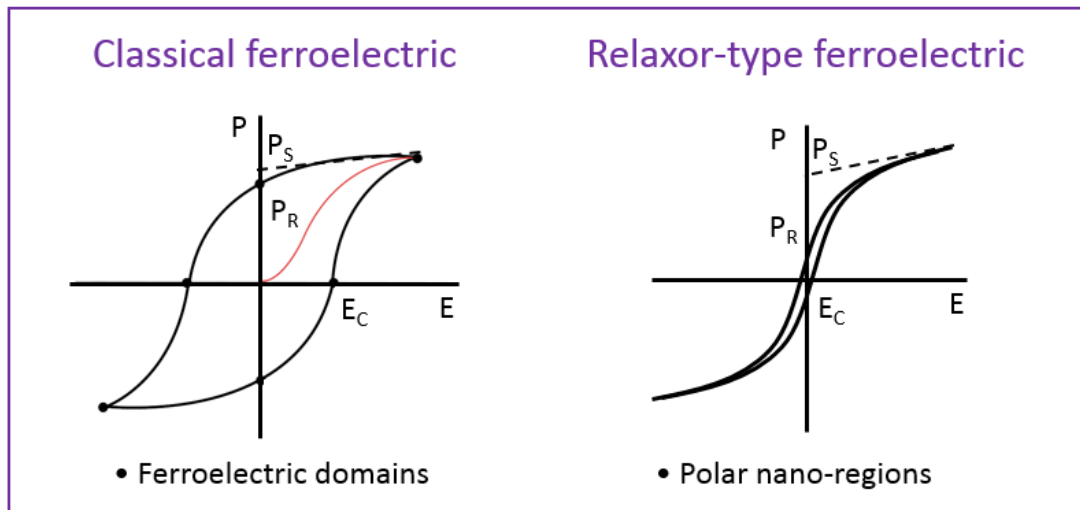


Fig. 2.11: Comparison of PE loops between classical ferroelectric and relaxor-type ferroelectric.

(ii) The polarization in relaxor-type ferroelectrics decreases smoothly with increasing temperature and shows a non-zero value above T_{max} which indicate that the PNRs persist up to the dielectric state. However, the polarization, for instance the saturation polarization (P_S) and P_R , in classical ferroelectrics dramatically decays with increasing temperature and drops down to zero at the phase transition temperature T_C . There are no ferroelectric domains existing above T_C (see Fig. 2.12).

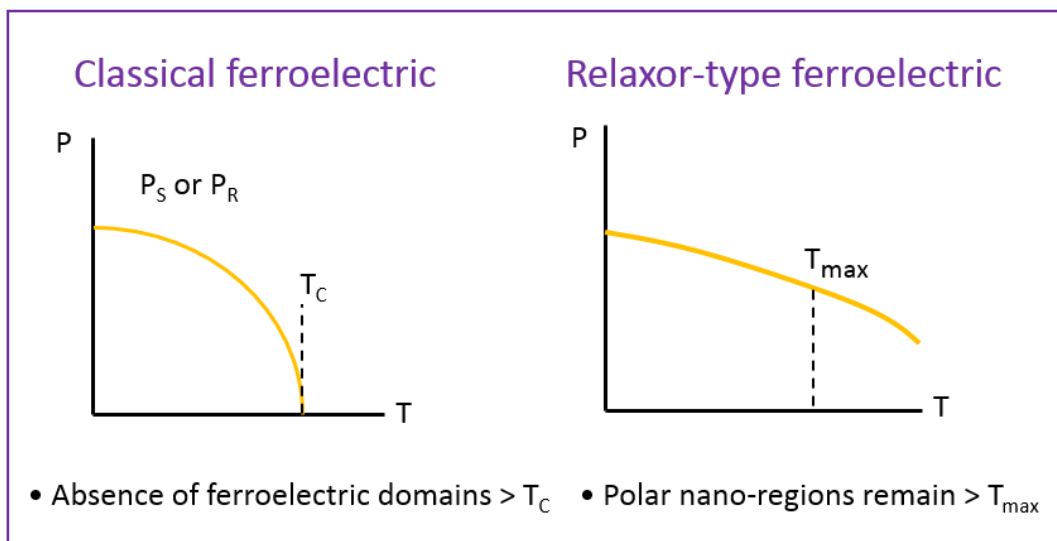


Fig. 2.12: Comparison of P-versus-T plots between classical ferroelectric and relaxor-type ferroelectric.

(iii) Relaxor-type ferroelectrics normally present a broad peak in the permittivity as function of temperature with a significant frequency dispersion. In addition, they show a deviation from the Curie-Weiss law at the so-called Burns temperature (T_{Burns}) which is several tens K higher than T_{max} . In contrast, classical ferroelectrics show a sharp and narrow peak and an abrupt decay slightly below T_C in the permittivity-versus-temperature plot in combination with no frequency dependence. Moreover, the temperature dependence of the permittivity above T_C nicely follows Curie-Weiss law (see Fig. 2.13).

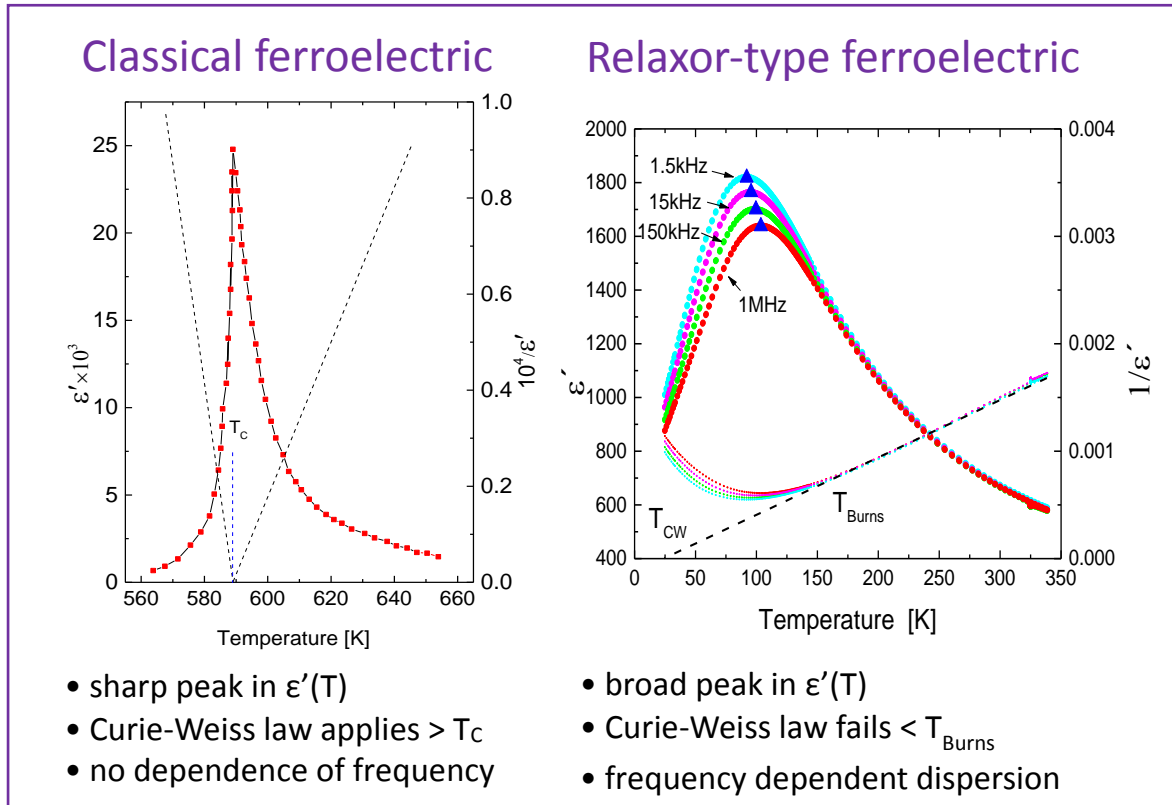


Fig. 2.13: Comparison of ϵ' -versus- T plots between classical ferroelectric and relaxor-type ferroelectric.

(iv) T_{max} in the relaxor-type ferroelectrics is not accompanied with a structural phase transition, but is an indication that the motions of dipoles are slowing down from high to low temperature. The transparent relaxors perform no difference in optical property below and above T_{max} . However, the classical ferroelectrics exhibit an obvious structural transformation, i.e. the lowering of the symmetry at T_C in a first order or second order phase transition. They present a strong optical anisotropy between the low temperature ferroelectric state and high temperature dielectric state.

2.4.1. Vogel-Fulcher behavior

The frequency dispersive behavior is the characteristic of a relaxor-type ferroelectric. A typical frequency dispersion is given in Fig. 2.14(a).

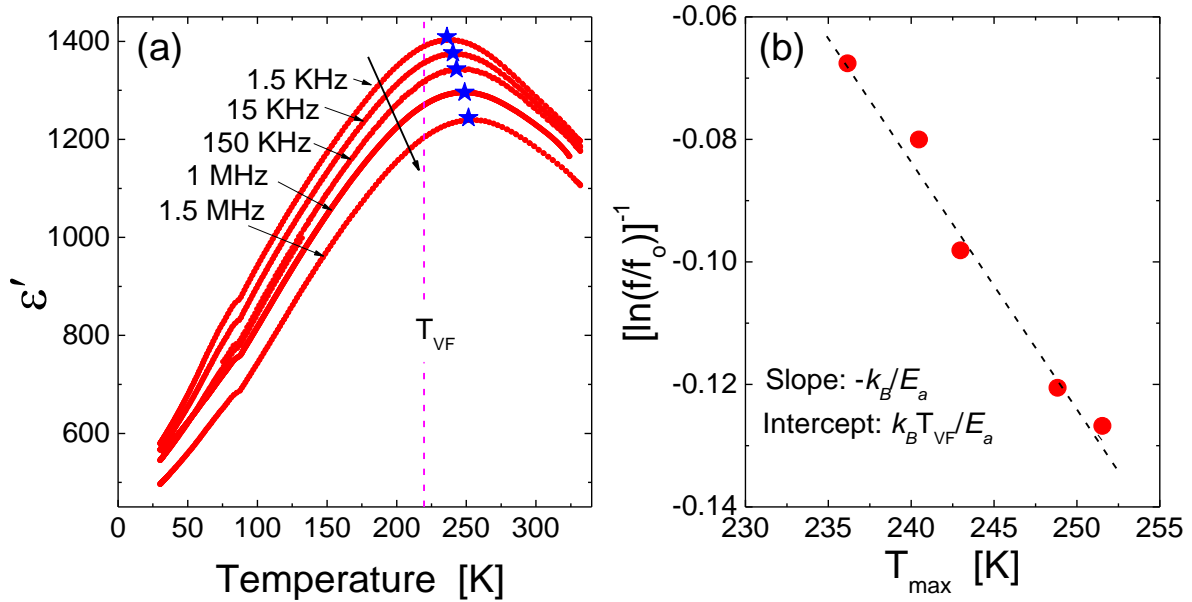


Fig. 2.14: (a) Permittivity as function of the temperature for different frequencies (1.5 kHz, 15 kHz, 150 kHz, 1 MHz, and 1.5 MHz, the direction of increasing frequency is indicated by the arrows), the maxima positions T_{\max} are marked by symbols, and (b) the resulting *Vogel-Fulcher* fits (dotted line) based on Eq. (2.5) and an attempt frequency $f_0 = 4$ GHz.

The frequency dependence of T_{\max} (temperature of the maximum permittivity) is given by the Vogel - Fulcher equation [61]:

$$f = f_0 \exp \left[- \frac{E_a}{k_B (T_{\max} - T_{VF})} \right] \quad (2.4)$$

with activation energy E_a , Vogel-Fulcher freezing temperature T_{VF} , attempt frequency f_0 , and Boltzmann constant k_B . Frequency dependent measurements of $T_{\max}(f)$ in the frequency regime up to MHz can be used to characterize the relaxor-type behavior in terms of Eq. (2.4). By inserting a reasonable value $f_0 = 4$ GHz for the attempt frequency we can extract the activation energy E_a and the freezing temperature T_{VF} from the resulting Vogel-Fulcher fit. The former describes the energy necessary for the reorientation of the polarization of the PNRs,

the latter characterizes the temperature at which the PNRs start to freeze, i.e. become immobile. Fig. 2.14(b) shows a Vogel-Fulcher analysis based on measurements performed at various frequencies (Fig. 2.14(a)). The double-logarithmic transformation of Eq. (2.4) is:

$$\left[\ln\left(\frac{f}{f_o}\right) \right]^{-1} = -\frac{k_B}{E_a} T_{\max} + \frac{k_B T_{VF}}{E_a} \quad (2.5)$$

where the slope and intercept of the double-logarithmic Vogel-Fulcher fit yield the values of $E_a = 21.2$ meV and $T_{VF} = 219.7$ K in this case.

2.4.2. Lorentz fit of the phase transition

Another important aspect of a relaxor-type ferroelectric is the broadness of the transition peak in the temperature dependence of the permittivity. This transition can generally be scaled by the empirical Lorentz relation [62],

$$\frac{\varepsilon'_{\max}}{\varepsilon'} - 1 = \frac{(T - T_{\max})^\gamma}{2\sigma^2} \quad (2.6)$$

for $T > T_{\max}$. Here ε'_{\max} is the maximum permittivity at T_{\max} , γ is the degree of the dielectric relaxation, and σ is the degree of diffuseness of the phase transition. Normally, a sharp transition peak in classical ferroelectrics is described by $\gamma = 1$. The γ values increase when the transition peak is getting broad. A relaxor-type phase transition is usually characterized by $\gamma \approx 1.5 - 2$. Fig. 2.15 shows the Lorentz equation fit based on a double-logarithmic transformation of Eq. (2.6):

$$\ln\left(\frac{\varepsilon'_{\max} - \varepsilon'}{\varepsilon'}\right) = \gamma \ln(T - T_{\max}) - \ln 2\sigma^2 \quad , \quad (2.7)$$

where the slope and intercept yield values of $\gamma = 1.82$ and $\sigma = 108.7$ K.

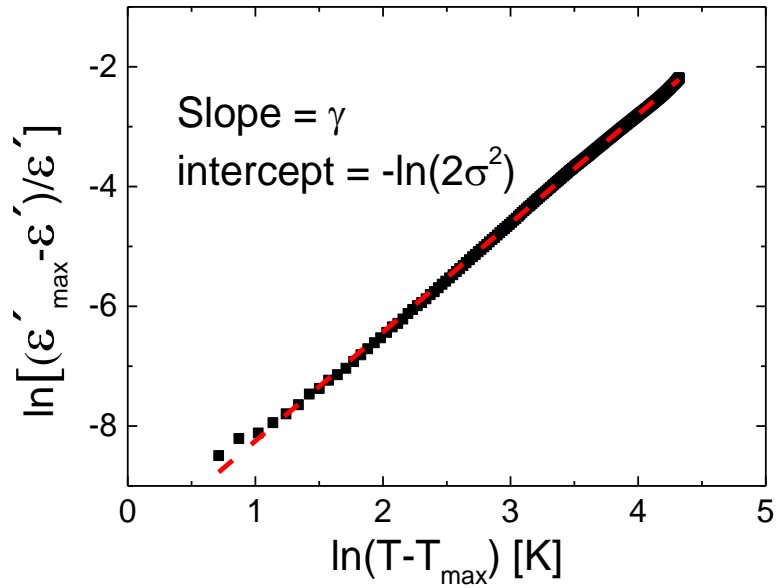


Fig. 2.15: Double logarithmic plot of the reduced and normalized permittivity as function of the reduced temperature at the phase transition ($T > T_{\max}$) for the data shown in Fig. 2.14(a). The fit (red dash line) represents the theoretic fit based on the Lorentz equation.

2.4.3. Models for relaxor-type ferroelectrics

Generally the polarization in the polar nano-regions (PNRs) which originate from a secondary phase or inhomogeneities (chemical or structural) [60,63-65] is supposed to be responsible for the relaxor behavior [66]. Quite a number of models were proposed to describe these highly interesting relaxor properties, such as, compositional heterogeneity [67], a superparaelectric model [53], dipole glass models [68-74], a breathing mode model [75], and random-field models [76,77]. Among these, the dipole glass and random-field models are well accepted to interpret the relaxor-type behaviors [65,78]. In the following, these major models are briefly sketched.

Dipolar glass model: The dipolar glass model is analogous to the spin glass model for ferromagnetic materials [79-81]. It describes the relaxor state is a short-order-ranged glassy state with random interactions between neighboring PNRs under the presence of random fields [74].

Generally in a dipolar glass state, a long-range ordering of the polarization becomes frustrated as the temperature decreases, which is due to a severely competing interaction between the adjacent dipolar clusters (PNRs) [82]. As a consequence, a local short-range ordering forms and a transition into a glass state takes place at the so-called static freezing temperature which can be obtained via an analysis according to the Vogel - Fulcher equation [61] (see Chapter 2.4.1). The static freezing temperature T_{VF} characterizes the onset of the measurable visco-elastic behavior of PNRs on observable time scales (Hz to MHz), which is then interpreted as a fingerprint of a glassy-like state [61]. An universal dipolar glass state includes a randomness of local disordering PNRs and a frustration leading to freezing of PNRs below T_{VF} [74].

Random-field model: The random-field model was first reported by West Westphal, Kleemann and Glinchuk (WKG model) in 1992 [76]. In the description of the WKG model, the authors referred to the idea conducted in the description of ferromagnets by Imry and Ma [83], which stated that the quenched random local fields are able to destroy a phase transition in certain systems.

This random-field relaxor state assumes a splitting of the ferroelectric state into nano-domains (analogous to PNRs) due to quenched local electric fields which are attributed to charged compositional fluctuations. In contrast to the PNRs, these nano-domains are separated by domain walls [84]. As a consequence, a smearing of the phase transition has to be induced [76].

Comparison between dipolar glass and random-field models: Based on the discussion above, we can summarize the still ongoing question whether the relaxor state in zero electric field is [74]

- (i) a glass state similar to the one in dipolar glasses with randomly interacting polar nanoregions in the presence of random fields or
- (ii) a ferroelectric state broken up into nanodomains under the constraint of quenched random electric fields.

Fig. 2.16 shows a picture of the two possible models for interpreting the relaxor state in the case of strained NaNbO_3 film. The dipole glass model indicates that the PNRs start to become

immobile at static freezing temperature $T_{VF} \approx 77$ K, therefore a dipolar glass state forms below T_{VF} . Whereas the random-field model suggests that the relaxor state might still contain ferroelectric ordering, however the transition is smeared due to the existence of a strong random field [65].

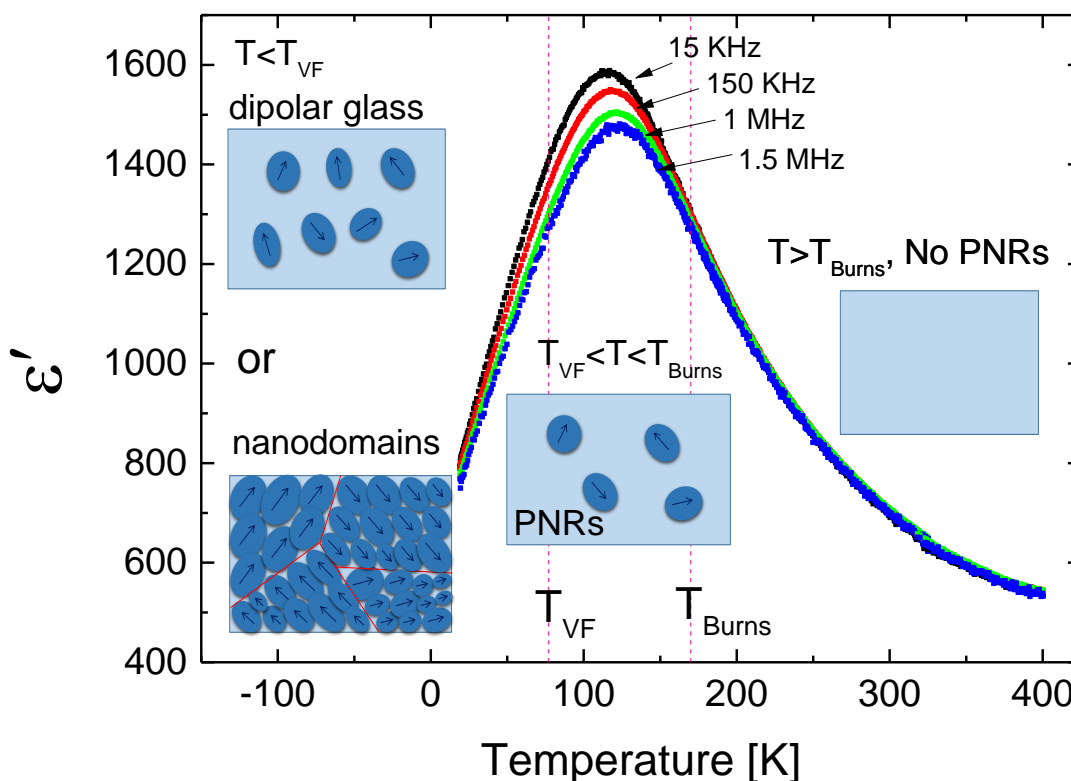


Fig. 2.16: Schematic illustrations of the evolution of PNRs in a strained NaNbO_3 film on $(110)\text{NdGaO}_3$ correlated to dipolar glass and random field models.

2.5. Engineering of ferroelectricity

As discussed in Chapter 2.3, ferroelectrics and ferroelectric thin films show most of their profound features typically in a temperature regime close to the phase transition temperature from the dielectric to ferroelectric state. In this temperature regime, for instance, the largest permittivity, piezoelectric effect, or tunability are present. Unfortunately, this transition temperature is usually far away from room temperature, e.g. $T_c \approx 37$ K for SrTiO_3 [85], 403 K for BaTiO_3 [86], 503 to 760 K (depending on the composition) for $\text{PbZr}_{1-x}\text{Ti}_x\text{O}_3$ [87], 763 K for PbTiO_3 [88], and 628 K for NaNbO_3 [16], respectively. Therefore, it is of great interest to modify

the phase transition temperature. This engineering of T_c can be achieved via strain, doping, or a combination of both.

2.5.1. Doping

In perovskite-type ferroelectrics, substitution of larger-charged or lower-charged cations at the A or B sites are able to modify the microstructure and, therefore, the electronic properties of the ferroelectrics [89]. Generally, donor doped perovskites with higher-charged doping ions (e.g. La^{3+} , Nd^{3+} , Bi^{3+} , Nb^{5+} , W^{6+}) serve as ‘soft’ ferroelectrics. The soft doping effect will lead to the generation of cation vacancies which suppress the concentration of oxygen vacancies, and therefore improves the domain wall motions. Consequently ‘soft’ ferroelectrics show low coercive fields, but high remnant polarization, permittivity, and dielectric loss. In contrast, acceptor doped perovskites with lower-charged doping ions (e.g. K^+ , Na^+ , Fe^{3+} , Mn^{2+} , Mn^{3+} , Cr^{3+}) are regarded as ‘hard’ ferroelectrics. The hard doping effect normally facilitates the formation of oxygen vacancies, which act as a source for trapping sites for domain wall pinning. ‘Hard ferroelectric’ usually exhibits high coercive fields, but low permittivity and dielectric loss [89,90]. The compatibility of dopant ions with the original cation sites can be described by the Goldschmidt tolerance factor [22, 91]:

$$t = \frac{r_A + r_O}{\sqrt{2}(r_B + r_O)} \quad (2.8)$$

where r_A , r_B , r_O are the ionic radii of A-site, B-site cations and oxygen anion, respectively. A Goldschmidt tolerance factor of $0.71 < t < 1.05$ allows the formation of cubic, orthorhombic, and rhombohedral structures [92]. In case of $t < 0.9$, the A-site ion is too small to occupy the oxygen octahedra interstices, therefore, a rotation or tilt of the BO_6 -octahedra takes place to reduce the empty space. Subsequently the oxygen anions are shifted away from the equilibrium positions, which leads to a decrease of symmetry [93] (see Fig. 2.17). As a consequence, the modification of ferroelectric properties can be achieved by chemical doping [94,95].

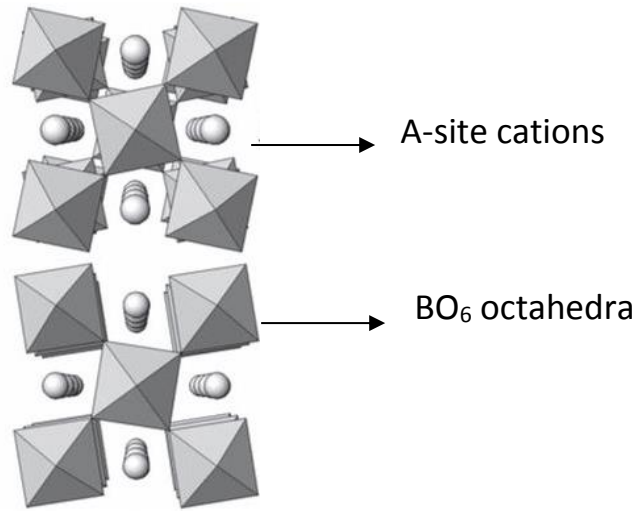


Fig. 2.17: Schematic illustration of the rotation of BO_6 octahedra, the balls represent A-site cations. The B-site cations are placed at the center of the octahedral. Adapted from [93].

2.5.2. Strain

An in-plane mechanical strain can be induced in a thin film due to the mismatch of the lattice parameters or thermal expansion coefficients between the film and substrate. [6-11,96]. Especially for epitaxially grown films, the lattice mismatch β and the expected in-plane strain η can be estimated from the lattice difference between film and substrate according to,

$$\beta = \frac{a_{nom} - a_{sub}}{a_{sub}} \quad \text{and} \quad (2.9)$$

$$\eta = \frac{a_{film} - a_{nom}}{a_{nom}} \quad , \quad (2.10)$$

where a_{nom} and a_{film} represent the in-plane lattice parameters of the unstrained and strained film, and a_{sub} is the corresponding in-plane lattice parameter of the substrate. Obviously mismatch and strain can be different for different crystallographic directions. The sign of η indicates the type of the strain, i.e. '+' suggests a tensile strain, whereas '-' hints to a compressive strain. Fig. 2.18 shows examples of engineering of tensile and compressive in-plane strain for heteroepitaxial film growth.

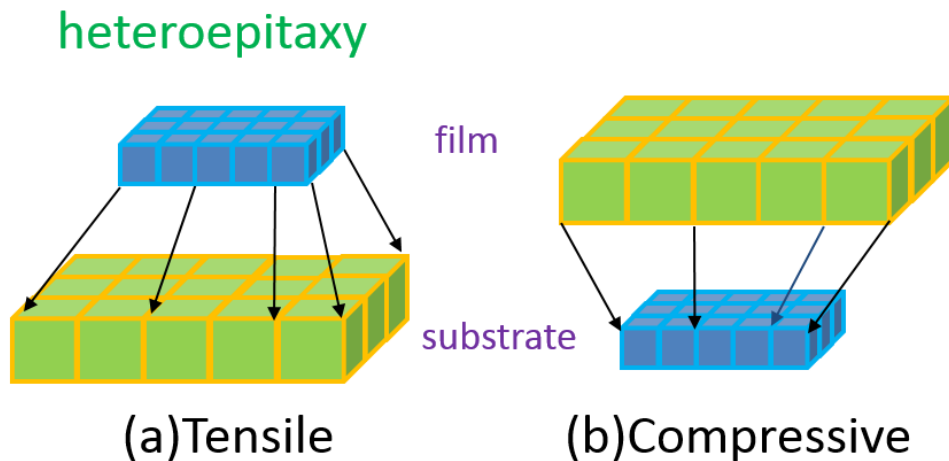


Fig. 2.18: Schematic sketch of heteroepitaxy leading to tensile (a) and compressive (b) in-plane strain, which is partially compensated by an out-of-plane strain of opposite sign.

The in-plane strain automatically modifies the structural properties of the film:

- (i) defects, like point defect, dislocation or crack, are introduced once a critical thickness (typically a few nm for point defects and dislocations) is reached,
- (ii) the in-plane lattice parameters are modified. However, also the out-of-plane lattice parameter is affected. Typically, the in-plane modification is partially compensated by the modification of the out-of-plane parameter (Poisson effect),
- (iii) consequently even structural phase transitions, e.g. from cubic to orthorhombic, can be induced via this method.

Therefore, the generation of strain in a ferroelectric thin film allows to modify the structural properties of an epitaxial film. Obviously this structural modification implies modifications of the electronic properties. For instance a strain-generated structural transition could lead to a ferroelectric phase transition, i.e. an engineering of the phase transition temperature T_C . This was first proposed by Pertsev et al. for SrTiO_3 [14,15] and later verified by experimental researches [6-11,96].

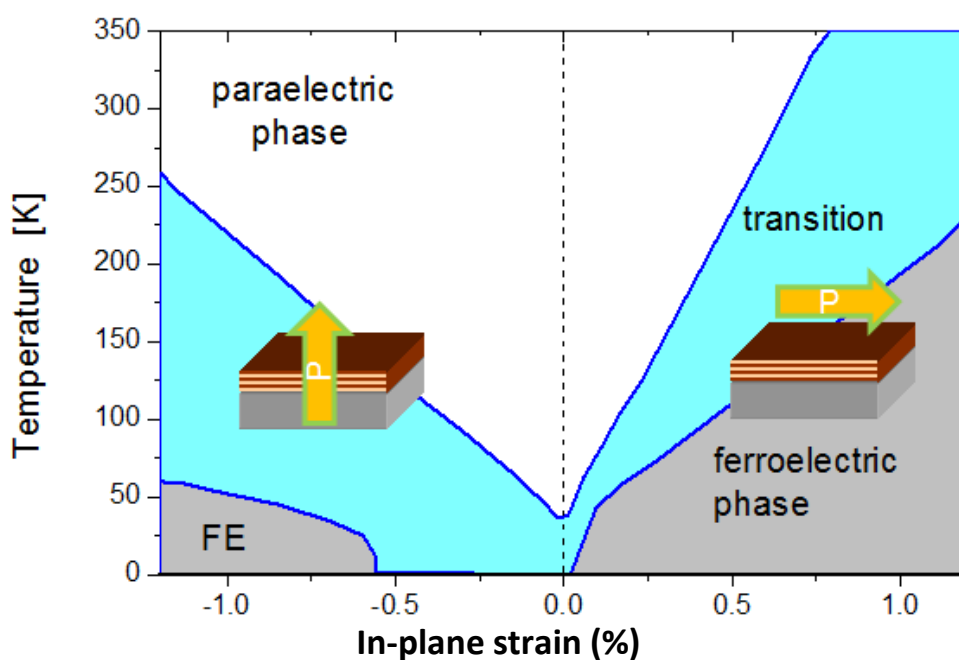


Fig. 2.19: Prediction of the shift of T_C in SrTiO₃ as function of the in-plane strain based on Pertsev et al.. The cyan region represents the range (error bar) of the phase transition. The arrows indicate the direction of enhanced polarization. Adapted from [18]

Fig.2.19 shows the theoretical expectation of the enhancement of T_C in SrTiO₃ thin films. The imparted tensile (positive) or compressive (negative) strain indicate the in-plane lattice constants of the film are elongated or contracted, respectively, during the epitaxial growth, which subsequently induces an in-plane or out-of-plane polarization, respectively. As a consequence, an enhancement of T_C is expected along in-plane or out-of-plane direction for in-plane tensile or compressive strain, respectively. The expected phase transition regime based on thermodynamic analysis is marked by the cyan area. The width of the transition is due to the spread in the reported coefficients for SrTiO₃ [6].

In this prediction only an enhancement of T_C is predicted and later demonstrated. In this work we will show, that we can also reduce T_C or generate a phase transition at low temperature by an appropriate strain. Considering the fact, that the phase transition temperatures for almost all technically relevant ferroelectrics are actually far beyond room temperature, this might be more important for applications, than to increase an already too high transition temperature.

3. Sample preparation and experimental techniques

In this chapter, the sample preparation techniques and characterization techniques are introduced. This includes the film deposition, various structural characterization methods, design of thin film structures, lithography, lift-off technology, and the electronic characterization and thus interpretation.

3.1. Sample preparation

The $\text{Na}_{1+x}\text{NbO}_{3+\delta}$ thin films investigated in this thesis are deposited via either metal organic chemical vapor deposition or pulsed laser deposition at the Leibniz Institute for Crystal Growth in Berlin. The metallization (Au, Pt) is done via evaporation technique in our institute. A simple introduction of deposition techniques is given in the following part.

3.1.1. Metal organic chemical vapor deposition

Metal organic chemical vapor deposition (MOCVD) represents a typical method used for the growth of oriented or epitaxial films of high quality. It is based on the pyrolysis reaction between the targeted elements in a gas phase on the surface of the wafer. In contrast to physical deposition techniques, e.g. pulsed laser deposition (PLD), molecular beam epitaxy (MBE) or magnetron sputtering, the organometallic precursor plays an important role as a prominent medium to carry and homogeneously distribute the film-elements in MOCVD deposition technique.

The NaNbO_3 films used in this thesis are deposited via liquid delivery MOCVD on (110) oriented single-crystalline NdGaO_3 substrates. $\text{Na}(\text{thd})$ ((thd) = 2,2,6,6-tetramethyl-3,5-heptanedione) and $\text{Nb}(\text{EtO})_5$ ($(\text{EtO})_5$ = penta-ethoxide), dissolved in dry toluene at a concentration of 0.01 M, are used as source materials for Na and Nb, respectively. In the vertical MOCVD system, the two liquid precursor solutions are independently transported by peristaltic pumps to two separated flash evaporators that are operating at a temperatures of 503 K and 463 K for the $\text{Na}(\text{thd})$ solution and for the $\text{Nb}(\text{EtO})_5$ solution, respectively. Argon is employed as carrier gas for the transport of the evaporated metal–organic (MO) precursors into the reactor chamber via a showerhead. The substrate carrier is rotating at 500 r/min in order to improve the

mixture of the MO precursor gases, the Ar dilution gas, and the O₂ oxidant gas, and thus to improve the resulting film homogeneity. The films are deposited at a gas pressure of 2.6 kPa, a substrate temperature of 973 K, a typical Na to Nb ratio of the source solutions of 1, and an O₂ to Ar ratio of the gas phase of 0.63 [52]. Fig. 3.1 shows the sketch of MOCVD setup used for deposition of NaNbO₃ thin films [97]. The film thickness is varied between 10 and 140 nm. In this thesis, we only examined Na_{1+x}NbO_{3+δ} films on (110) oriented NdGaO₃. In order to obtain a better epitaxial growth, the NdGaO₃ substrates are slightly off-oriented (0.1°) and annealed in pure oxygen flow at 1050 °C for one hour. This generates a regular step-and-terrace surface structure with NdO surface termination [98] and promotes step flow growth of the film.

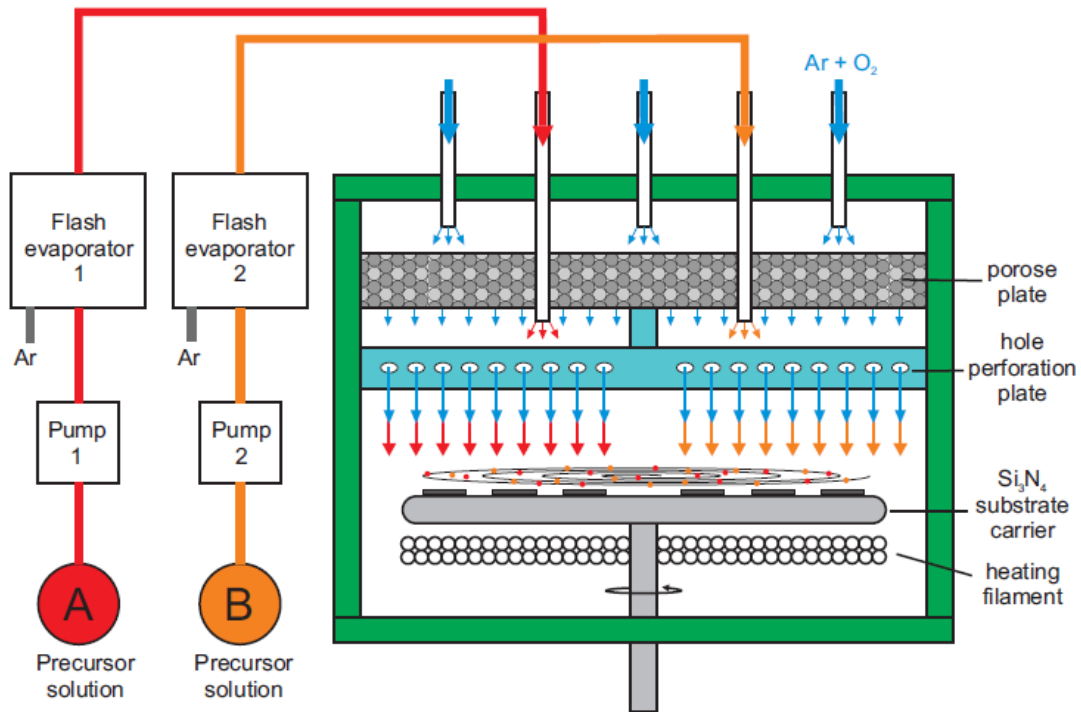


Fig. 3.1: The sketch of the MOCVD setup at Leibniz Institute for Crystal Growth, Berlin. Adapted from [97].

3.1.2. Pulsed laser deposition

Pulsed laser deposition (PLD) is a very flexible physical vapor deposition technique for thin film growth. It was used in this work to provide first test and to examine for instance the impact of stoichiometry variations on the structural and electronic properties of the strained $\text{Na}_{1+x}\text{NbO}_{3+\delta}$ films on (110) NdGaO_3 . In this technique, the high-energy photons in the focused laser beam excite the electron at the surface of the target. The target material is locally heated up and evaporated in the form of a plasma plume. With the expansion of the plasma, the target materials is deposited on the substrate. It should be noted that due to the inhomogeneous flux and angular energy distribution in the ablation plume, variations of the composition of the film have to be expected. Moreover, due to the large particle energy compared to MOCVD, a larger defect density is expected for PLD films compared to MOCVD films.

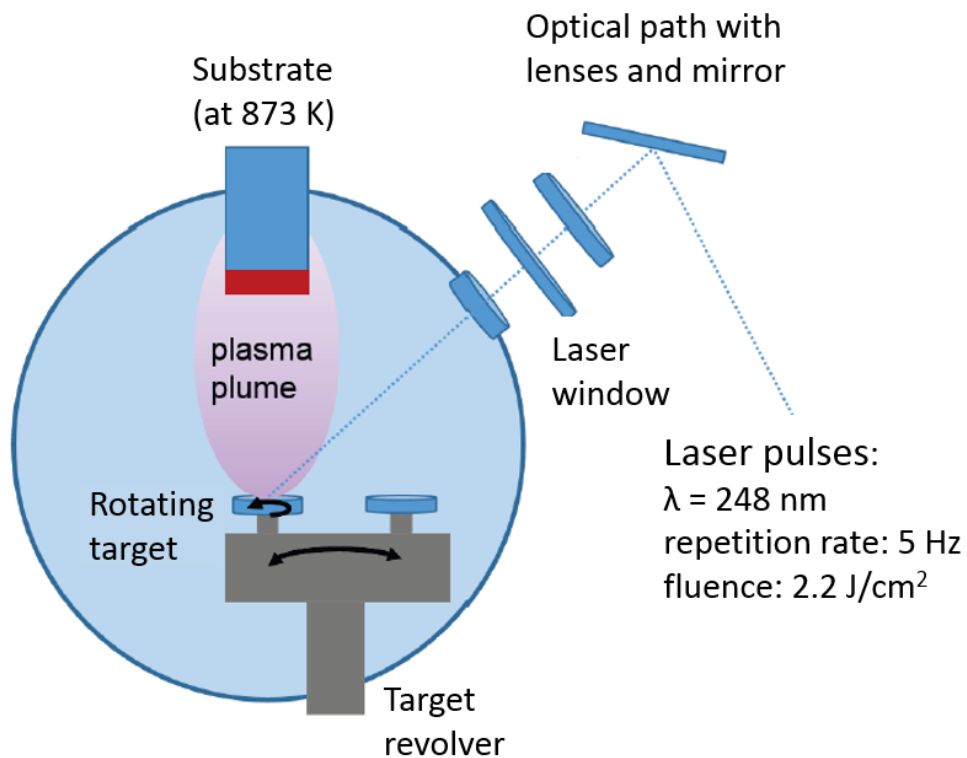


Fig. 3.2: Schematic illustration of the setup of PLD at Leibniz Institute for Crystal Growth, Berlin. Adapted from [100].

For the PLD process a KrF excimer laser ($\lambda = 248$ nm) with an energy fluence of 2.2 J/cm² and a pulse repetition rate of 5 Hz is used. The oxygen pressure during deposition is 70 Pa, the substrate temperature is 873 °C. Similar to the MOCVD process, prior to the Na_{1+x}NbO_{1+δ} deposition, the (110) oriented single-crystalline NdGaO₃ substrates are annealed in pure oxygen flow at 1050 °C for one hour in order to generate a regular step-and-terrace surface structure with NdO surface termination [98] and promote step-flow growth of the NaNbO₃ film. More details to the deposition conditions are given in Ref. [99]. Fig. 3.2 schematically illustrates the sketch of PLD setup which is employed to produce off-stoichiometric films [100].

For the PLD deposition stoichiometric target and off-stoichiometric sodium excess targets are fabricated with a nominal Na/Nb ratio ranging from 1 to 1.37 in the raw material mixture. All targets are prepared by conventional solid state reaction. Sodium carbonate (Na₂CO₃, 99.997% purity) and niobium oxide (Nb₂O₅, 99.9985% purity) powders are mixed, milled, and pressed into pellets of 2.5 cm in diameter at 2000 bar. Subsequently, the pellets are first calcined for six hours and in a second step sintered for 12 hours at 950 °C inside a Pt/Au crucible in ambient air. The resulting Na/Nb ratio in the sintered target is analyzed via an inductively coupled plasma using optical emission spectroscopy (ICP-OES) measurements. For instance, for a Na/Nb ratio of 1.22 in the raw material mixture, a Na/Nb ratio of 1.17 is obtained in the target. The ratio in the deposited Na_{1+x}NbO_{3+δ} film roughly agrees with the stoichiometry of the target.

3.1.3. Evaporation deposition

Evaporation deposition is used for the deposition of the metallic electrodes. In this technique the evaporative material is simply heated up and evaporated in a vacuum chamber. Subsequently the evaporated material in the form of vapor travels to the substrate and condenses into a film at the surface of the substrate. The metallization of Au, Pt or Ti/Pt layer in this thesis is done by evaporation deposition. Fig. 3.3 shows the evaporation device used in this thesis.



Fig. 3.3: Picture of the evaporation setup of the Helmholtz Nanoelectronic Facility (HNF) of Jülich Research Center.

3.2. Characterization of structure and stoichiometry

In this part, the techniques, such as, X-ray diffraction, reciprocal space mapping, transmission electron microscopy and Rutherford backscattering spectrometry used to characterize the structural and compositional features of the ferroelectric thin films are introduced.

3.2.1. X-ray diffraction

X-ray power diffraction (XRD) represents a standard technique to analyze the crystalline structure of materials. X-ray is an electromagnetic radiation with a wavelength ranging from 0.1 to 100 Å which is typically comparable to the size of the atom and molecule. In this technique, the incident X-ray collides with the crystalline planes of the sample, and a general scattering effect towards random directions sets in. Most scattering of X-ray is compensated as a destructive interference, whereas a diffraction takes place when these scattered X-rays are in phase with each other (constructive interference). A detector is used to collect the

angles and intensities of these diffracted X-rays. Via analyzing these XRD data, the lattice parameters, crystalline phase and structure can be determined. The constructive interference of the diffraction of the incident X-ray fulfills the Bragg's law:

$$n\lambda = 2d_{hkl}\sin\theta \quad , \quad (3.1)$$

where n is an integer, λ represents the wavelength of the incident X-ray, d_{hkl} denotes the spacing between the parallel crystalline planes with miller indices (h, k, l) , and θ indicates the incident angle of the X-ray. A sketch of the Bragg-Brentano geometry ($\theta/2\theta$) is shown in the inset of Fig. 3.4.

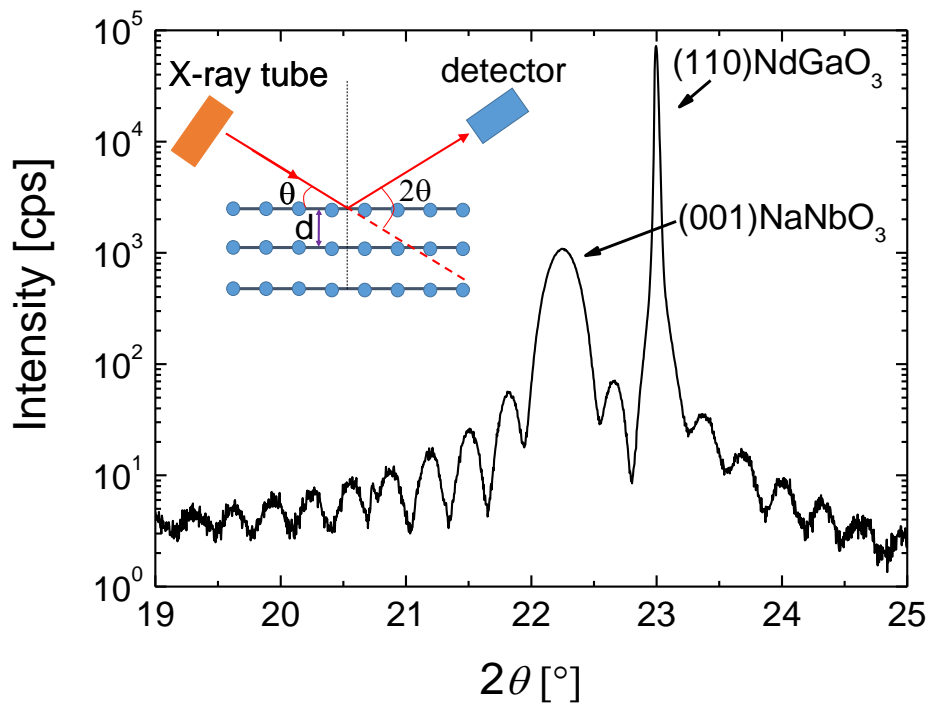


Fig. 3.4: HRXRD $\theta/2\theta$ scan (Bragg-Brentano scan) of a NaNbO_3 on a $(110)\text{NdGaO}_3$ substrate. The major two peaks are explicitly analyzed and ascribed to $(001)\text{NaNbO}_3$ and $(110)\text{NdGaO}_3$, respectively. The rest of the peaks with less intensity are thickness fringes which help to estimate the thickness of the film. The inset shows the sketch of the Bragg-Brentano geometry. Adapted from [100].

The structural properties of the target and film are analyzed via XRD in this thesis. The crystallographic phases of the ceramic targets are determined via standard XRD with $\text{Cu K}\alpha$ radiation ($\lambda = 1.541 \text{ \AA}$). The structural properties of the NaNbO_3 films are analyzed via high-

resolution x-ray diffraction (HRXRD) by a Bruker Discovery D8 with the Cu $K\alpha_1$ line ($\lambda = 1.54056$ Å). Symmetrical $\theta/2\theta$ scans (Bragg-Brentano scans) are used to determine the out-of-plane lattice parameters of the films and to evaluate among others the film thickness [100]. Fig. 3.4 shows a typical HRXRD scan of a c-axis oriented NaNbO_3 film on $(110)\text{NdGaO}_3$. In addition to the $(001)\text{NaNbO}_3$ and $(110)\text{NdGaO}_3$, thickness fringes are observed that yield a film thickness of $27 \text{ nm} \pm 1 \text{ nm}$.

3.2.2. Reciprocal space mapping

For the analysis of the epitaxial growth of the strained films, 2-dimensional (2D) reciprocal space mappings (RSM) is an extremely useful tool. It is basically an extended XRD technique that scans the complete angular range for ω and θ around a given Bragg reflex of the film and the substrate. The resulting 2D images of the Bragg reflex are then “mapped”, therefore the name. The mapping provides information on structural correlation (e.g. epitaxy, strain, or strain relaxation) between film and substrate. As in standard XRD, incident X-ray with a wave vector \underline{k} and wavelength of $2\pi / \lambda$ impinges the surface of the sample under an angle of ω . The detector is located with an angle of 2θ with respect to the incoming beam. Therefore, the angle between the diffracted beam \underline{k}' with respect to the sample surface is $2\theta - \omega$. As a consequence, the scattering vector is equal to $\underline{q} = \underline{k}' - \underline{k}$, which is related to ω and 2θ . The resulting components of \underline{q} which are parallel or normal to the surface of the sample are obtained, respectively:

$$q_{\parallel} = \frac{2\pi}{\lambda} [\cos(2\theta - \omega) - \cos(\omega)] \quad (3.2)$$

and

$$q_{\perp} = \frac{2\pi}{\lambda} [\sin(2\theta - \omega) + \sin(\omega)] \quad (3.3)$$

When the detector is fixed and only the sample is rotated, the so-called ω scan is achieved. In this case the length of \underline{q} is constant but the direction of \underline{q} varies. On the other hand, if the sample and detector are rotated simultaneously especially with an angle ratio of 1 : 2 ($\omega/2\theta$ scan, Bragg-Brentano geometry), the direction of \underline{q} is fixed while the length of \underline{q} keeps changing. If both methods are combined, the reciprocal space can be scanned in two orthogonal directions, and a 2D image of the reflected intensity (the RSM) can be obtained. A

Bruker Discovery D8 system is applied for our RSM measurements. Fig. 3.5 sketches the mechanism of RSM measurements [101].

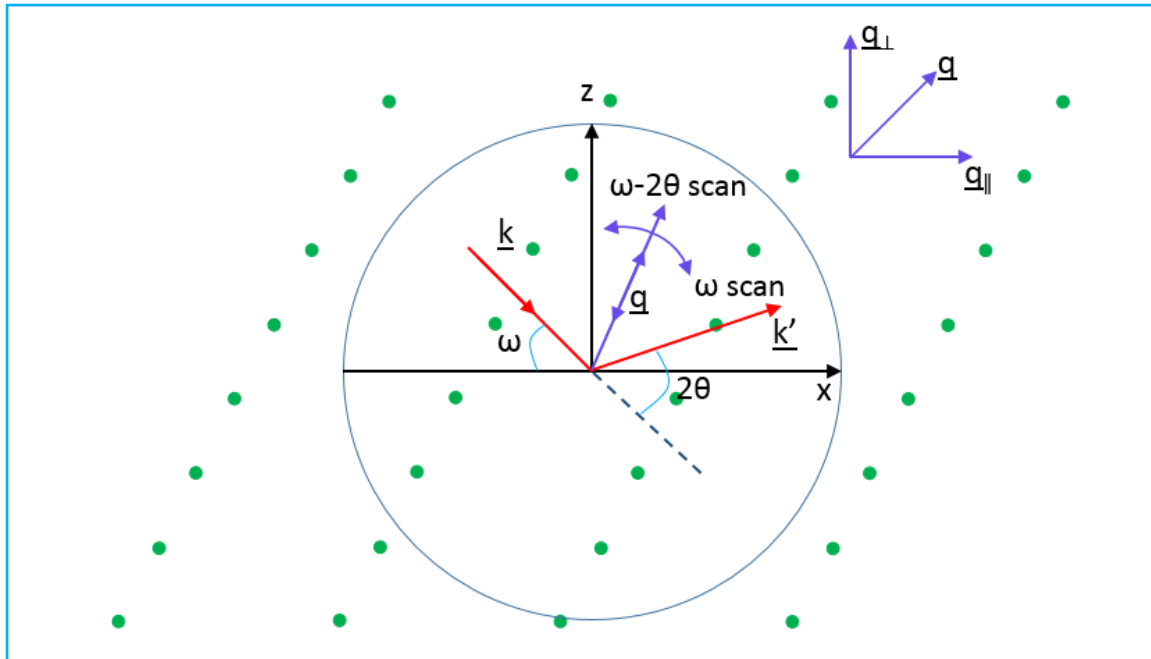


Fig. 3.5: Schematic illustration of the 2D-RSM measurements showing the 2D section of the Ewald sphere. The parameters ω , 2θ , and \underline{q} in combination with the two measuring models, i.e. ω scan and $\omega/2\theta$ scan, are given in the figure. Adapted from [101].

Our standard strained NaNbO_3 films grow on the (110) NdGaO_3 substrate in the form of a pseudocubic on an orthorhombic structure. Examples of RSMs recorded in the vicinity of the asymmetric (444) Bragg reflection of the NdGaO_3 substrate on NaNbO_3 films of different thickness are shown in Fig. 3.6. The indices “o” for orthorhombic and “pc” for pseudocubic describe the contributions of the NdGaO_3 substrate and NaNbO_3 film, respectively. The fact that q_{\parallel} of $(444)_o \text{NdGaO}_3$ and $(402)_{pc} \text{NaNbO}_3$ coincide proves the epitaxial growth, i.e. the in-plane lattice parameters of the film and substrate agree (at least for thin films). However, with increasing thickness of the film the $(402)_{pc}$ reflex of the film expands towards lower q_{\parallel} values, i.e. larger in-plane lattice parameters. This is an indication for a partial plastic relaxation of the incorporated compressive strain towards the lattice parameters of unstrained NaNbO_3 . This process starts at a critical thickness of a few nanometers [52] and becomes more prominent with increasing thickness. For the thickest film (140nm) the $(402)_{pc}$ reflection of the film is extended to the value of unstrained NaNbO_3 which is marked by a circle in Fig. 3.6 (c). This indicates that part of the film (i.e. the top layer) is more or less

completely relaxed. Moreover, the RSM also shows, that the in-plane compressive strain is at least partially compensated by an out-of-plane expansion of the lattice parameter (tensile strain). In analog, the relaxation observed in thicker NaNbO_3 samples leads to an increase of q_{\perp} value, i.e. reduction of the out-of-plane lattice parameter due to strain relaxation. The sketch in Fig. 3.6 shows the resulting structural correlation between the epitaxial NaNbO_3 film and the $(110)_{\text{NdGaO}_3}$ substrate according to the RSM results and based on a “classical model”. In chapter 4.3 we will discuss this model and show, that this model cannot explain the electronic properties of the film and, therefore, most likely has to be modified.

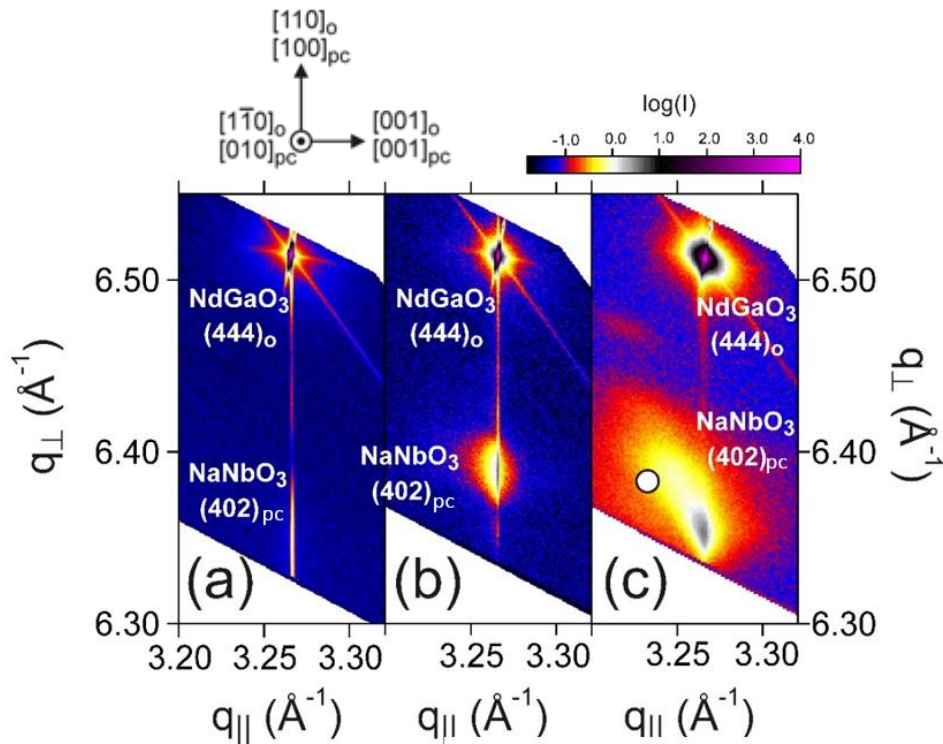


Fig. 3.6: High resolution x-ray diffraction RSM in the vicinity of the $(444)_{\text{o}}$ Bragg reflection of the NdGaO_3 substrate for a 11 nm (a), 80 nm (b) and 140 nm (c) thick sample. The circle in (c) marks the position of the corresponding $(402)_{\text{pc}}$ reflex of unstrained NaNbO_3 . The sketch shows the resulting structural correlation of film and substrate according to the “classical model” which will be discussed in detail in Chapter 4.3.

3.2.3. Transmission electron microscopy

Transmission electron microscopy (TEM) represents an imaging technique for matters, especially crystalline structures, with an atomic resolution. In this technique an electron beam is traversing a very thin sample and interacting with the atoms in the sample. A detector

collects the transmitted electrons. Based on the detector data a 2D image of the material is constructed. In comparison to the conventional TEM, scanning transmission electron microscopy (STEM) generates a more focused electron beam. It allows to analyze the data in terms of energy dispersive X-ray (EDX) spectroscopy, electron energy loss spectroscopy, or annular dark-field imaging (ADF).

High-resolution TEM and STEM are performed with an aberration corrected FEI Titan 80 – 300 electron microscope operated at 300 kV on NaNbO_3 reference sample at the Leibniz Institute for Crystal Growth, Berlin. As an example, Fig. 3.7 demonstrates the epitaxy (coherent interface) for an 11 nm thick NaNbO_3 film and $(110)\text{NdGaO}_3$ [52].

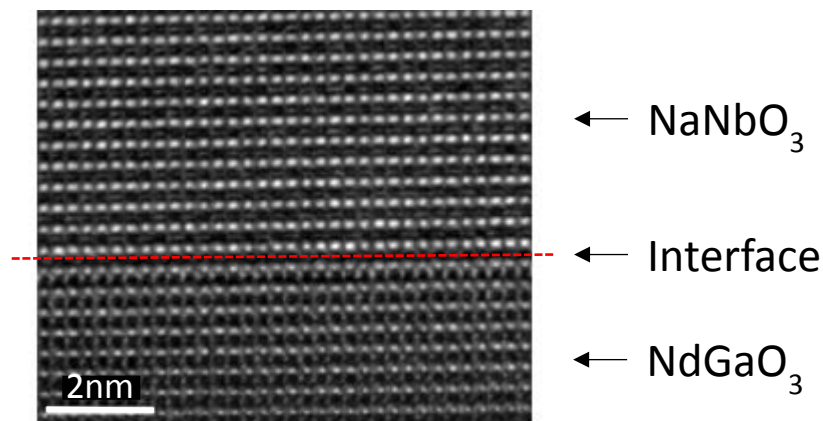


Fig. 3.7: High resolution TEM picture of NaNbO_3 thin film (11 nm) grown on $(110)\text{NdGaO}_3$. Adapted from [52].

3.2.4. Rutherford backscattering spectrometry

Rutherford backscattering spectrometry (RBS) represents an ion scattering technique that is used for a quantitative analyses of composition and thickness of our thin film sample. Alpha particles, e.g. He^{2+} ions, from the incident beam are accelerated in a linear particle accelerator to a high energy (typical kinetic energy of 0.5 – 4 MeV) are collided at the surface of the target (sample). The energy of the backscattered alpha particles are recorded via an energy sensitive detector. The energy loss during the backscattering process is ascribed to the elastic collision between the projectile and the nuclei of the atoms in the sample in combination with a minor contribution from the small angle in-elastic collision between the projectile and the electrons

of the target atoms. The first contribution is associated with the mass of the atom (leading to the stoichiometry), whereas the latter one describes the depth of the atom which scatters the projectile (leading to the thickness of the layer). The resolution of RBS is directly correlated to the mass of the examined atom. This also means, heavy atoms (in our case Nd, Nb, Ga) can easily be detected, whereas light atoms (in our case Na or O) are hardly visible. Based on the energy conservation during elastic collision, a larger kinetic energy of the backscattered ions will be achieved by colliding a heavier target. Therefore a larger energy change during the scattering is detected for atom with larger mass which allows to distinguish different types of atoms.

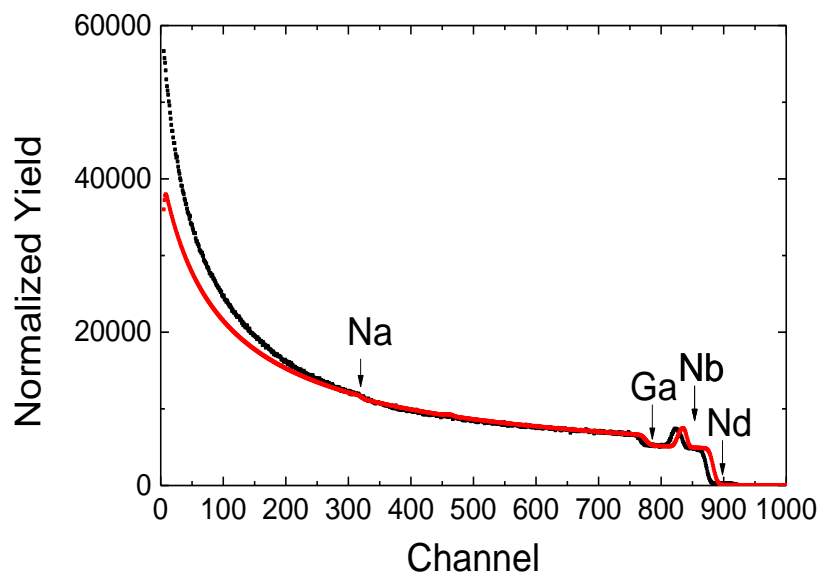


Fig. 3.8: Examples of an RBS measurement on a 30 nm thick NaNbO_3 film on NdGaO_3 . The experimental data (black line) is fitted via the program XRump (red line) using an input of the nominal stoichiometry and density of NaNbO_3 and NdGaO_3 and the thickness of the film (30 nm). The expected positions for the detection of the different elements of the system are indicated and agree with the experimental data.

Fig. 3.8 shows a typical RBS measurement of a thin (≈ 30 nm) NaNbO_3 film which is examined in this thesis. The original data (black line) is simulated (“XRump”) (red line) using the appropriate thickness of the film and the elements (and their density) that we present in the system. The agreement between the fit and experiment confirms the assumption used for the fit.

3.3. Device design for the electronic characterization

In order to study the electronic properties of our samples, reasonable device structures are required for the experiments. In this thesis, mainly interdigitated capacitors, nano-contact for the local analysis of the conductive behavior of the oxide layer, Pt-temperature sensors for local recording of the temperature, and a Pt heater are employed. Fig. 3.9 shows the general sketch of certain devices integrated to the examined samples which are used for measurements.

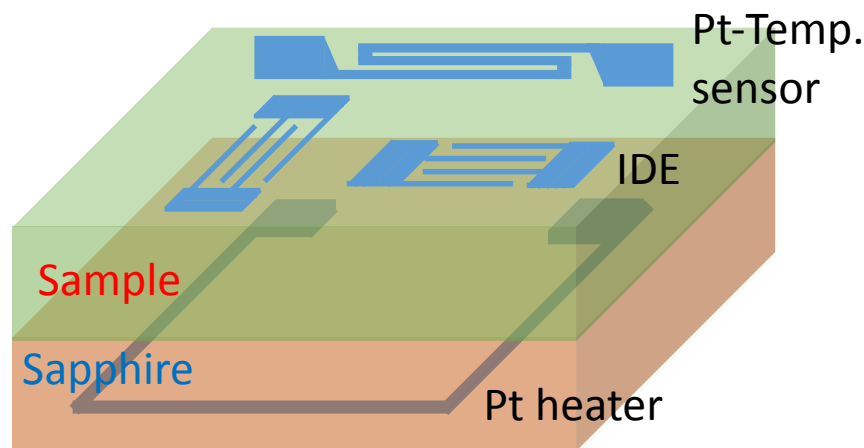


Fig. 3.9: Sketch of the integrated devices, e.g. interdigitated capacitor, Pt-temperature sensor and Pt heater, used in this thesis.

3.3.1. Interdigitated electrodes

For the investigation of the in-plane dielectric and resistive properties of the $\text{Na}_{1+x}\text{NbO}_{3+\delta}$ films, planar capacitors based on interdigitated electrodes (IDE) are employed. The IDEs are prepared via lift-off lithography technique and deposition of a thin (30 nm) Pt/Ti layer which will be introduced later. In order to obtain a reliable and large signal, a relatively large gap size $s = 5 \mu\text{m}$ is chosen that is compensated by large length $d = 700 \mu\text{m}$ of the individual IDE's fingers (width of the finger is $10 \mu\text{m}$) and a large number (64) of fingers resulting in an effective length of the capacitor of 44.1 mm [8]. In order to avoid stray fields the gap is strongly extended at the end of each finger ($45 \mu\text{m}$). This guarantees that the electric field E is oriented perpendicular to the direction of the fingers.

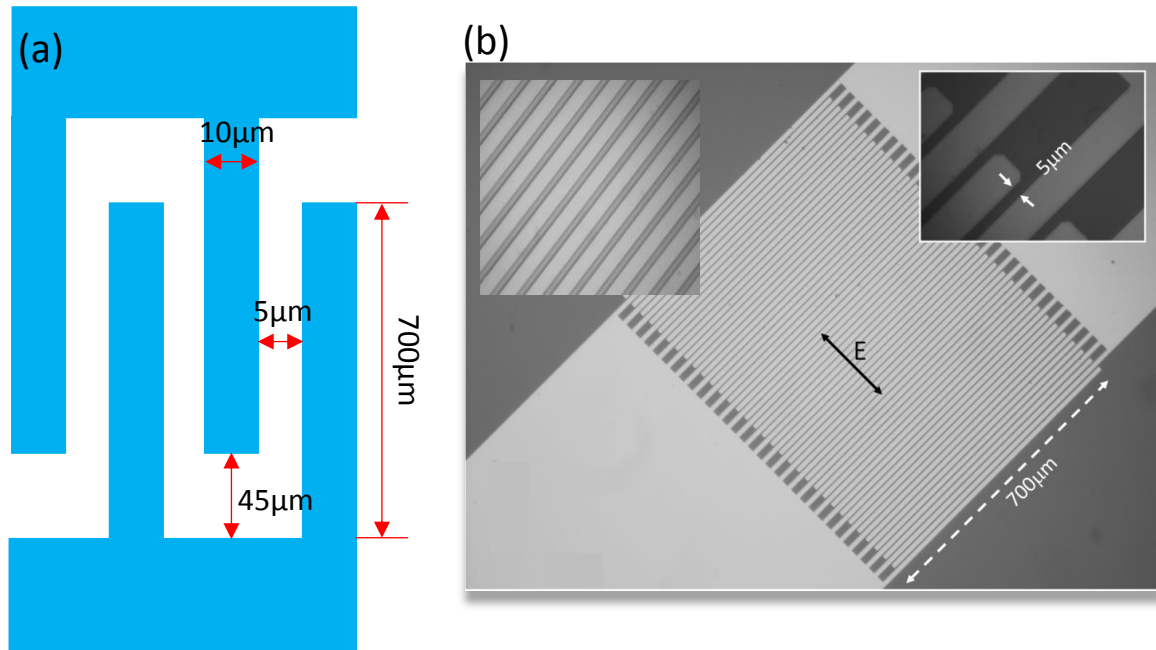


Fig. 3.10: Schematic illustration (a) of the IDEs with dimensions used in this thesis and scanning electron microscopy pictures (b) of the IDEs. The inset shows part of the IDE with larger amplification.

Two (in some case three) different orientations of the IDEs are prepared on each sample, which allow to determine the ferroelectric properties for different field orientations. The two major IDE orientations are those where the electric field E is either orientated along the longer in-plane axis of $(110)\text{NdGaO}_3$ substrate, i.e. $E \parallel [1\bar{1}0]\text{NdGaO}_3$, or the short in-plane axis of substrate i.e. $E \parallel [001]\text{NdGaO}_3$. We denote these two major directions for simplicity “long axis, L ” and “short axis, S ”. In a few cases other directions are examined, e.g. a “diagonal or 45° orientation” with $E \parallel [1\bar{1}1]\text{NdGaO}_3$. Fig. 3.10 shows a sketch of planar IDEs and scanning electron microscopy pictures of one example which nicely presents the μm -size structure and the parameters used for this device.

3.3.2. Integrated Pt temperature sensor

One of the most important parameters that has to be determined during the cryoelectronic measurement is the temperature of the $\text{Na}_{1+x}\text{NbO}_{3+\delta}$ thin film. In first experiments we relied on commercial temperature sensors that were mounted close to the sample. Even after optimizing the experiment, temperature difference of a few K between the sensor and the

film could not be excluded. Especially in experiments that required fast temperature changes, we noticed, that we had to change the temperature recording.

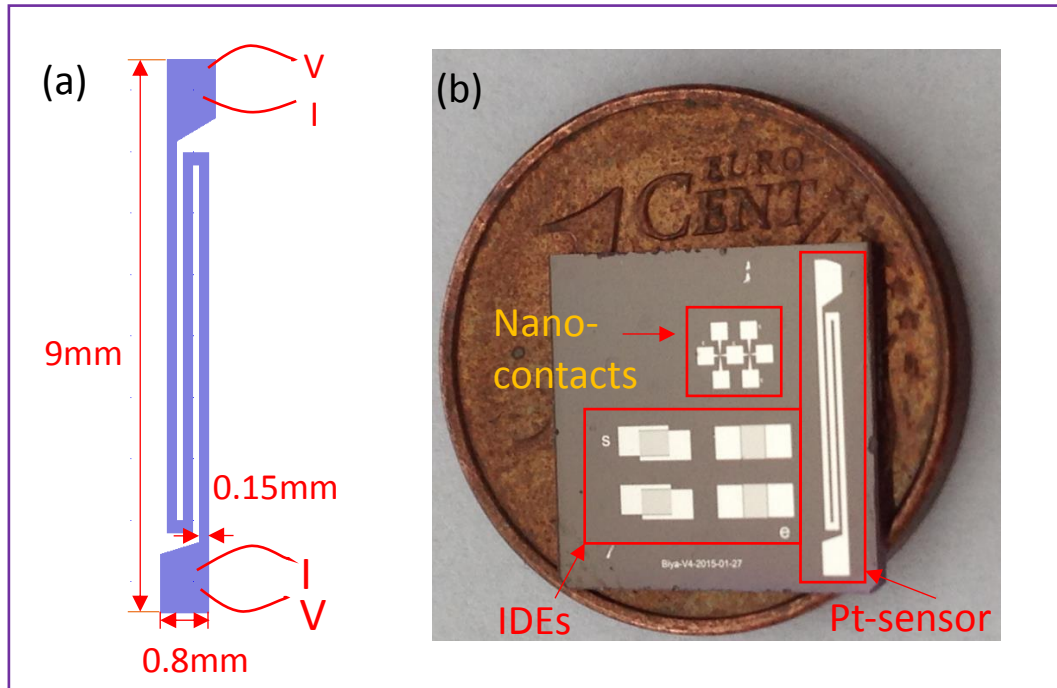


Fig. 3.11: Design of the Pt temperature sensor with specific parameters (a) and an image (b) of a NaNbO_3 sample ($10 \times 10 \text{ mm}^2$) with 4 IDEs with different orientations, nano-contacts for resistive measurements of the NaNbO_3 film, and integrated Pt temperature sensor. The sample is located on top of a one Euro cent coin for comparison.

Therefore we developed a thin film temperature sensor that is integrated directly on the thin film. For this we used the Pt-layer that is also used for the IDEs. By adding a stripe line of adequate length to the design of the electrode structure, we developed a resistive Pt-sensor for the temperature reading. Fig. 3.11 shows the design and an image of a sample consisting of a Pt-sensor, 4 IDEs structures, and several nano-contacts for additional resistive measurements that are not described in this thesis.

The resulting Pt-temperature sensor has a typical resistance of $200 - 400 \Omega$ at room temperature and a linear temperature dependence over a large temperature regime (typically 70 to 500 K were employed). After calibration using the internal commercial temperature sensor (Xenox, Lakeshore), the temperature reading was done with the integrated sensor except for the temperature regime $T < 70 \text{ K}$.

3.3.3. Integrated Pt heater

Additionally to the integrated Pt temperature sensor, a Pt heater was developed. There are two main reasons for this development:

- (i) we wanted to enhance the heating speed and, thus, reduce the measuring time and
- (ii) we tried to extend the temperature regime for the measurement to 400 – 500 K. These measurements should be performed in the cryostat (4K – 320 K) in order to allow fast sweep between high and low temperature and avoid discontinuities in the data that are caused by changes in the experimental setup (e.g. moving the sample from the cryostat to an external setup for measurements at elevated temperature)

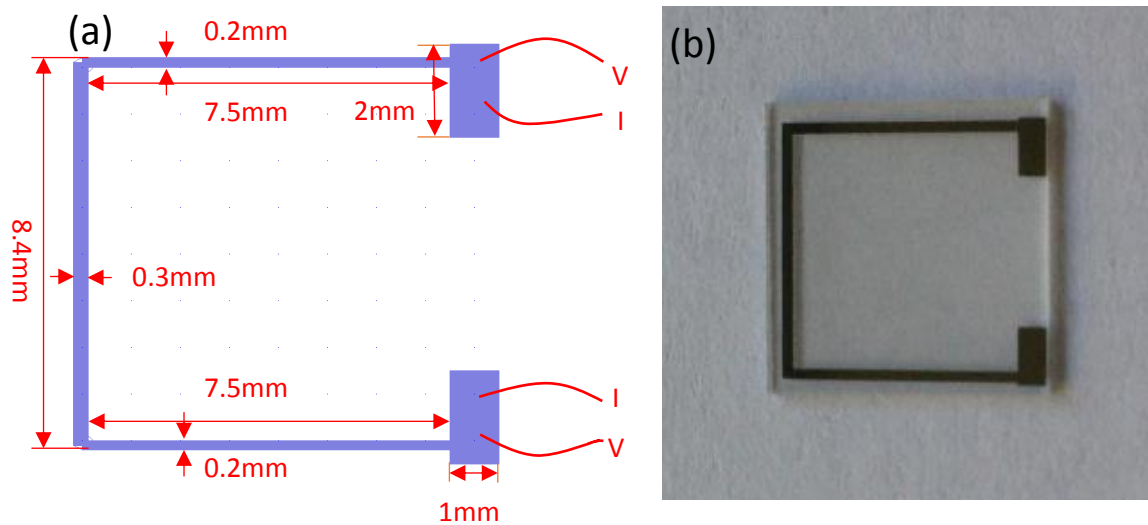


Fig. 3.12: Design of the Pt heater (a) and image (b) of a Pt heater deposited on a $10 \times 10 \text{ mm}^2$ sapphire. Length and width are given in the design.

In a first step, we integrated a resistive Pt-heater (similar to the Pt temperature sensor) in our sample design. However, it turned out, that this heater which is working at a power of a few W, interfered with our capacitive measurements. Therefore we separated the heater and prepared it on a separate substrate ($10 \times 10 \text{ mm}^2$ sapphire) and mounted this thin film (30nm) heater back-to-back to the sample. Fig. 3.12 shows the simple design and an image of such Pt-

heater. The typical resistance of the heater is around 250 – 300 Ω , it works reliably even at 20 W, producing enough power in order to heat the sample up to approximately 700 K.

3.4. Device fabrication techniques

All devices are fabricated via lift-off technology using electron-beam lithography and metallization (Au, Pt, Ti, and Cr deposition). The specific recipe is explicitly described in the following.

1. **Cleaning:** In order to remove organics and dust, the sample is rinsed successively in a solvent of acetone and isopropanol for 5 mins in an ultrasonic bath with moderate power and then dried in nitrogen gas.
2. **Spin Coating:** Photoresist, poly(methyl-methacrylate) (PMMA), is spin-coated onto the sample at 4000 revolution per minute for 1 minute. PMMA 649.04 950K (company Allresist) was used in this thesis.
3. **Baking:** The sample is located on a hot plate at 120 °C for 30 minutes. Baking temperature and time are optimized with regard to the quality of the structure and the thickness of the PMMA layer. They typically deviate from standard conditions provided by the company [102].
4. **Cr deposition:** A 20 nm thick Chrome layer is deposited onto the PMMA layer via evaporation deposition in order to enhance the surface conductivity of PMMA, which is essential for the next step, the E-beam writing.
5. **E-beam writing:** The specific patterns and shapes are written into the electron-sensitive photoresist, i.e. PMMA (positive photoresist), via the focused electron in an “e-beam writer”.

In this thesis, an e-beam writer (VISTEC EBP 5000 plus) based on a field-emission source was used. The corresponding masks were designed by AutoCAD or Clewin. The incident focused electron beam traverses the PMMA and cracks the major polymer chains of the PMMA. As a consequence, at the exposed area, the PMMA can be selectively removed afterwards, whereas at the un-exposed region it will stay on the sample.

The parameters, especially the electron doses, play a major role for the resolution and quality of the pattern. If the electron doses are too small or too large, it will cause aberrations of the resulting patterns. A small dose is not able to penetrate the complete photoresist, i.e. the region is under-exposed, whereas a too large dose will cause a diffusion of electrons at the edge of the mask, i.e. the region is over-exposed. Optimization of the electron dose was performed in order to get stable and good-quality patterns.





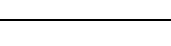

6. **Cr etching:** The 20 nm thick Cr layer is removed by an etchant typically a mixture of ceric ammonium nitrate ((NH₄)₂[Ce(NO₃)₆]), perchloric acid (HClO₄) and water with a ratio of 10.9 % : 4.25 % : 84.85 % (microchemicals). The Cr etching rate is 80 nm/min, therefore 15 s of etching is required for our samples. The chemical etching does not change the property of the PMMA at all. Afterwards, the sample is rinsed in de-ionized water in an ultrasonic bath for 10 mins and then dried using the nitrogen gun.
7. **Development:** The exposed PMMA is removed by a developing solvent (developer). The sample is rinsed in the developer AR-600-55 (Allresist) with the main component of methyl-isobutyl-ketone (MIBK) [102] for 2 mins. Then it is rinsed in isopropanol for 1 min to wash away the developer, finally the sample is dried using again the nitrogen gun.

The development time has also to be optimized via experiments. A too short time leads to an under-development, i.e. the exposed region is only partially removed. A too long time leads to an over-development, i.e. additional un-exposed region adjacent to exposed region can be removed.

8. **Pt deposition:** The metallic patterns are deposited on top of the sample via evaporation deposition. First a 5 nm thick Ti layer is deposited in order to enhance the adhesion. Subsequently a 25 nm thick Pt layer is deposited on top of Ti as the second layer.
9. **Lift-off:** The Pt/Ti layer on top of the PMMA is removed (lift-off), whereas the metal layer directly on top of the sample remains. The PMMA is dissolved in acetone, removing at the same time the metallic layer on top of the PMMA. The sample is rinsed in acetone for 5 mins, and the designed pattern appears (in most cases). If some PMMA remains on the sample, a 30 s ultrasonic bath treatment with moderated power can be applied. It should be noted that a longer time (> 30 s) not only removes the PMMA, it can also remove part of the metallic patterns. Subsequently the sample is rinsed in isopropanol for 1 min to remove the acetone. Afterwards, the sample is dried using the nitrogen gun.

The whole recipe of E-beam lithography is summarized in table 3.1.

Table 3.1: Summary of the lift-off technique used in this thesis. UB stands for ultrasonic bath.

step			process	sketch	
1	Cleaning	a b c	Acetone (UB, 5 mins) Isopropanol (UB, 5 mins) Nitrogen gas		
2	PMMA Coating	a	Spin coating (4000 rpm, 1min) Photoresist: PMMA 649.04		
3	Baking	a	Heating (120 °C, 30 mins)		
4	Cr deposition	a	Cr (20 nm), evaporation		
5	Lithography	a	E-beam writing (300 μC/cm ²)		
6	Cr etching	a b c	Etching (chemical, 15 s) Rinsing(DI-water, UB, 10 mins) Nitrogen gas		
7	Development	a b c	AR-600-55(shaking, 2 mins) Isopropanol (UB, 1 min) Nitrogen gas		
8	Deposition Evaporation	a b	Ti (5 nm) Pt(25 nm)		
9	Lift-off	a b c	Aceton (5 mins) Isopropanol (1 min) Nitrogen gas		

3.5. Electronic characterization

In this section, the setup for electronic characterization of the $\text{Na}_{1+x}\text{NbO}_{3+\delta}$ films is sketched and the theoretical model, the partial capacitance model, that is used to derive the permittivity of the sample, is introduced.

3.5.1. Experimental setup

All electronic characterizations of our $\text{Na}_{1+x}\text{NbO}_{3+\delta}$ films are performed in a cryostat which is equipped with the self-made Pt-heater (see Chapter 3.3.3), in order to extend the temperature regime to 4 K – 700 K. A simplified sketch of the experimental setup is shown in Fig. 3.13.

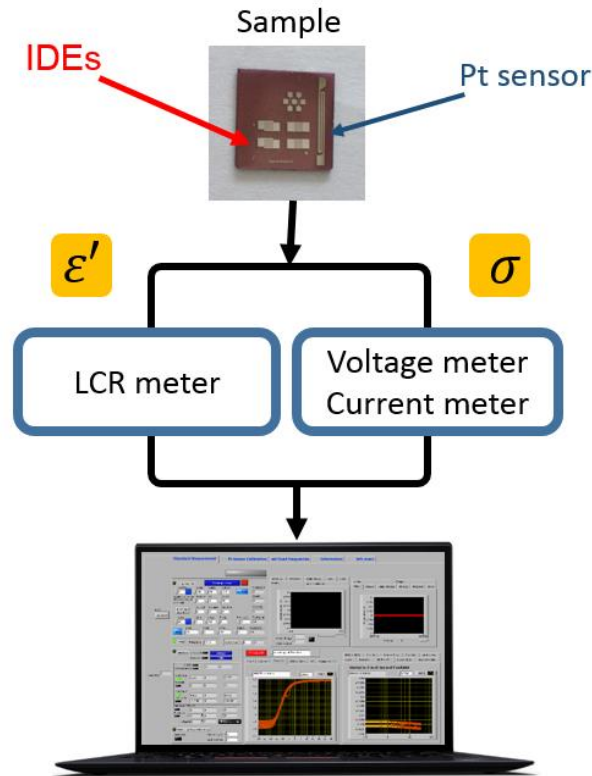


Fig. 3.13: Sketch of the setup of the electronic measurements for the capacitive and resistive characterizations.

Fig. 3.14 shows the different components of the setup, these are:

- (i) The sample carrier (a-c) with the Pt heater (a), the sample (b) with bondwires for the contact, and a bulky ceramic cap (c) that thermally protects the cryostat when the heater operates at temperature $T > 320$ K.
- (ii) The sample holder (d) that is installed in the cryostat (e) with special BNC connections for the capacitive measurements.

-
- (iii) The complete measuring setup consists of a cryostat, a small magnet (not used in this work), pumps, He tank, and the electronic equipment. The following electronic equipment was used: a temperature controller (Lakeshore332), a high precision capacitance meter (HP4278A), a LCR meter (ST2826A), a current/voltage source (Keithley2400), sensitive digital voltmeters (Keithley182 and 196), and a sensitive multimeter (Keithley2000).
- (iv) Finally, a computer controls the whole experiment (except for the liquid He-flow and the pump rate) and collects all data (Fig. 3.15). For this purpose a special Lab-view program was developed that allows continuous measurements for 24h, 7days a week.

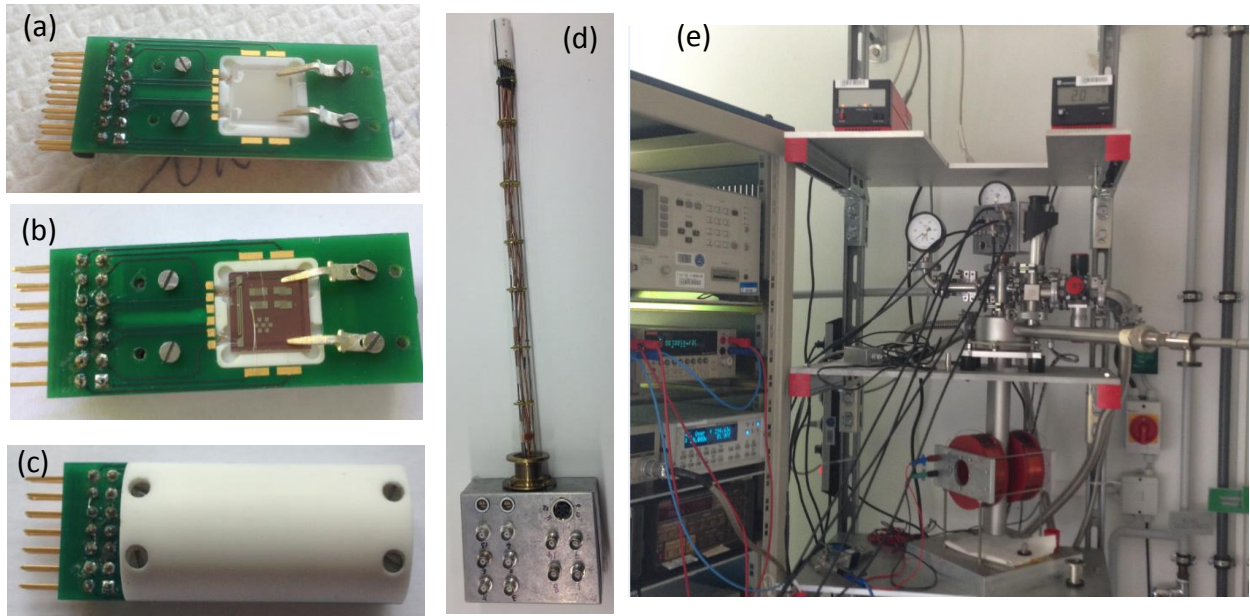


Fig. 3.14: Schematic illustrations of the procedure of sample installation. Mount a backside Pt heater (a), then add the sample with Al bondwires as electronic connection (b), close the holder with a ceramic heat protection(c), fix it on the top of a holder for the carrier (d), and install all in a cryostat (e).

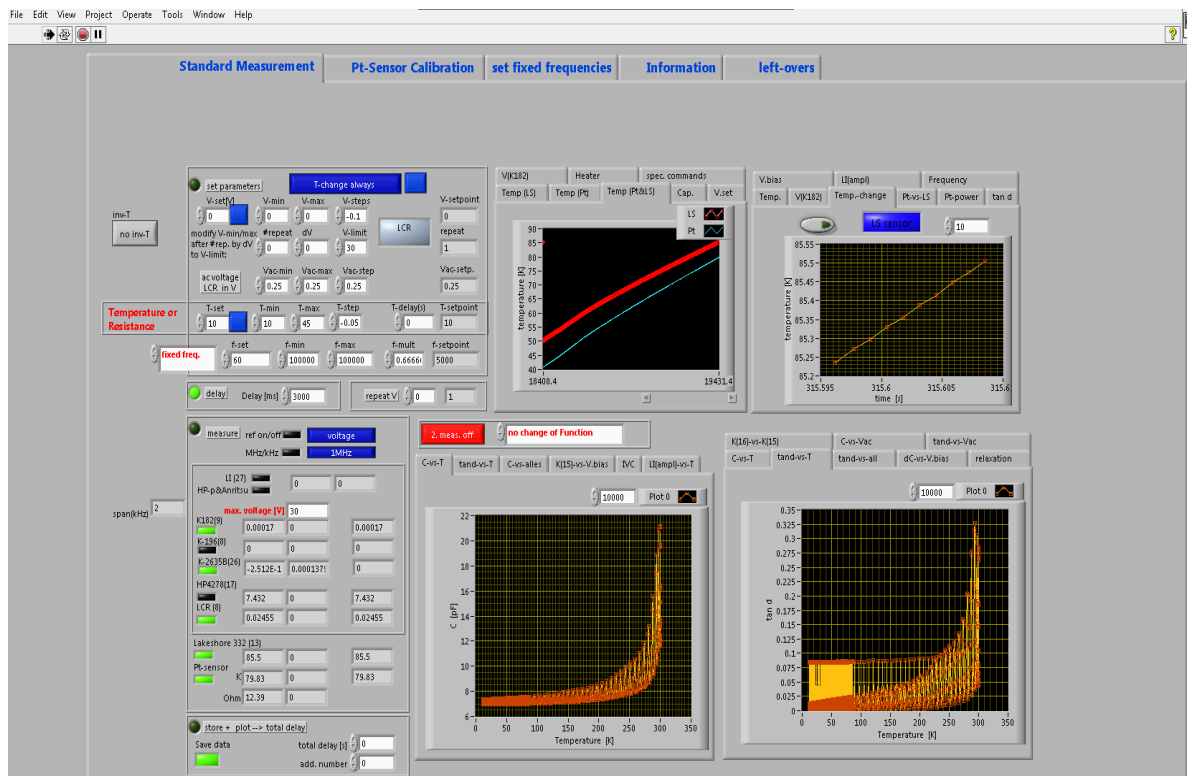


Fig. 3.15: Screenshot of the control panel developed in Lab-view for the electronic measurements in this thesis.

3.5.2. Capacitive measurements and evaluation

The main concept of electronic measurements is the measurement of the permittivity of the films. This is done via measurement of the capacitance of the respective interdigitated electrodes (IDEs) using a capacitance meter (HP4278A) or a LCR meter (ST2826A). In order to obtain the permittivity of the strained film, from this data, the so-called “partial capacitance model” is used.

3.5.2.1. Partial capacitance model

The “partial capacitance model” [103-105] describes the capacitive behaviors of planar capacitor by:

- (i) dividing the total capacitance into the different contributions and

- (ii) describing the different contributions for instance via elliptical integral or conformal mapping.

Fig. 3.16(a) shows a typical planar capacitor consisting of two planar electrodes, on top of the film that has to be examined, and the substrate. In our case the electrodes resemble two adjacent fingers of the two opposing IDEs, the film would be our $\text{Na}_{1+x}\text{NbO}_{3+\delta}$ films, and the substrate would be the (110) NdGaO_3 . An electric field applied between both electrodes automatically generates a field above, between, and below the electrodes leading to capacitive contributions from the air above and between the electrodes, from the film, and from the substrate. Including the contribution of the electronics (e.g. BNC cables), the total capacitance is given by the parallel arrangement of all components (see Fig. 3.16(b)):

$$C_{total} = C_{film} + C_{substrate} + C_{air} + C_{setup} \quad (3.4)$$

where C_{film} , $C_{substrate}$, C_{air} , and C_{setup} represent the capacitance of the film, substrate, air, and the electronic device (i.e. cables), respectively. Fig. 3.16 shows a sketch of a planar capacitor and the corresponding electric circuit that motivate the partial capacitance model, i.e. Eq. (3.4).

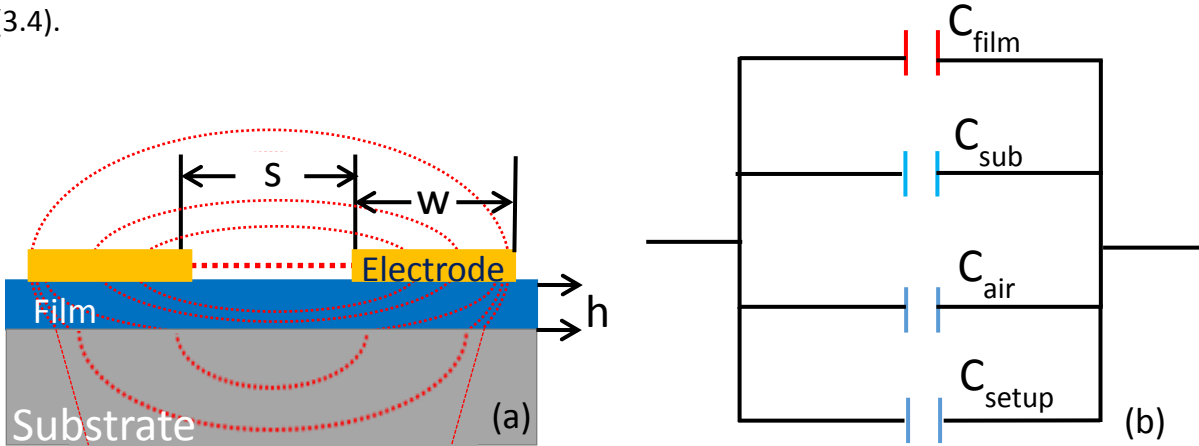


Fig. 3.16: Schematic sketch of the electric field distribution in our sample (a), and resulting electric circuit (b). The red dash lines represent the electric field lines, s , w , and h represent the gap between two adjacent electrodes, the width of the electrode, and the thickness of the film, respectively. (b) shows the corresponding electric circuit of the system corresponding to 4 capacitors connected in parallel.

For our experiment we can simplify this calculation by using a reference sample with identical substrate and IDE design, but without the film. The capacitance of such a reference is given by:

$$C_{reference} = C_{substrate} + C_{air} + C_{setup} \quad (3.5)$$

Therefore, the capacitance of the film is simplified as:

$$C_{film} = C_{total} - (C_{substrate} + C_{air} + C_{setup}) = C_{total} - C_{reference} \quad (3.6)$$

Fig. 3.17 shows, the reference measured for a (110)NdGaO₃ substrate for the IDEs oriented along the long ([1 $\bar{1}$ 0]) direction and the short ([001]) direction of the substrate.

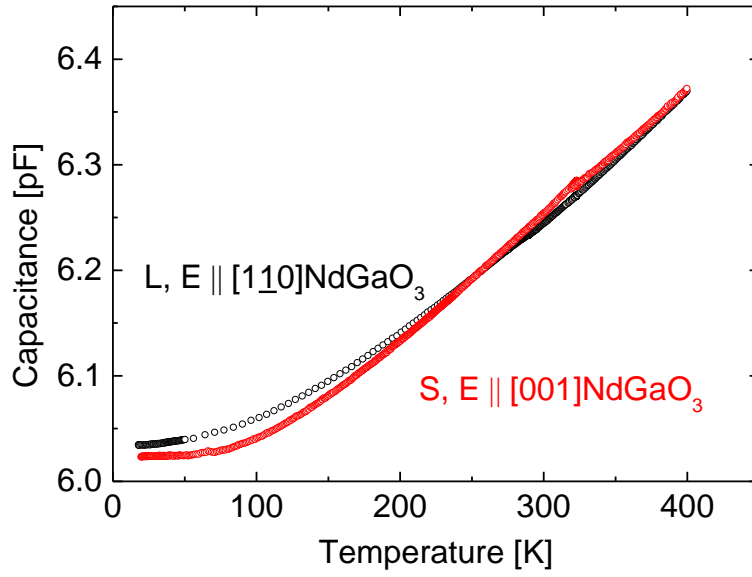


Fig. 3.17: Reference capacitance as function of temperature of a NdGaO₃ substrate for the large (black) and short (red) directions, i.e. E || [1 $\bar{1}$ 0]NdGaO₃, and E || [001]NdGaO₃, respectively.

3.5.2.2. Approximation of planar capacitor model

With the help of the reference measurement the capacitive contribution of the film can be derived from the measurement of C_{total}. The real part of the permittivity ϵ'_{film} of the film is then given by [103]:

$$C_{film} = \frac{1}{2} \cdot \epsilon'_{film} \cdot \epsilon_0 \frac{K(k')}{K(k)}, \quad k' = \sqrt{1 - k^2} \quad (3.7)$$

where ϵ_0 represent the vacuum permittivity, $K(k)$ is the total elliptic integral, and k is the modulus of the elliptic integral.

Via conformal mapping, this equation can be transformed into [103]:

$$C_{film} = \frac{\epsilon'_{film} \cdot \epsilon_0 \cdot l}{\frac{s}{h} + \frac{4}{\pi} \cdot \ln 2} \quad (3.8)$$

where s , h , and l are the gap between the electrodes (in our case $5\mu\text{m}$), the thickness of the film, and the length of the electrode. In our case we work with IDEs. The effective length is given by the integrated length of the electrode structure, i.e. $63 \times 700 \mu\text{m} = 44.1 \text{ mm}$. The conformal mapping used for Eq. (3.8) is restricted to certain conditions:

- (i) $s \leq 2w/3$, (for our design with $s = 5\mu\text{m}$ and $w = 10\mu\text{m}$ (see Fig. 3.16(a)), this condition is fulfilled.) and
- (ii) $s \geq h$ (which is definitely true in our case).

A further simplification of Eq. (3.8) can be obtained for $s \gg h$. In this case, $s/h \gg \frac{4}{\pi} \cdot \ln 2 \approx 0.88$ and Eq. (3.8) can be represented as:

$$C_{film} \approx \frac{\epsilon'_{film} \cdot \epsilon_0 \cdot l \cdot h}{s} \quad (3.9)$$

which is actually identical to the expression describing a classical parallel plate capacitor.

Since the total loss also consists of contributions from individual components, it is expressed as:

$$\tan \delta_{total} = \sum \frac{C_{individual}}{C_{total}} \tan \delta_{individual} \quad (3.10)$$

Therefore the resulting loss of the ferroelectric film is given by:

$$\tan \delta_{film} \approx \frac{C_{total} \tan \delta_{total} - C_{reference} \tan \delta_{reference}}{C_{film}} \quad (3.11)$$

The imaginary part ϵ'' of the dielectric constant of the film is obtained from the loss tangent $\tan \delta$ of the layer according to:

$$\tan \delta_{film} = \frac{\epsilon''_{film}}{\epsilon'_{film}} \quad (3.12)$$

4. Engineering of ferroelectric properties of NaNbO_3 via strain

Since the discovery of ferroelectricity in 1920, a large number of ferroelectric materials ranging from hydrogen-bonded crystals to double oxides (e.g. titanate or niobate) were identified, which show extraordinary dielectric, pyroelectric, elasto-electric, or opto-electric properties and, therefore, are of interest for technical applications [53]. Especially in thin film form, double oxide ferroelectrics and, more generally, polar materials are used nowadays in memories, sensors, actuators, and rf devices [47].

However, these ferroelectrics show most of their profound features typically in a temperature regime close to the phase transition temperature from the dielectric to ferroelectric state. In this temperature regime, for instance, the largest permittivity, piezoelectric effect, or tunability are present. Unfortunately, this transition temperature is usually far from room temperature, e.g. $T_C \approx 37$ K for SrTiO_3 [85], 403 K for BaTiO_3 [86], 503 to 760 K (depending on the composition) for $\text{PbZr}_{1-x}\text{Ti}_x\text{O}_3$ [87], 763 K for PbTiO_3 [88], and 628 K for NaNbO_3 [16], respectively. Therefore, it is of great interest to modify the phase transition temperature. This engineering of T_C can be achieved via strain, doping, or a combination of both. Especially in case of epitaxial ferroelectric films, the application of strain has been proven to be very successful. During the epitaxial growth, the lattice mismatch between substrate and film automatically induces tensile or compressive strain in the film. This has been demonstrated among others for a number of perovskites [6-13], tungsten bronzes [106], and bismuth layer-structured ferroelectrics [107].

In this chapter we focus on the impact of the in-plane strain on the engineering of Curie temperature and the ferroelectric properties of epitaxially grown NaNbO_3 on $(110)\text{NdGaO}_3$. Moreover, we demonstrate that the anisotropy of the in-plane strain leads to a large anisotropy in all ferroelectric properties ranging from the permittivity, Curie temperature, to the relaxor properties. Finally dc dependent measurements are applied to conduct a first analysis of the ferroelectric state in the strained NaNbO_3 films. A relaxor behavior is observed in the examined samples. A detailed discussion of the relaxor ferroelectric state will follow in Chapter 5.

4.1. Structural properties: epitaxy, strain and strain relaxation

NaNbO₃ films with different thickness are deposited via liquid delivery spin metal organic chemical vapor deposition (MOCVD) on (110) oriented single-crystalline NdGaO₃ substrates. A detailed description of the MOCVD deposition technique, the deposition parameters and structural properties of the film are given in chapter 3.

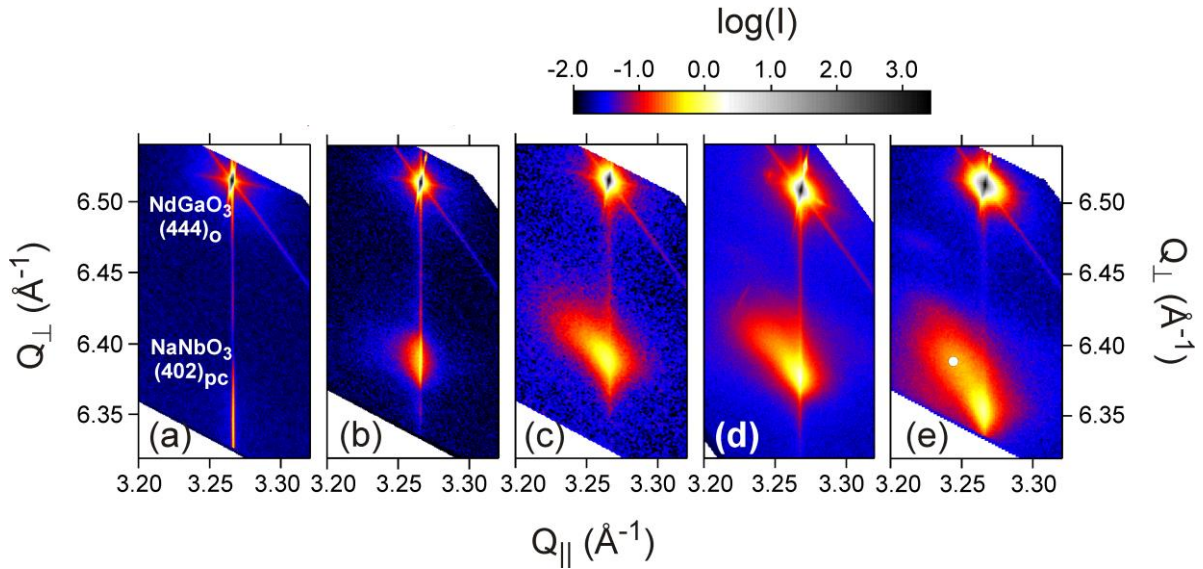


Fig. 4.1: High resolution x-ray diffraction RSM in the vicinity of the (444)_o Bragg reflection of the NdGaO₃ substrate for a 11 nm (a), 27 nm (b), 63 nm (c), 80 nm (d), and 140 nm (e) thick sample. The circle in (e) marks the position of the corresponding (402)_{pc} reflection of unstrained NaNbO₃.

Fig. 4.1 illustrates the impact of the lattice mismatch between the substrate and film on the structure, strain and strain relaxation of the NaNbO₃ films. It shows a series of reciprocal space maps (RSM) in the vicinity of the asymmetric (444)_o Bragg reflection of the orthorhombic NdGaO₃ substrate for a series of NaNbO₃ films of different thickness. All RSM patterns prove the epitaxial growth of the films, i.e. the in-plane component of the scattering vectors of the (444)_o Bragg reflection Q_{\parallel} of NdGaO₃ and of the main intensity of the (402)_{pc} Bragg reflection of the NaNbO₃ films coincide. This demonstrates that all films are strained, their in-plane lattice parameters adapt the substrate's lattice at the interface. However, only for the thinnest film ($d = 11$ nm, Fig. 4.1(a)) the film reflection peak is symmetric. Already for the 27 nm thick film the (402)_{pc} reflection peak of the film slightly broadens asymmetrically to the left side (Fig. 4.1(b)) and with further increasing film thickness the film contribution expands more and more towards lower Q_{\parallel} values, i.e. larger in-plane lattice parameters (Figs. 4.1(c) – (e)). This is

clearly noticeable for the 140 nm film in Fig. 4.1(e) where the film reflection peak spreads towards the corresponding reciprocal lattice point of unstrained NaNbO_3 marked by the white circle. This observation is an indication for a partial plastic relaxation of the strained lattice of the film.

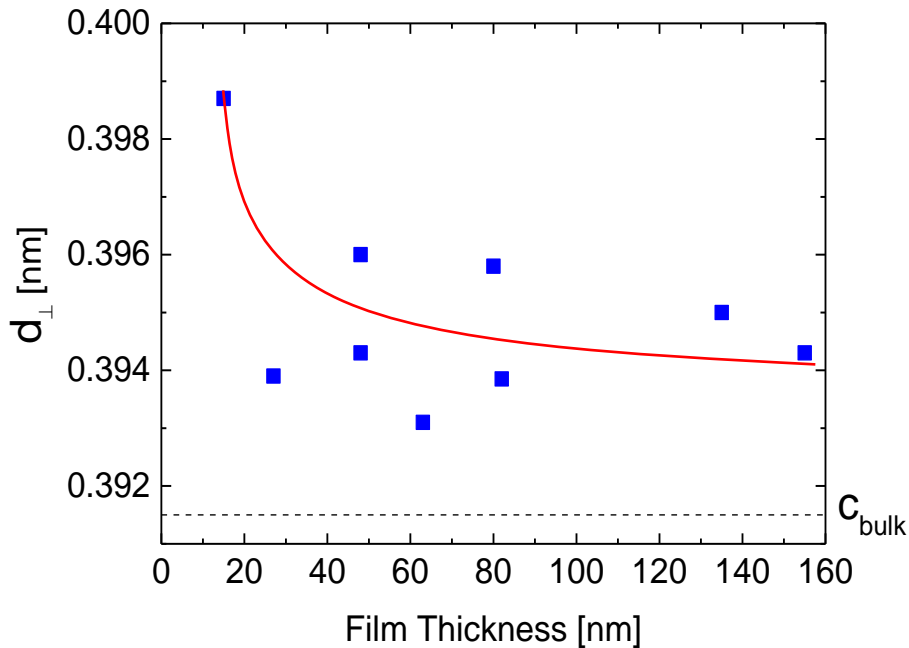


Fig. 4.2: Out-of-plane lattice parameter d_{\perp} of epitaxial NaNbO_3 films grown on (110) NdGaO_3 as function of film thickness. The dash line represents the c -axis parameter of unstrained NaNbO_3 . The red line serves as a guide for the eye for the thickness dependence of d_{\perp} . Adapted from [52].

This strain relaxation can also be obtained in the out-of-plane component. Typically the in-plane strain is partially compensated by an out-of-plane modification of the lattice parameter. In case of the compressively strained NaNbO_3 , the out-of-plane lattice parameter is elongated with respect to the literature value. Fig. 4.2 shows the out-of-plane lattice parameter d_{\perp} of a series of NaNbO_3 films of different thickness deposited on NdGaO_3 . Generally the lattice parameter is larger than the literature value of 0.3915 nm [43]. With increasing film thickness, it decreases even for films with very small thickness. It should be noted, that these values represent integral value of d_{\perp} . Nevertheless it nicely confirms the partial relaxation of the compressive strain [52]. This process starts at a critical thickness of approximately 15 – 20 nm [52] and becomes more prominent with increasing thickness. Even for a very thick sample, i.e.

155 nm, d_{\perp} is still larger than the c-axis bulk lattice parameter. This is a good indication that even the very thick films are still partially strained.

4.2. Electronic properties

The ferroelectric properties of these films are determined via capacitor structures using interdigitated electrodes (IDEs). Two different orientations of IDEs are prepared on each sample, which allow to determine the ferroelectric properties for electric field E with orientations along the longer axis ($E \parallel [1\bar{1}0]\text{NdGaO}_3$) and the short axis ($E \parallel [001]\text{NdGaO}_3$), respectively. In the following the orientations are simply denoted by the length of the axis along which the electric field is oriented. In this section, we will exemplarily discuss the properties of one direction, i.e. the ferroelectric properties for the “short axis”. In section 4.3, we will discuss the anisotropy of the ferroelectric properties, which includes both directions.

In contrast to the polycrystalline unstrained NaNbO_3 , the temperature dependences of the permittivity ϵ' of the compressively strained NaNbO_3 films (Fig. 4.3) show distinct and broad peaks at low temperature which are indicative of a phase transition from a relaxor-type ferroelectric at low temperature to the dielectric state at high temperature [9-11] (The relaxor properties will be discussed in detail in chapter 5). The temperature of maximum permittivity, T_{max} , can be used as a first approximation of the temperature of the phase transition from the ferroelectric-to-dielectric phase transition. The compressive strain induced by the lattice parameter mismatch between the epitaxially grown film and the substrate leads to:

- (i) a reduction of the temperature of maximum permittivity from that of unstrained polycrystalline NaNbO_3 at $T_{\text{max}} = 620 - 660$ K [17] to temperatures of $T_{\text{max}} = 125 - 147$ K for the films of thicknesses ranging from 27 nm to 80 nm, and
- (ii) an enhancement of the permittivity up to 1500 at T_{max} in comparison to $\epsilon'(T < 300 \text{ K}) \lesssim 250$ of unstrained bulk material [17].

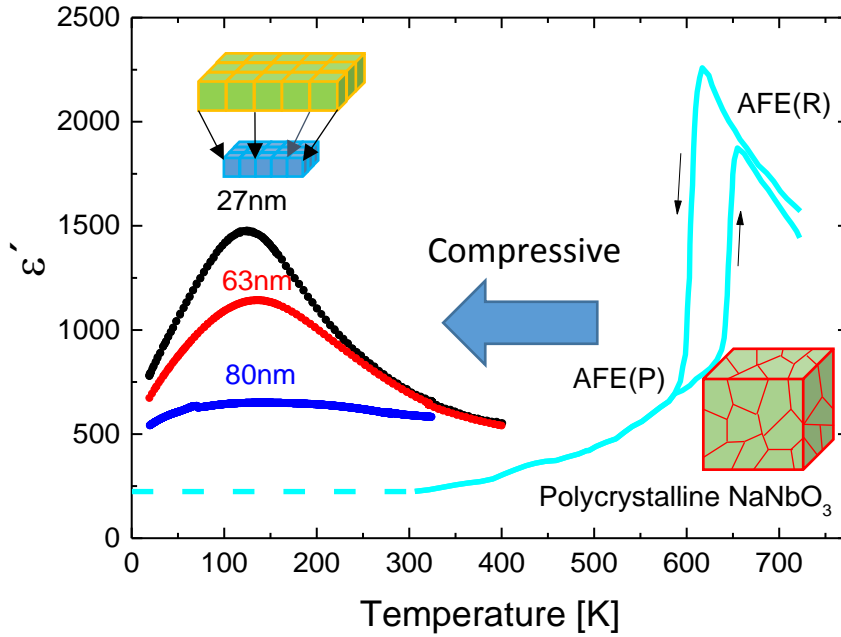


Fig. 4.3: Temperature dependence of the permittivity of NaNbO_3 films of different thickness that are epitaxially grown on (110) NdGaO_3 . The data are recorded at 1 MHz using a small ac electric field ($E_{ac} = 0.048 \text{ V}/\mu\text{m}$) along the short axis of the substrate, i.e. $E \parallel [001]\text{NdGaO}_3$. The cyan line represents the dielectric constant of unstrained polycrystalline NaNbO_3 bulk material with a phase transition from the P-phase antiferroelectric (AFE) to the R-phase antiferroelectric state around 620 – 660 K [17]. The extension of the data to 0K (dash line) represents the expected permittivity at low temperature. Note, that we only measure the in-plane component of the permittivity of epitaxial films.

Both effects strongly depend on the thickness of the NaNbO_3 film (see Fig. 4.4). With increasing thickness, the maximum permittivity ϵ'_{max} decreases, whereas T_{max} increases. Both effects can be explained by the partial relaxation of the lattice strain in the film that was demonstrated by XRD measurements (see Fig. 4.1 and 4.2). The largest strain is present in the thinnest film which possesses the lowest $T_{max} \approx 125 \text{ K}$ and the largest $\epsilon'_{max} \approx 1500$. With increasing thickness partial plastic lattice relaxation sets in. As a consequence, the reduction of transition temperature becomes smaller, i.e. T_{max} increases. Moreover, the distribution of the strain (i.e. completely strained bottom layer relaxes towards the film surface) increases with increasing thickness. This leads to a broadening of the peak and, thus, a decrease of ϵ'_{max} with increasing thickness. Already at a thickness of 80 nm the strain leads only to a relatively small enhancement of the permittivity of $\epsilon'_{max} \approx 650$. This is not only caused by the progressive relaxation of the film, it is additionally enforced by the arrangement of the measurement. The

planar set of IDEs predominantly records the permittivity of the top layer of the film which represents the more relaxed part of the film.

The compressive strain engineered at the interface between the NaNbO_3 film and NdGaO_3 substrate is supposed to be responsible for the occurrence of a phase transition at low temperatures in these strained NaNbO_3 films on NdGaO_3 . This phase transition could be:

- (i) a “new” phase transition which does not occur in the unstrained material or
- (ii) a known phase transition (e.g. the phase transition at ~ 620 K) that is shifted to lower temperature due to the strain.

The strain relaxation also plays an important role in the modification of the ferroelectric features (see Fig. 4.4).

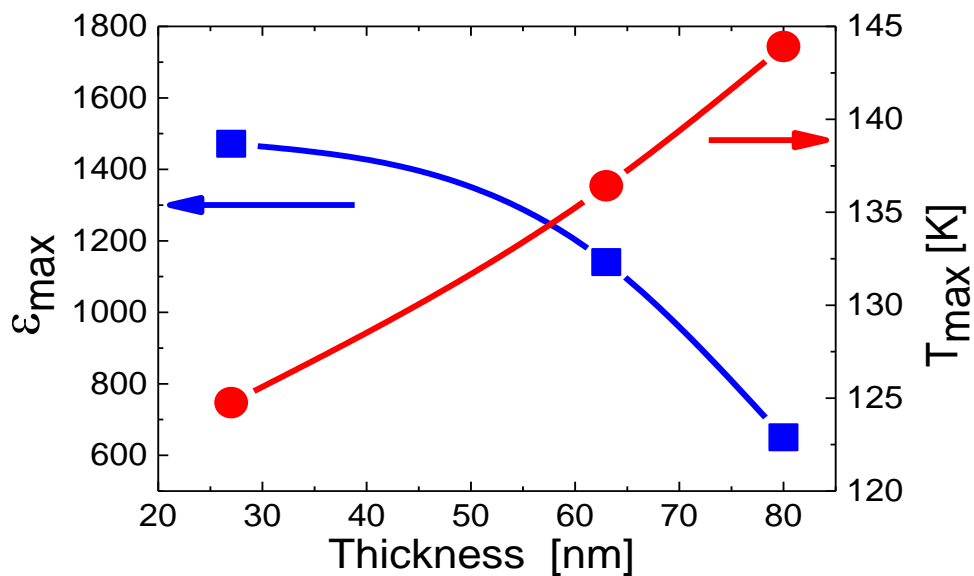


Fig. 4.4: Maximum dielectric constant ϵ'_{\max} (blue squares) and corresponding temperature T_{\max} (red circles) as function of film thickness for the NaNbO_3 film shown in Fig. 4.3 ($E \parallel [001]\text{NdGaO}_3$).

4.3. Anisotropy

In the previous section we demonstrated that compressive strain can either induce a ferroelectric transition at low temperatures or shift an existing ferroelectric transition towards

low temperatures. Due to their structures, the substrate, (110)NdGaO₃, offers different directions with different in-plane lattice parameters, that automatically results in different resulting in-plane strain.

This difference in strain can not only results in anisotropic structural and electronic properties, it might also help to understand the mechanism that is responsible for the phase transition at low temperature created by the strain in our NaNbO₃ films.

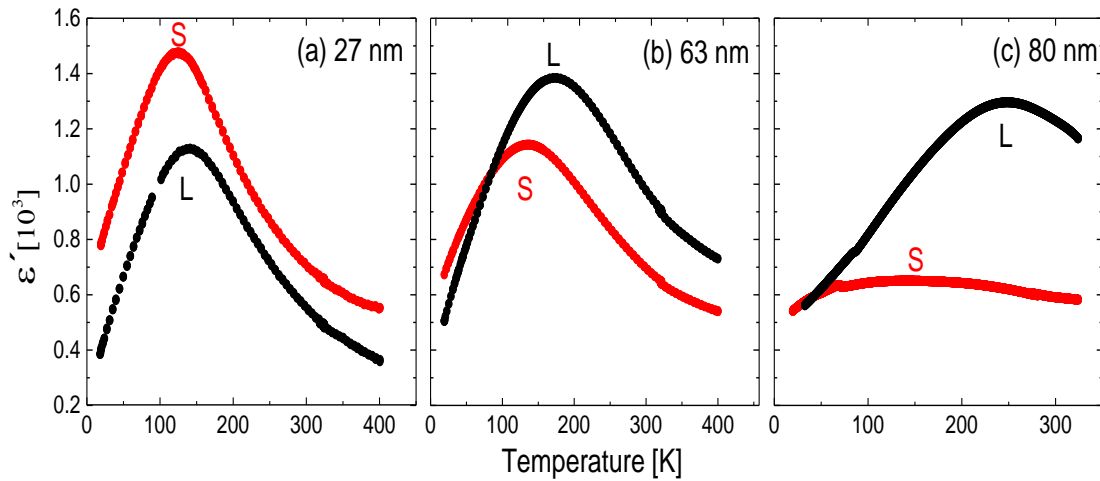


Fig. 4.5: Permittivity as function of temperature recorded along the long (black, L) axis and the short axis (red, S) for NaNbO₃ thin films on NdGaO₃ with a thickness of 27 nm (a), 63 nm (b) and 80 nm (c), respectively. All the data are measured at 1 MHz using a small ac electric field of $E_{ac} = 0.048 \text{ V}/\mu\text{m}$.

Fig. 4.5 shows the temperature dependence of the permittivity of strained NaNbO₃ thin films with different thickness which are epitaxially grown on (110) NdGaO₃. The results for the experiment with E oriented along the large axis are added to the data shown in Fig. 4.3. The measured loss tangent values (not shown) are typically below 0.05 which indicates that the measured dielectric constant is reliable. A huge anisotropy in the permittivity can be observed in all three samples (see Fig. 4.6). Values up to $\epsilon'(L)/\epsilon'(S) \approx 2.1, 1.4,$ and 0.8 are obtained for 80 nm, 63 nm and 27 nm thick NaNbO₃ films, respectively.

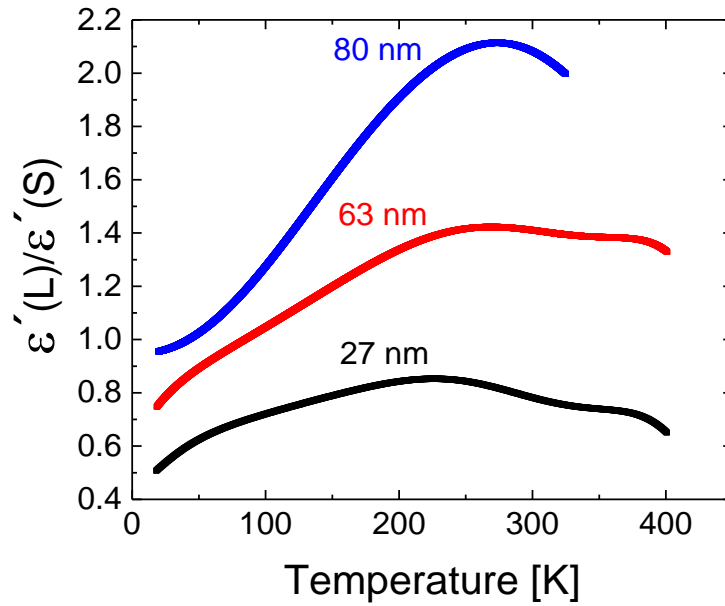


Fig. 4.6: Anisotropy of the permittivity for the NaNbO_3 films with different thickness, i.e. 27 nm (black), 63 nm (red) and 80 nm (blue).

For the discussion of the anisotropic properties in detail, the values of ϵ'_{\max} and T_{\max} recorded along the two different crystalline orientations of NaNbO_3 are summarized in Fig. 4.7. Let us concentrate on the behavior of T_c , the temperature that characterizes the temperature of the phase transition. There are two major observations:

- (i) T_{\max} increases with increasing thickness of the film and
- (ii) T_{\max} is always larger for the electric field oriented along the larger axis of NdGaO_3 .

The first observation simply reflects the partial plastic relaxation of the film (see Fig. 4.1 and 4.2) which increases with increasing thickness. It represents another argument for the hypothesis that strain can lead to a significant temperature shift of phase transition in these materials.

The second observation is actually surprising. According to classic model, we would expect the opposite behavior, i.e. $T_{\max}(S) > T_{\max}(L)$. In order to elucidate this contradiction, let us first consider the “classical model” which explains the orientation of NaNbO_3 on NdGaO_3 by

minimizing the energy of NaNbO_3 crystal that is structurally adapting the $(110)\text{NdGaO}_3$ structure.

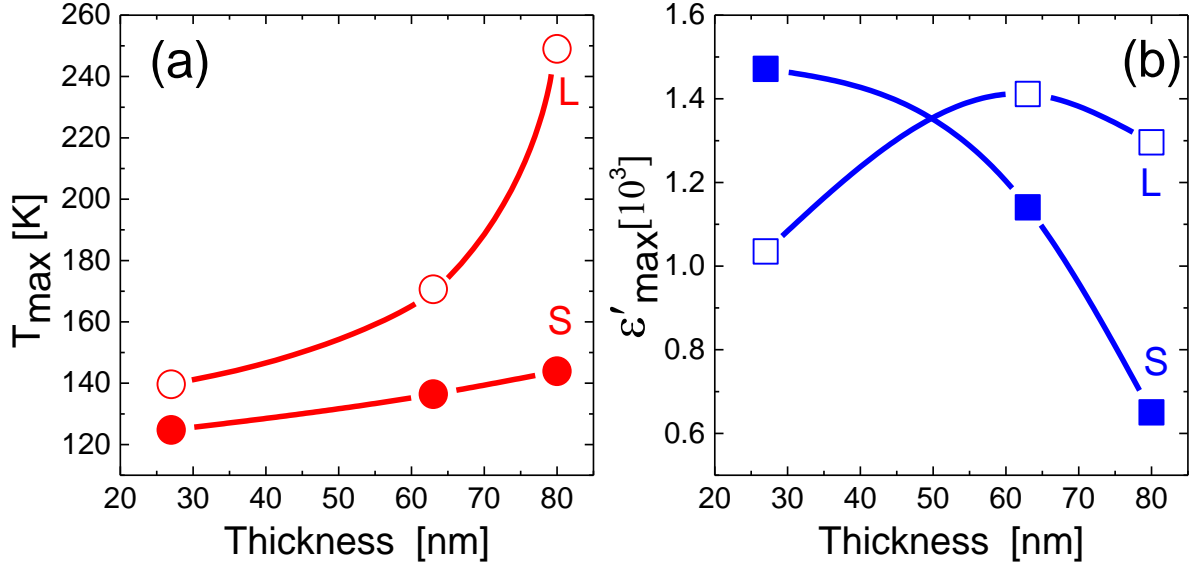


Fig. 4.7 (a) T_{\max} (red circles) and (b) corresponding maximum dielectric constant ϵ'_{\max} (blue squares) of NaNbO_3 thin films for E oriented along the small (S, solid symbols) and large (L, open symbols) axis directions as function of film thickness.

Classical model:

NdGaO_3 : At room temperature the crystal structure of the substrate NdGaO_3 is orthorhombic ($a_{\text{NGO}} = 0.5428$ nm, $b_{\text{NGO}} = 0.5498$ nm, $c_{\text{NGO}} = 0.7709$ nm) [108] and the (110) surface exhibits an only nearly squared in-plane lattice with lattice parameters 2×0.3854 nm and 2×0.3863 nm in $[001]$ and $[1\bar{1}0]$ direction, respectively. The lattice parameter of the “long axis” ($[1\bar{1}0]$ NdGaO_3) is 0.23% larger than that of the “short axis” ($[001]\text{NdGaO}_3$). Onto this not perfect square lattice the NaNbO_3 film is deposited, which itself is orthorhombic.

NaNbO_3 : At room temperature the orthorhombic unit cell lattice parameters of bulk NaNbO_3 are $a_{\text{NNO}} = 0.55047$ nm, $b_{\text{NNO}} = 0.55687$ nm, and $c_{\text{NNO}} = 1.5523$ nm, respectively [42]. For simplicity NaNbO_3 is often presented in pseudocubic notation with the corresponding pseudocubic lattice parameters $a^{\text{pc}}_{\text{NNO}} = 0.3881$ nm and $b^{\text{pc}}_{\text{NNO}} = c^{\text{pc}}_{\text{NNO}} = 0.3915$ nm [43]. Note that the surface normal and in-plane directions of the NdGaO_3 substrate and the NaNbO_3 film refer to the orthorhombic and pseudocubic notation, respectively.

NaNbO₃ on NdGaO₃: Due to energy minimization NaNbO₃ is expected to grow with the smallest possible distortion on NdGaO₃ which is achieved by the *c*^{pc}-orientation of the NaNbO₃ film and the *a*^{pc}-axis and *b*^{pc}-axis of NaNbO₃ along [001]NdGaO₃ and [11̄0]NdGaO₃, respectively. The resulting lattice mismatch

$$\beta = (2a_{film} - a_{sub})/a_{sub} \quad (4.1)$$

in *a*^{pc}- and *b*^{pc}-direction is compressive and highly anisotropic, i.e. ~0.70% and ~-1.35%, respectively (see Table 4.1). Here *a*_{film} and *a*_{sub} represent the pseudocubic lattice parameters in *a*^{pc} or *b*^{pc} direction of the film and the corresponding effective in-plane lattice dimensions in [001] or [11̄0] direction of the substrate. Furthermore, the resulting experimentally determined strain

$$\eta = (a_{film-exp} - a_{film})/a_{film} \quad (4.2)$$

is compressive in *a*^{pc}- and *b*^{pc}-direction (e.g. -0.70% and -1.33%) and tensile in *c*^{pc}-direction (e.g. 0.77%) (see table 4.1). Here *a*_{film-exp} and *a*_{film} represent the experimentally determined lattice parameter and the lattice parameter of unstrained NaNbO₃, respectively.

Table 4.1: Lattice parameters [43, 108], resulting lattice mismatch, and experimentally determined strain for an epitaxial grown NaNbO₃ film on NdGaO₃. Theoretical values are given in black, experimental values in red. The results according to square-lattice model are given in the brackets.

	Direction		Lattice parameter [nm]			Lattice mismatch β	Strain η
	NdGaO ₃	NaNbO ₃	NdGaO ₃	NaNbO ₃	NaNbO ₃		
in-plane	[001]	[100] ^{pc}	2 x 0.3854	0.3854	0.3881	0.70%	-0.70%
					(0.3898)	(1.14%)	(-1.13)
	[11̄0]	[010] ^{pc}	2 x 0.3863	0.3863	0.3915	1.35%	-1.33%
					(0.3898)	(0.91%)	(-0.90%)
out-of-plane	[110]	[001] ^{pc}		0.3945	0.3915		0.77%

According to this model the larger compressive strain (i.e. -1.33%) is actually expected for the larger axis, i.e. [11̄0]NdGaO₃. However, this larger compressive strain should lead to a strong reduction of T_{max}, which is not observed in the experiment.

The problem of this classical approach is actually that:

- (i) It only considers the structure of the unstrained NaNbO_3 at room temperature and
- (ii) that most likely the difference in energy for different structural configurations of NaNbO_3 is very small.

Actually it is not known and difficult to predict what happens during the deposition and phase formation of NaNbO_3 on NdGaO_3 at elevated temperature ($\sim 700^\circ\text{C}$). We believe it is most appropriate to assume that the NaNbO_3 actually adapts a square shaped in-plane structure at the interface to the substrate during the growth. The resulting strain in the growing film would then be directly related to the length of the axis of the substrate. This strain that is induced during the growth, would then be transferred to room temperature (and further on to the experimental temperature).

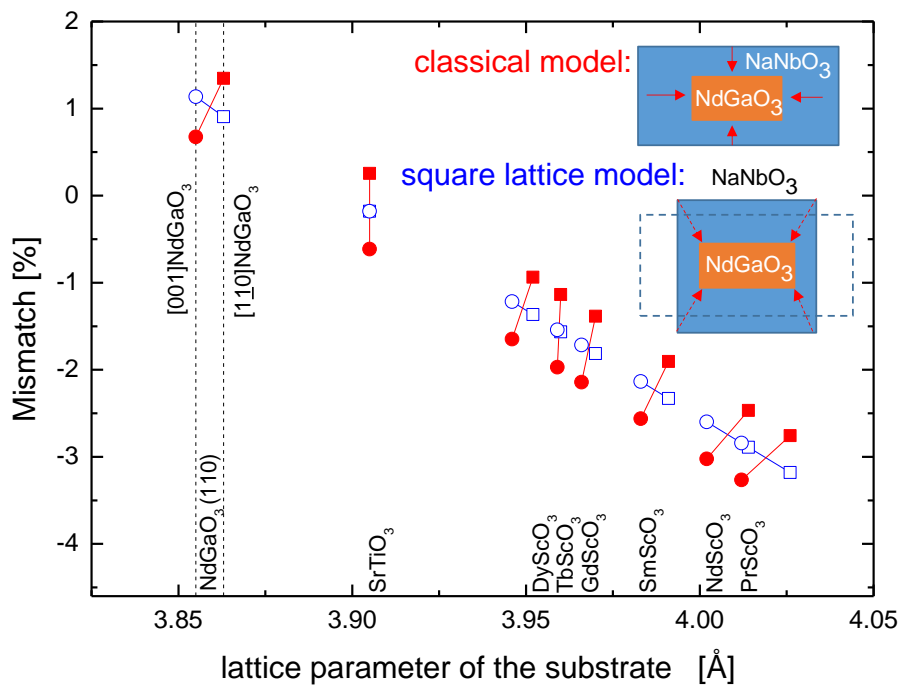


Fig. 4.8: Mismatches between the NaNbO_3 film and various substrates based on the classical approach (solid symbols) and “square lattice” model (open symbol) for the large direction (square) and small direction (circle). Sketches of the two models are given as insets.

In this way, a lattice mismatch of $\sim 1.14\%$ and $\sim 0.91\%$ and a compressive strain of $\sim -1.13\%$ and -0.90% are obtained for the short ($[001]$ NdGaO₃) and long axis ($[\underline{1}10]$ NdGaO₃), respectively (see data in brackets of table 4.1). The compressive strain is larger for the smaller NdGaO₃ axis and smaller for the larger NdGaO₃ axis which automatically explains the experimental observation, i.e. $T_{\max}(L) > T_{\max}(S)$ as shown in 4.7(a). The different models and the resulting lattice mismatches for NaNbO₃ on various orthorhombic substrates are sketched in Fig. 4.8. It was the plan to test this model by depositing NaNbO₃ on various scandates. However this project could not be completed during this PhD work.

4.4. Ferroelectric state

In this section we offer a first discussion on the ferroelectric state of the strained NaNbO₃ films trying to find out, whether the peak observed at low temperature represents a new induced phase transition or a shift of a known phase transition towards low temperature.

It is known that substrate-induced biaxial strain may significantly increase the spontaneous polarization and induce structural and, therefore, ferroelectric phase transitions in a ferroelectric material [6,7,14,15]. These effects not only depend on the amount of strain, but they are also strongly affected by the sign of the strain (compressive or tensile) and the electric field direction in which the polarization is measured. For example, it has been shown that tensile strain significantly increases T_c for in-plane polarization measurements on SrTiO₃ films, whereas compressive strain does not induce any spontaneous in-plane polarization in the same material [6,7]. In order to examine the ferroelectric state of the strained NaNbO₃ films, dc bias dependent measurements are performed.

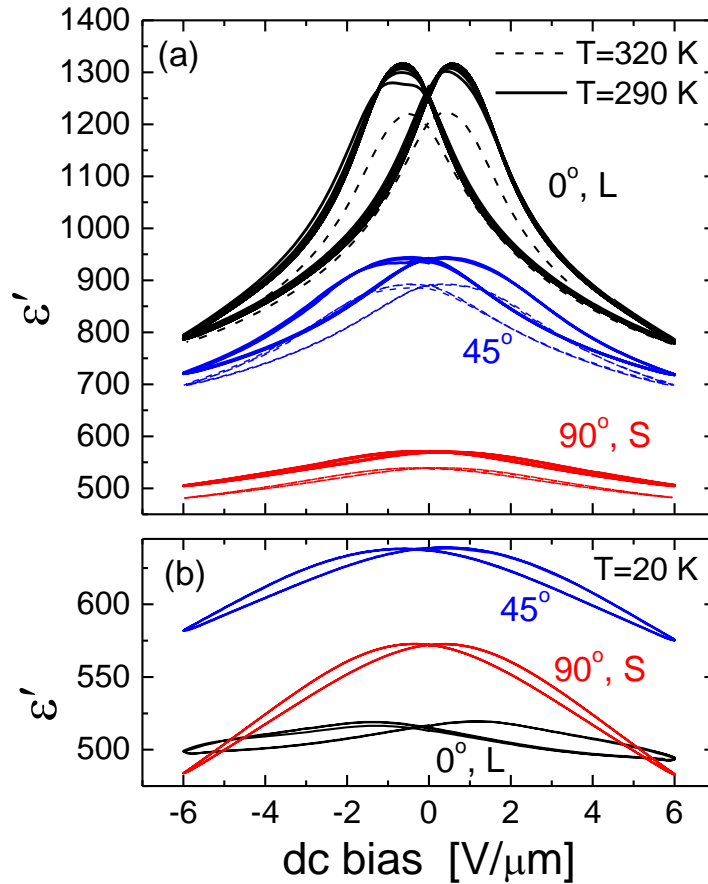


Fig. 4.9: Electric field dependence of the permittivity of the 80 nm thick NaNbO_3 on (110) NdGaO_3 measured at 1 MHz for different orientations α of the electric field E and different temperatures, i.e. 320 K (dashed lines in (a)), 290 K (solid lines in (a)), and 20 K (b). Here, α is defined as the angle with respect to the longer axis ($[1\bar{1}0]\text{NdGaO}_3$), additionally L and S are added for consistency.

Fig. 4.9 shows examples of the dc electric field dependence of the strained NaNbO_3 film for different temperatures and field orientations. The dc bias is oriented parallel to the ac field of the measurement. In all cases a butterfly shape is observed indicating the presence of spontaneous polarization and tunability. Spontaneous polarization has also been recorded by piezo force microscopy [109]. Nevertheless, it cannot be excluded, that the butterfly shape is also partially caused by the movement of domain walls [110]. At room temperature the tunability and spontaneous polarization (and, possibly, domain wall motion) are largest for the L direction (longer axis).

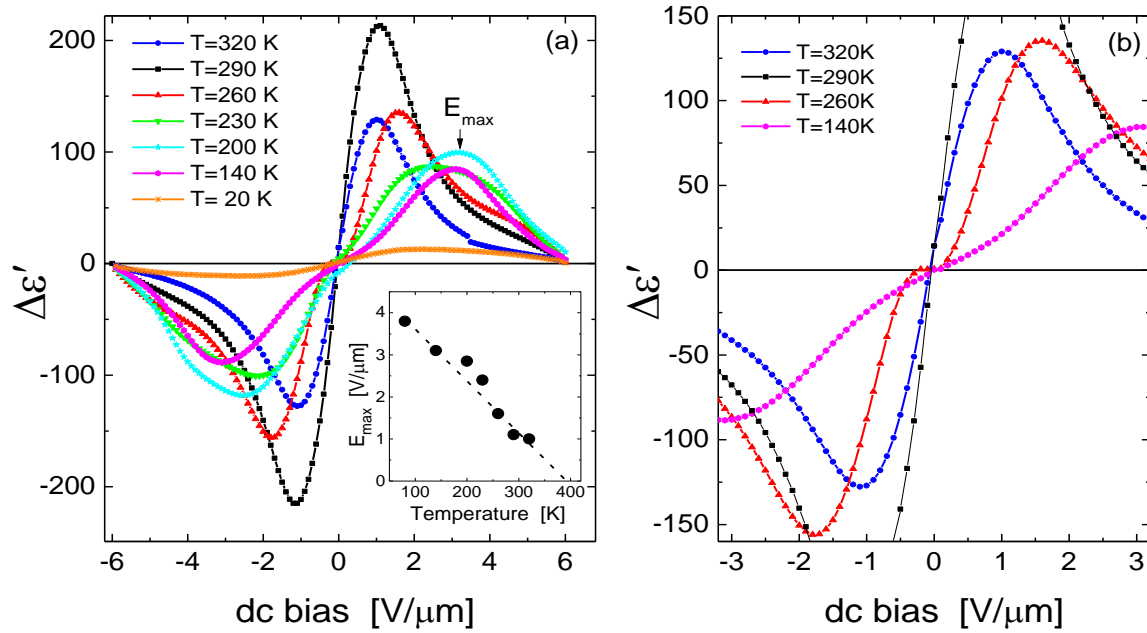


Fig. 4.10: Hysteretic behavior of the permittivity $\Delta\epsilon' = \epsilon'(\text{increasing bias}) - \epsilon'(\text{decreasing bias})$ of the 80 nm thick NaNbO_3 film on (110) NdGaO_3 (long axis) measured at 1 MHz for different temperatures. The inset in (a) represents the temperature dependence of the position of the maxima E_{max} as indicated by an arrow for one temperature, (b) represents an enlarged plot of the bias dependence of $\Delta\epsilon'$ around zero bias for selected temperatures.

More details of the ferroelectric properties of the sample can be obtained by the analysis of the hysteretic behavior of the bias dependence of the permittivity by analyzing $\Delta\epsilon' = \epsilon'(\text{increasing bias}) - \epsilon'(\text{decreasing bias})$. Fig. 4.10 shows $\Delta\epsilon'$ for the E oriented along the large axis. For all temperatures, $T < 400$ K, a spontaneous polarization is present. The maximum $\Delta\epsilon'_{\text{max}}$ at the electric fields E_{max} coincides with the coercive voltage of the ferroelectric film [111]. The temperature dependence of E_{max} (inset Fig. 4.10(a)) as well as the decrease of $\Delta\epsilon'_{\text{max}}$ above room temperature indicate, that the ferroelectric state will most likely disappear at higher temperatures. The linear decrease of E_{max} -versus- T (inset Fig. 4.10(a)) hints at a transition temperature close to 400 K.

A closer look at the dc-bias dependence of $\Delta\epsilon'$ (Fig. 4.10(b)) around zero bias reveals more details of the ferroelectric properties of the strained film. At high temperatures ($T > 270$ K), $\Delta\epsilon'$ shows the classic ferroelectric behavior, i.e. a linear increase around zero bias. However at lower temperature the bias dependence shows an 'S' shape which is indicative for an antiferroelectric behavior or antiferroelectric contributions. In particular, the data recorded

at 260K shows a clear plateau at zero bias, i.e. the film behaves antiferroelectric. At lower temperatures, the plateau inclines, i.e. there seems to be antiferroelectric and ferroelectric behavior at the same time. Finally at the lowest temperatures ($T < 100$ K, see Fig. 4.10(a)) the dependence is again linear. Either the antiferroelectric contribution has vanished or it is too small to be detected in our measurement.

4.5. Summary

In summary of this chapter we found:

- (i) Epitaxial films of NaNbO_3 can be grown on $(110)\text{NdGaO}_3$.
- (ii) Although partial strain relaxation sets in already for relatively thin films ($d \approx 10 - 15$ nm) all NaNbO_3 films (up to $d \approx 140$ nm) are still strained.
- (iii) The compressive strain leads to a significant enhancement of the permittivity for $T < 400$ K (maximum temperature of the electronic characterization) and a relaxor-type ferroelectric phase transition at low temperature. The relaxor behaviors is discussed in detail in next chapter.
- (iv) This phase transition is either a new phase transition induced by the strain or a known phase transition shifted to lower temperature due to the strain.
- (v) The orthorhombic structure of the substrate leads to an anisotropy in-plane strain and, thus, anisotropic ferroelectric properties.
- (vi) The “classical model” for the mismatch based on energy minimization and the room temperature lattice of unstrained NaNbO_3 cannot explain the shift of T_c with the strain. A new “square lattice” model is proposed, which nicely fits the experimental results.
- (vii) A first ferroelectric analysis indicates, that the NaNbO_3 films show signs of spontaneous polarization up to $T \approx 400$ K, which might be indications for ferroelectric, and antiferroelectric contributions. The latter indicates, that a more detailed analysis of the ferroelectric state is necessary. This will be given in the following chapter.

5. Relaxor behavior and polar nanoregions in strained NaNbO_3

As discussed in Chapter 4, the physical properties of NaNbO_3 thin films can substantially differ from those in bulk materials. Especially an epitaxial growth of the film onto a substrate with different lattice parameters can cause considerable compressive strain of the film structure that may change profoundly the phase transition sequence, Curie temperature and permittivity in thin films with respect to that of unstrained bulk material [6,7]. However, at the same time the strain can lead to defects in the film and cause a (slight) deviation from the perfect stoichiometry of the ferroelectric film. As a consequence, these films (with a most likely imperfect composition) actually show the typical characteristics of relaxor-type ferroelectrics [8-11].

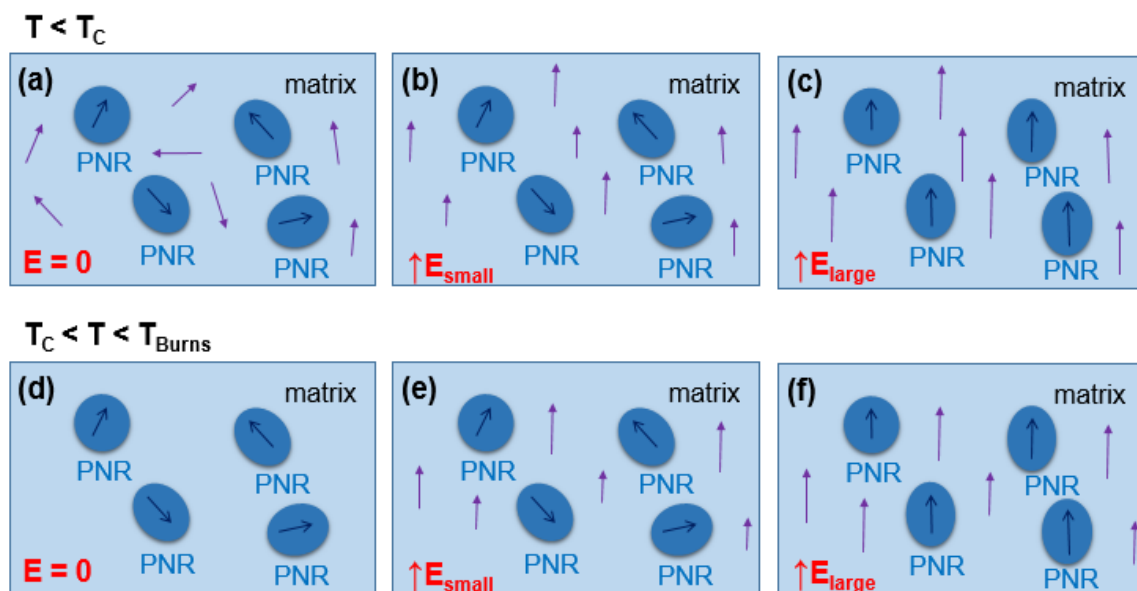


Fig. 5.1: Schematic illustration of the evolution of PNRs (blue) and matrix (light blue) for zero field ($E = 0$) and an applied electric field ($E \neq 0$) in relaxor-type ferroelectrics in the relaxor state ($T < T_C$) and in the paraelectric state below the Burns temperature ($T_C < T_{Burns}$).

Relaxor-type ferroelectrics recently attracted considerable scientific interest owing to their intriguing physics and their potentially high permittivity and tunability resulting in a number of potential applications [53]. Generally relaxor-type ferroelectrics are characterized by their frequency-dependent and broad peak in the temperature dependence of the permittivity that

is believed to be based on the formation of regions of uniform polarization, the so-called polar nano-regions (PNRs) [112]. Fig. 5.1 illustrates the PNRs which are randomly distributed in a non-spontaneously polarized ($T_C < T < T_{\text{Burns}}$) or spontaneously polarized ($T < T_C$) matrix in relaxor-type ferroelectrics. Here T_{Burns} represents the Burns temperature where all the PNRs start to vanish.

In classical relaxor-type ferroelectrics, such as lanthanum-doped lead zirconate titanate (PLZT) or lead magnesium niobate (PMN), it is assumed that secondary phases or inhomogeneities (chemical or structural) might be responsible for the formation of the PNRs [60, 63-65]. As a consequence the size of the PNRs is usually assumed to be associated with the extension of these secondary phases or inhomogeneities. The existence of both the polar cluster and the matrix into which the polar clusters are embedded in the relaxor-type state was demonstrated for instance by neutron scattering, NMR and X-ray diffraction experiments [64,113-116]. Whereas, for the interaction of the PNRs two major models are accepted [65,78], i.e. a dipole-glass model [68-74] and a random-field model [76,77], the size of the PNR is still discussed controversially.

Direct observations of the local polarization using piezo-response-force microscopy (PFM) suggest rather extended regions of uniform polarization of up to a few 100 nm in diameter [117], neutron scattering measurements indicate the length scale of the PNRs is several nm [64,113], and transmission electron microscopy (TEM) images show local variations of the structure and thus uniform polarization of a size of 10 to 20 nm [65] or even only a few unit cells [118] that could be associated with the PNRs. The latter is supported by simulation [119]. However, PFM as well as TEM observations are mainly restricted to surface properties, whereas PNRs are expected to exist in the bulk, i.e. 3D polar clusters embedded in a dielectric or ferroelectric matrix. Furthermore, all these techniques refer to static polarization, whereas in electronic (e.g. frequency-dependent) measurements the mobility of the PNRs plays a major role. Therefore, a 'direct' measurement of the size and mobility of the PNRs would be desirable.

In this chapter, we first demonstrate the relaxor-type behavior of our strained NaNbO_3 films via frequency dependent measurement of the permittivity, Vogel-Fulcher analysis of the frequency dispersion, and the discussion of the temperature dependence of the transition using Lorentz fits. Then we directly analyze the size and mobility of PNRs in our NaNbO_3 films using complex electric field (ac and dc) dependences of the permittivity. Via our experiments we are able to directly evaluate the size of the PNRs and demonstrate that PNRs significantly attribute to the irreversible contribution to the permittivity.

5.1. Relaxor-type behavior

Due to the small, temperature dependent mobility of the PNRs, characteristic features should be observed in frequency dependent measurements of the ferroelectric properties in the relaxor regime. Especially at the transition to the relaxor ferroelectric state the permittivity and the maximum in the ϵ' -versus- T characteristic are expected to be frequency dependent.

5.1.1. Vogel-Fulcher behavior

Fig. 5.2 shows the temperature dependence of the permittivity for different frequencies for the 27 nm thick NaNbO_3 film and the electric field direction along short axis ($[001]\text{NdGaO}_3$). Especially at the peak in ϵ' , large differences in the permittivity are recorded for different frequencies. With increasing frequency the permittivity decreases and the temperature of the maximum permittivity T_{\max} increases. Generally, this frequency dependence of the permittivity can serve as a fingerprint for relaxor-type ferroelectrics [68,84]. This is evident from the frequency dependent shift of T_{\max} (temperature of maximum permittivity) according to the Vogel - Fulcher equation [61]:

$$f = f_o \exp \left[- \frac{E_a}{k_B (T_{\max} - T_{VF})} \right] \quad (5.1)$$

with activation energy E_a , Vogel-Fulcher freezing temperature T_{VF} , , attempt frequency f_o , and Boltzmann constant k_B . Performing frequency dependent measurements of $T_{\max}(f)$ in the frequency regime of 100 Hz to 1.5 MHz (see example in Fig. 5.2(a)), it can be demonstrated that the NaNbO_3 film shows typical relaxor-type behavior in agreement with Eq. (5.1). By inserting a reasonable attempt frequency (e.g. $f_o = 2- 8$ GHz) we can extract the activation energy E_a and the freezing temperature T_{VF} from the resulting Vogel-Fulcher fit. The first one describes the energy necessary for the reorientation of the polarization of the PNRs, the latter one characterizes the temperature at which the PNRs start to freeze, i.e. become immobile. Fig. 5.2(b) exemplifies the Vogel-Fulcher analyses based on measurements performed at various frequencies (Fig. 5.2(a)) with different attempt frequency f_o according to a logarithmic transformation of Eq. (5.1)

$$\left[\ln \left(\frac{f}{f_o} \right) \right]^{-1} = - \frac{k_B}{E_a} (T_{\max} - T_{VF}) \quad (5.2)$$

The dash lines represent linear fits according to Eq. (5.2) and are used to evaluate E_a and T_{VF} , which yields $T_{VF} = 79.3$ K and $E_a = 16.57$ meV, $T_{VF} = 77.1$ K and $E_a = 18.73$ meV, and $T_{VF} = 76.9$ K and $E_a = 21.54$ meV for $f_o = 2$ GHz, 4 GHz, and 8 GHz, respectively. T_{VF} and E_a show little dependence of the attempt frequency, especially the freezing temperature. The values obtained for E_a are comparable to values reported for activation energies of a relaxor ferroelectric in the literature [68, 120].

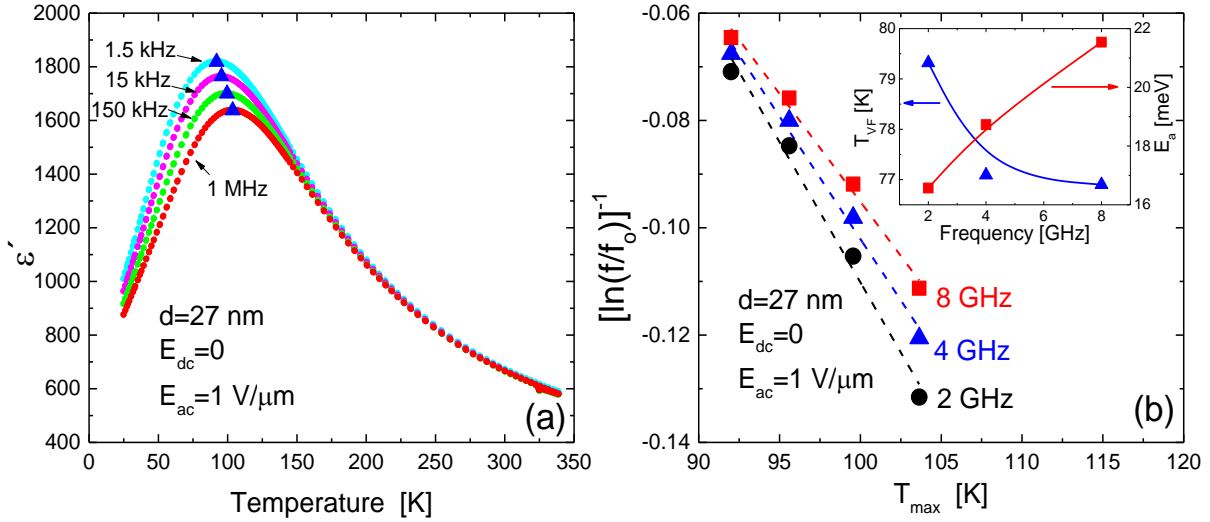


Fig. 5.2: Typical examples for (a) the frequency dependent measurement of the permittivity (the position T_{max} is marked by blue triangles) and (b) the resulting Vogel-Fulcher fits (dash lines) based on Eq. (5.2) with $f_o = 2$ GHz (black), 4 GHz (blue) and 8 GHz (red) for the 27 nm thick NaNbO_3 film with E oriented along the shorter axis of NdGaO_3 . The corresponding T_{VF} and E_a as function of attempt frequency f_o are shown in the inset of Fig. 5.2(b). The electric field values and thickness of the films are given in the figure.

5.1.2. Lorentz fit

In addition, all ϵ' -versus- T plots measured for our NaNbO_3 films show a broad peak rather than a sharp one which would characterize transition for the “classical” ferroelectric material. The transition regimes can be analyzed by a Lorentz simulation [62]:

$$\frac{\epsilon'_{max}}{\epsilon'} - 1 = \frac{(T - T_{max})^\gamma}{2\sigma^2} \quad (5.3)$$

for $T > T_{max}$, with γ representing the degree of the dielectric relaxation and σ denoting the degree of the diffuseness of the phase transition. A sharp transition peak in classical

ferroelectrics is described by $\gamma = 1$, whereas a relaxor-like phase transition is usually characterized by $\gamma \approx 1.5 - 2$.

Using a transformation of Eq. (5.3):

$$\ln\left(\frac{\varepsilon'_{\max} - \varepsilon'}{\varepsilon'}\right) = \gamma \ln(T - T_{\max}) - \ln 2\sigma^2 \quad (5.4)$$

the normalized permittivity should show a linear temperature dependence in a double-logarithmic plot of $\ln((\varepsilon'_{\max} - \varepsilon')/\varepsilon')$ -versus- $\ln(T - T_{\max})$. The slope of this plot provides the value of γ , the intercept gives the value of σ .

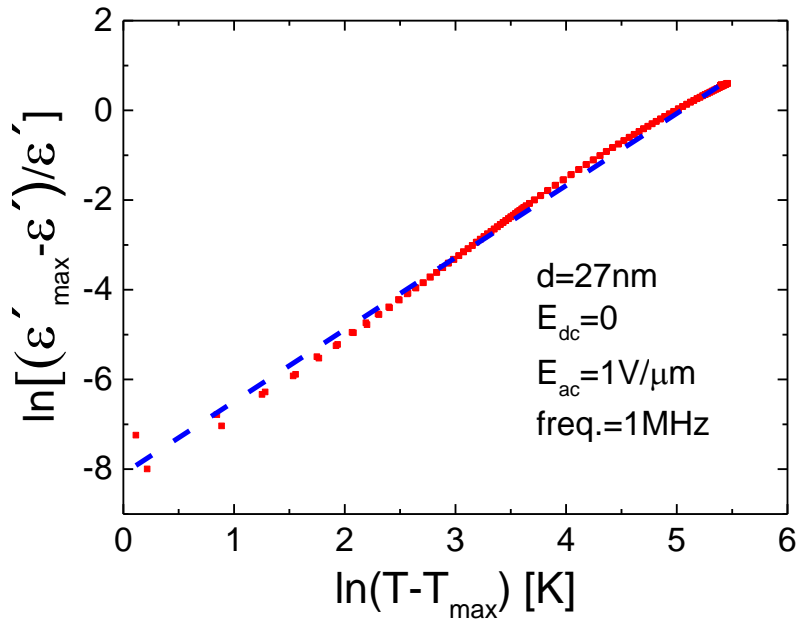


Fig. 5.3: Double logarithmic plot of the reduced and normalized permittivity versus reduced temperature at the phase transition ($T > T_{\max}$) measured at 1 MHz, $E_{dc} = 0$, $E_{ac} = 1 \text{ V}/\mu\text{m}$ for the NaNbO_3 film with a thickness of 27 nm (red). The blue dash line represents the theoretic Lorentz fit based on Eq. (5.4).

For the example shown in Fig. 5.3 we obtain $\gamma \approx 1.6$ with $\sigma = 40.6 \text{ K}$. Similar values of $\gamma \approx 1.6 - 2$ are obtained for the other samples. This supports the assumption that the peak in the temperature dependence of the permittivity results from the transition of the dielectric (or paraelectric) state at high temperature to a relaxor-type ferroelectric state at low

temperature. The transition temperature for this type of ferroelectric transition is typically very broad, therefore it is usually associated with the temperature T_{\max} . From now on we will use T_{\max} as the phase transition temperature for the dielectric to the relaxor-type ferroelectric state. It should be noted again, that we only refer to the in-plane ferroelectric properties of our c-axis oriented NaNbO_3 films.

5.2. Electric field dependence of the permittivity

Not only the frequency dispersion and the temperature dependence of the permittivity at the transition from the dielectric to the ferroelectric state show different behaviors for relaxor-type ferroelectrics compared to classical ferroelectrics. Also the electric field dependence of the permittivity is characteristic (i.e. larger) for relaxor-type ferroelectrics at temperatures around the transition temperature.

Fig. 5.4 summarizes the electric field dependence of the permittivity along the $[001]\text{NdGaO}_3$ direction for the 27 nm and 63 nm thick NaNbO_3 films. In order to visualize the impact of the electric field, it shows the change of the permittivity $\Delta\varepsilon'$ with respect to the data $\varepsilon'(0)$ recorded for smallest electric field ($E_{\text{dc}} = 0$ and $E_{\text{ac}} = 0.048 \text{ V}/\mu\text{m}$) that were already shown in Fig. 4.3. The impact of a dc bias (dc tunability) is given in curves 1 – 5 (see Fig. 5.4(a)), which are measured for dc-voltages of 1 V to 5 V, respectively. In the paraelectric regime (i.e. the temperature regime close to the dielectric-to-relaxor-type ferroelectric transition temperature), a significant dc bias dependent reduction of ε' is observed. The peak position does hardly depend on the applied dc field. The paraelectric regime extends from approximately 25 K to 250 K with a maximum tunability $n = \Delta\varepsilon'/\varepsilon'(0)$ for only 5 V (equivalent to $1 \text{ V}/\mu\text{m}$) of $n \approx 6 \%$ and $n \approx 3.7 \%$ for the 27 nm and 63 nm thick sample, respectively (see Fig. 5.4(c) and (d)). This dc-bias dependence agrees well with that of classical ferroelectrics [121].

In contrast, an increase of the ac electric field leads to a pronounced increase of the permittivity in the paraelectric regime (see curves 6 – 10 in Fig. 5.4(b)). Although the electric field strengths are identical to that of the dc-bias (i.e. a maximum electric field of $1 \text{ V}/\mu\text{m}$ is applied in both cases) the impact of the ac-field is several times (~ 6 times) larger than that of the dc-bias (see Fig. 5.4). Furthermore, the position of the peak in the $\Delta\varepsilon'$ -versus-T plot depends on the ac-field. This ac-electric field dependence is not only extremely large, it is also characteristic for relaxor-type ferroelectrics, since it is caused by the limited polarizability (or

mobility) of the PNRs which are also responsible for the frequency dispersion. This ac field dependence and its consequence will be discussed in detail in the following section.

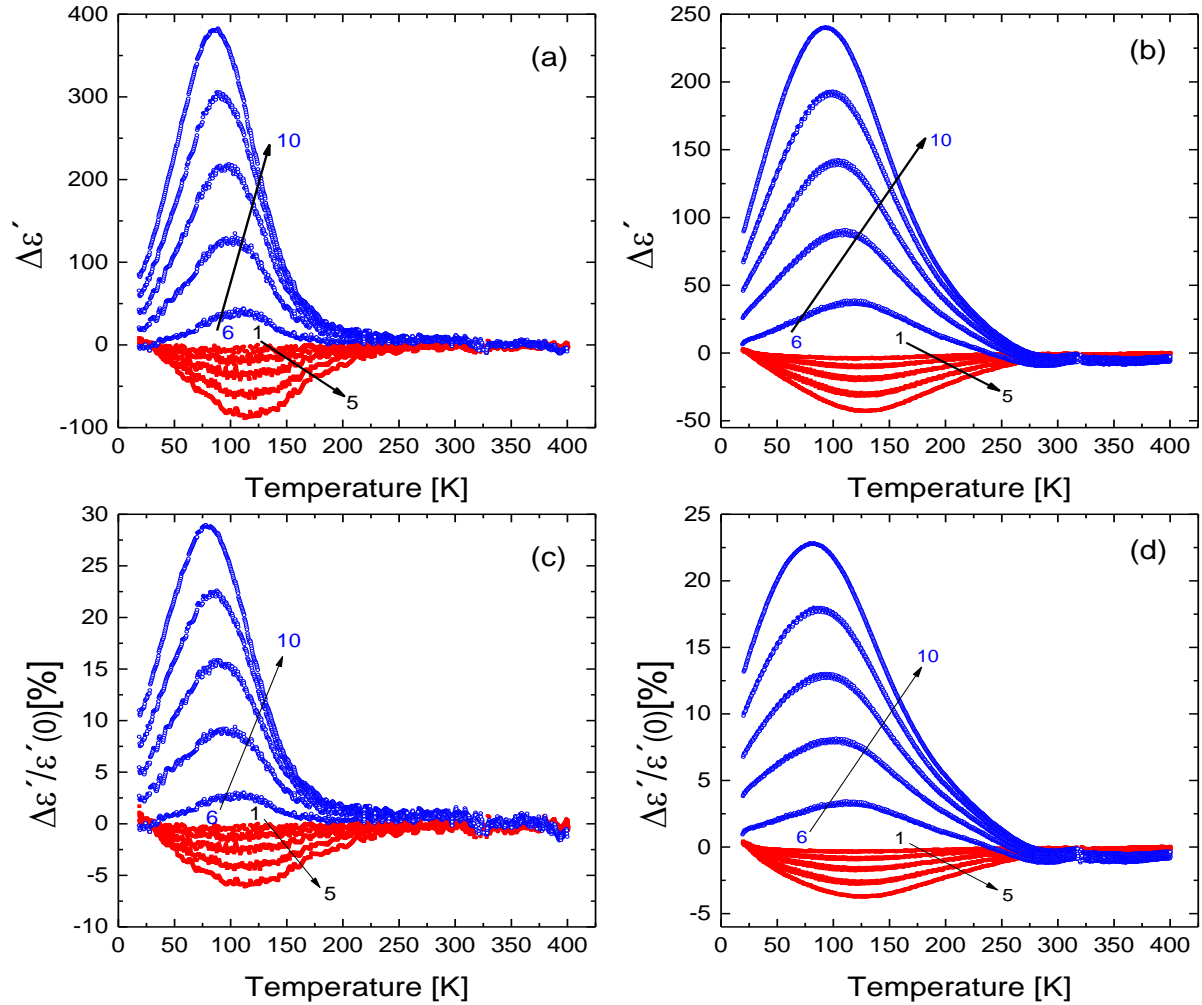


Fig. 5.4: Temperature dependence of the electric field induced modification of the permittivity with respect to the data shown in Fig. 4.3 and resulting tunability for the 27 nm (a, c) and 63 nm (b, d) thick NaNbO_3 films, where $\Delta\epsilon'$ is defined as $\Delta\epsilon' = \epsilon'(E_{ac}, E_{dc}) - \epsilon'(0)$ and $\epsilon'(0) = \epsilon'(E_{ac} = 0.048\text{V}/\mu\text{m}, E_{dc} = 0)$ and tunability is defined as $\Delta\epsilon'/\epsilon'(0)$. For curves 1 – 5 (red solid symbols) the dc-bias is varied from $E_{dc} = 0.2\text{ V}/\mu\text{m}$ to $1\text{ V}/\mu\text{m}$ in steps of $0.2\text{ V}/\mu\text{m}$, the ac-field is kept at the minimum value of $E_{ac} = 0.048\text{ V}/\mu\text{m}$, while for curves 6 – 10 (blue open symbols) the ac-field amplitude is increased in steps of $0.2\text{ V}/\mu\text{m}$ from $E_{ac} = 0.2\text{ V}/\mu\text{m}$ to $1\text{ V}/\mu\text{m}$ with $E_{dc} = 0$. The frequency is 1 MHz for all measurements, the arrows indicate the direction of increasing electric field.

5.3. Polar nanoregions

In this section, we combine the frequency and ac-electric field dependent experiments in order to learn more about the PNRs of the relaxor-type material. We develop a new model that actually provides values for the size of the PNRs.

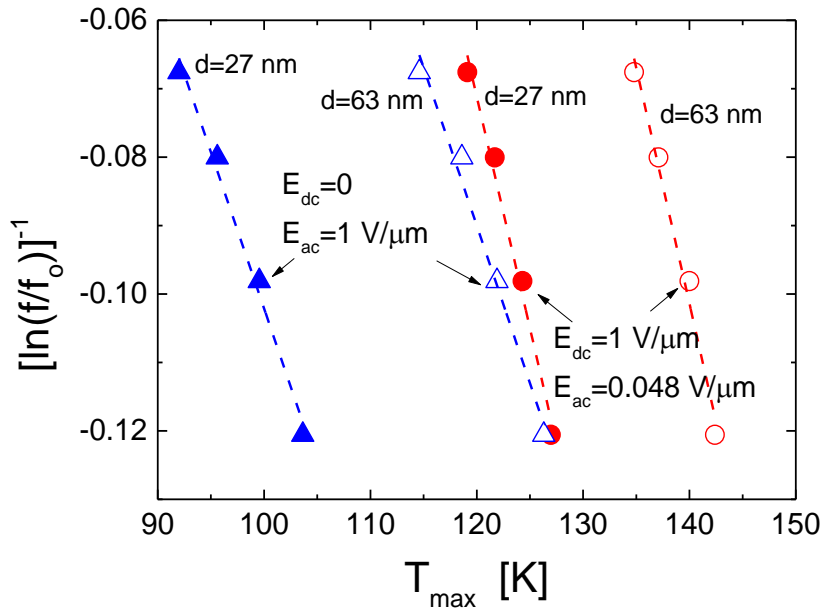


Fig. 5.5: Typical examples for the Vogel-Fulcher fits (dash lines) based on Eq. (5.2) with $f_0 = 4$ GHz for different ac and dc electric field combinations with E oriented along shorter axis for the 27 nm (solid symbols) and 63 nm (open symbols) thick films. The electric field values and thickness of the films are given in the figure.

Generally, the frequency dependence of the permittivity is a characteristic for relaxor-type ferroelectrics. In the previous discussion, we demonstrated that our compressively strained NaNbO_3 represent a relaxor-type ferroelectric as shown in chapter 5.1. A typical Vogel-Fulcher fit has already been shown in Fig. 5.2. Fig. 5.5 exemplifies various Vogel-Fulcher analyses according to Eq. (5.2) based on measurements performed at various frequencies similar to data shown in Fig. 5.2 and different ac and dc electric field combinations with E oriented along $[001]\text{NdGaO}_3$ (short axis) for two NaNbO_3 thin films. The dash lines represent linear Vogel-Fulcher fits according to Eq. (5.2) which are used to evaluate E_a and T_{VF} .

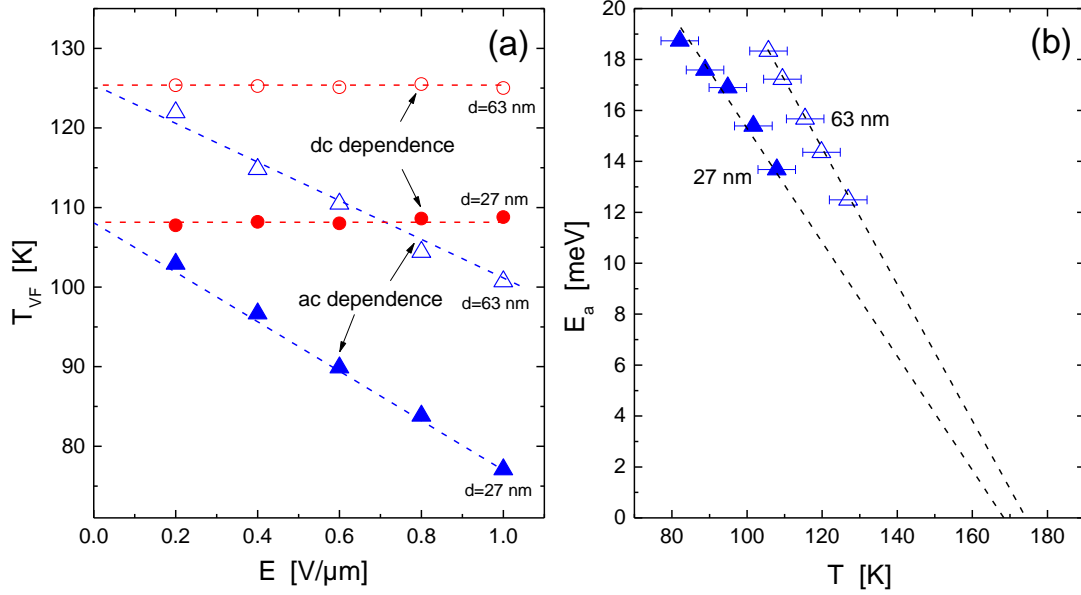


Fig. 5.6: (a) Freezing temperature as function of dc (red circles) and ac (blue triangles) electric field and (b) temperature dependence of the activation energy for NaNbO_3 thin films with a thickness of 27 nm (solid symbols) and 63 nm (open symbols) and E oriented along the short axis. Both parameters T_{VF} and E_a are obtained from the Vogel-Fulcher fit (Eq. (5.2)) as shown in Fig. 5.5, and using an attempt frequency of 4 GHz. In case of the ac dependence, dc was zero. For the dc dependence, a small ac field of $0.048 V/\mu m$ is applied.

The resulting electric field dependence of the freezing temperature T_{VF} (Fig. 5.6(a)) and temperature dependences of the activation energy (Fig. 5.6(b)) reveal a number of important information on the PNRs:

- (i) T_{VF} does hardly depend on the dc bias. For classical relaxor ferroelectrics different field dependences have been reported. For instance a small decrease of T_{VF} of about 4 K is reported for (Mg,Nb) - doped lead titanate, whereas a small decrease of ~ 3 K followed by a significant increase of T_{VF} is reported for lead magnesium niobate for the dc field regime of 0 to $1 V/\mu m$ [122,123]. However, generally, the dc field dependence of the freezing temperature is expected to be small. Therefore, it can be assumed that the size of the PNRs that contributes to the permittivity is only little affected by the dc field at this regime for our system.
- (ii) However, a significant decrease of T_{VF} is observed for increasing ac amplitudes. The freezing temperature decreases by 21 K and 26 K for the 63 nm and 27 nm thick films, respectively, if the ac-field amplitude is changed from $0.2 V/\mu m$ to $1 V/\mu m$. We will use

this field dependence of T_{VF} below to estimate the size of the PNRs that is ‘active’ (i.e. still mobile) at the freezing temperature.

(iii) The magnitude of the activation energy agrees with the expected values for relaxor ferroelectrics [68,120]. Moreover, E_a decreases with temperature (Fig. 5.6(b)) in a linear way to zero at about 170 K. Below (see discussion of Fig. 5.10) we will show that at this temperature the irreversible contribution to the permittivity actually vanishes.

Let us first discuss the ac-field dependence of the freezing temperature shown in Fig. 5.6(a). This dependence actually allows us to estimate the size of the ‘active’ PNRs that contributes to permittivity at the freezing temperature. Comparing the change of the total energy per volume

$$U_e = \frac{\epsilon'_0 \epsilon' (\Delta E_{ac})^2}{2} \quad (5.4)$$

stored by an ac electric field E_{ac} in a dielectric material with the change of the thermal energy of a PNR with a volume V_{PNR} we obtain:

$$V_{PNR}(T_{VF}) = \frac{2 \cdot k \cdot \Delta T_{VF}}{\epsilon'_0 \cdot \epsilon'(T_{VF}) \cdot (\Delta E_{ac})^2} \quad (5.5)$$

Inserting experimental values for ΔT_{VF} and ΔE_{ac} from Fig. 5.6 and an estimation for the permittivity of the PNRs by using $\epsilon'(T_{VF})$ from Fig. 4.3, we obtain very similar values for the volume of the PNRs for both samples, i.e. from approximately 70 to 270 nm³, which however depend on the applied ac field amplitude (see Fig. 5.7). Desheng Fu et al. [65] reported that the PNR starts to transform its shape from spherical at $T > T_{VF}$ into elliptical at T_{VF} for decreasing temperature. In order to estimate the diameter of the PNR, we assume that these PNRs are still spherical at T_{VF} in our samples. In this case, the resulting diameter of the PNRs would decrease with increasing ac field from ~ 8 nm at 0.2 V/ μ m to ~ 5.2 nm at 1 V/ μ m for both samples (see Fig. 5.8). The value is smaller than that reported for PFM experiments [117], however very similar to that measured by neutron scattering [64,113] and TEM [65]. However, it should be noted that in contrast to the microscopic data, our electronic analysis characterizes the size of the electronically ‘active’ PNRs inside the ferroelectric matrix at the freezing temperature. Furthermore, the microscopic observations refer to classical relaxor ferroelectrics, whereas our measurements are performed on strain-induced oxide thin film relaxors.

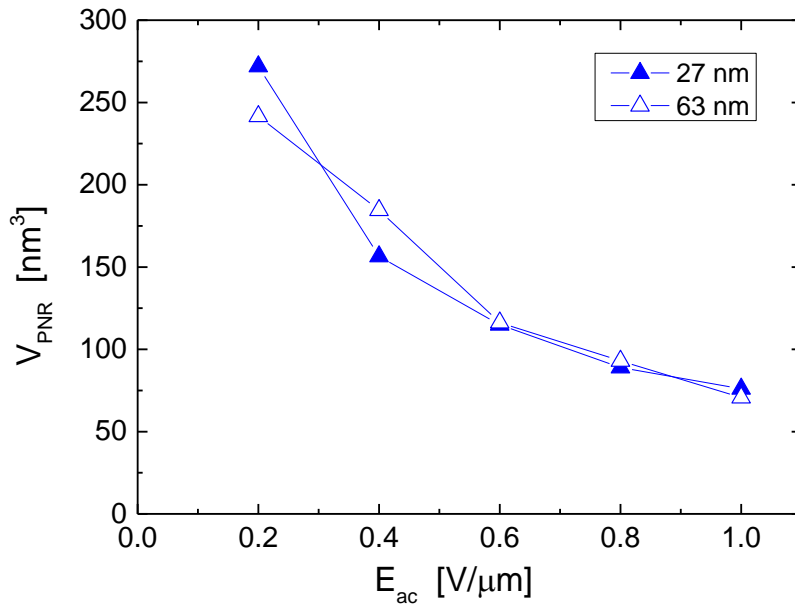


Fig. 5.7: Volume of PNRs that are mobile (i.e. attributing to the permittivity) at the freezing temperature as function of applied ac electric field for 27 nm (solid) and 63 nm (open) thick NaNbO_3 films, respectively. The volume is obtained via Eq. 5.5 using the data for $\Delta T_{\text{VF}}(E_{\text{ac}})$ and $\epsilon'(T_{\text{VF}})$ given in Fig. 5.6 and 4.3, respectively.

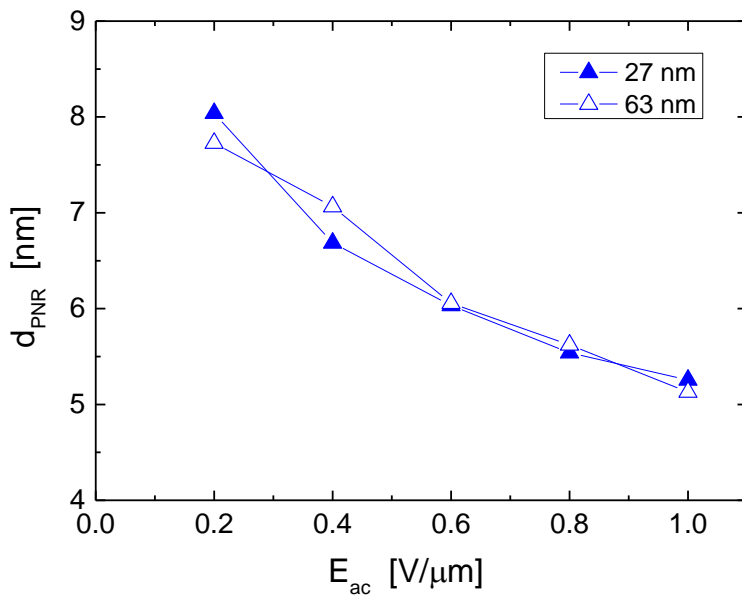


Fig. 5.8: Diameter of PNRs that are mobile (i.e. attributing to the permittivity) at the freezing temperature as function of applied ac electric field for 27 nm (solid) and 63 nm (open) thick NaNbO_3 films, respectively. The diameter of PNRs are calculated by assuming an idealized spherical shape for the PNRs.

The ac electric field dependence of the PNR's size in Fig. 5.7 and 5.8 are very striking. They could be a result of the assumptions and simplifications that were used. For instance,

- (i) for the permittivity of the PNRs the permittivity of the sample itself (reversible and irreversible contribution) is used,
- (ii) the impact of 'pinning' on the PNRs (e.g. their polarization) is neglected, and
- (iii) all values represent averaged values for the size and form of the PNRs, a distribution of the PNR's size is not unlikely [124].

Nevertheless, the ac-field dependent size of the PNRs is reasonable, since a larger driving force will lead to enhanced repolarization of the PNRs that could cause a reduction of the effective size of the polar clusters.

5.4. Reversible and irreversible behavior

Finally, the contribution of the PNR to the permittivity is discussed. Fig. 5.9 shows a set of ac-field dependent measurements of the permittivity at 1 MHz. Similar measurements are performed for other frequencies. All samples exhibit a linear dependence of ϵ' -versus- E_{ac} for all temperatures and frequencies, which is a characteristic feature of hard ferroelectrics and can be described by the Rayleigh law [125]:

$$\epsilon' = \epsilon'_{init} + \alpha E_{ac} \quad (5.6)$$

where ϵ'_{init} represents the initial (reversible) permittivity at zero electric field and α the Rayleigh coefficient that describes the irreversible properties of the polarization. In classical ferroelectrics ϵ'_{init} represents contribution to the permittivity arising from the intrinsic lattice polarization and the reversible domain wall motions, whereas α is caused by pinning of ferroelectric domain wall at defects [126]. In relaxor-type ferroelectrics also the PNRs can attribute to the irreversible properties, and thus to the Rayleigh coefficient α [119,127]. From the previous section we have known that the mobility of PNRs not only depends on the temperature but also on the applied electric field.

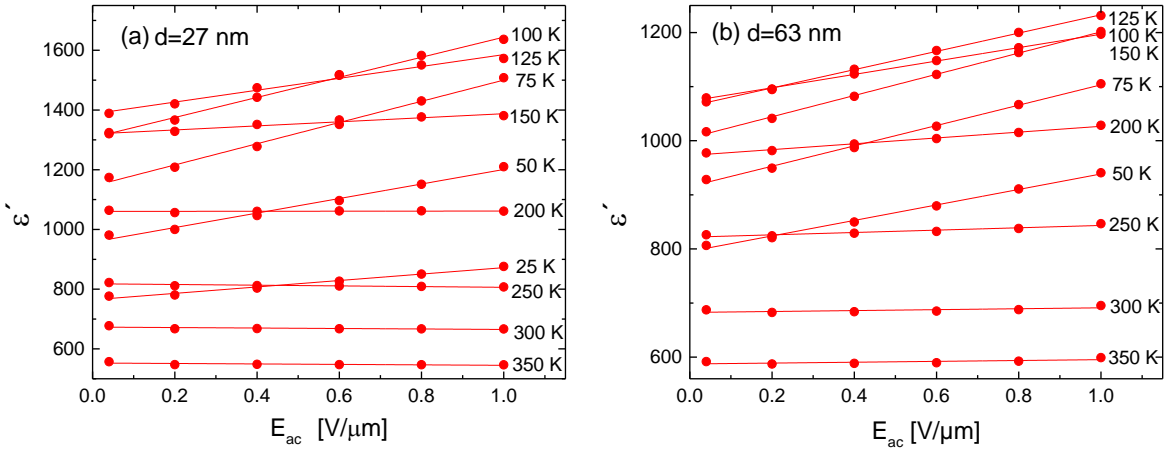


Fig. 5.9: Permittivity as function of the ac electric field measured at 1 MHz and different temperatures for E oriented along the short axis for the 27 nm (a) and 63 nm (b) thick NaNbO_3 films, respectively. The lines represent linear fits of the data according to Eq. (5.6).

For all temperatures and frequencies the permittivity data in Fig. 5.9 show a linear behavior and can be fitted by Eq. (5.6). The resulting values for ϵ'_{init} and α are shown in Fig. 5.10.

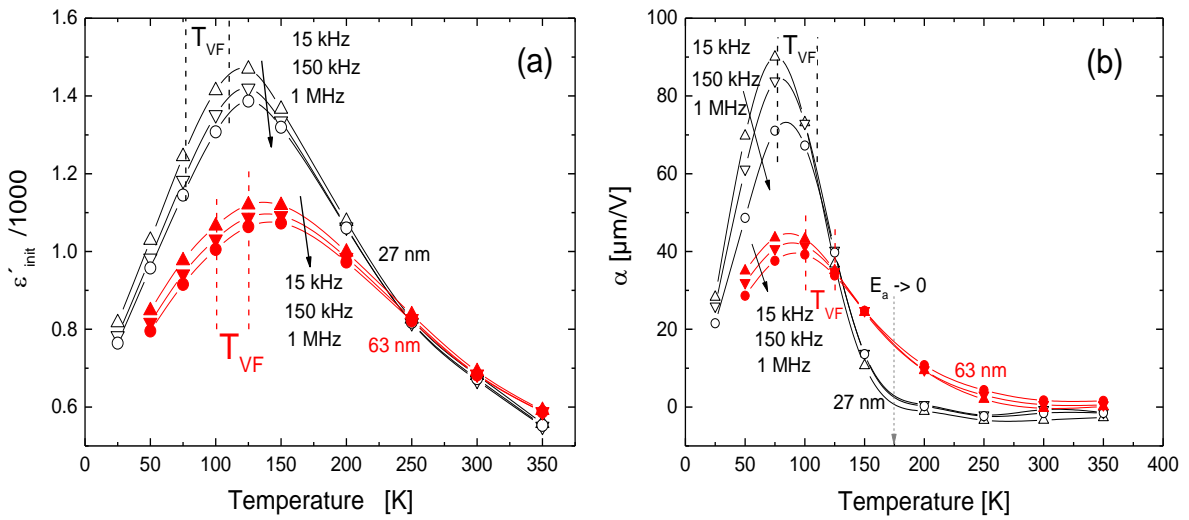


Fig. 5.10: Initial permittivity (a) and Rayleigh parameter (b) as function of temperature for the NaNbO_3 thin films with different thickness, 27 nm (open symbols) and 63 nm (solid symbols), measured at frequencies 15 kHz (triangle), 150 kHz (inverted triangle), and 1 MHz (circle). The dashed lines mark the regime of freezing temperature for $E_{\text{ac}} = 1 \text{ V}/\mu\text{m}$ (lower temperature) and $E_{\text{ac}} = 0.048 \text{ V}/\mu\text{m}$ (higher temperature). The solid arrows indicate the direction of increasing frequency, the dashed arrow in (b) marks the temperature at which the activation energy extrapolates to zero (see Fig. 5.6(b)).

The observations show a number of interesting features:

- (i) Obviously, the initial (reversible) permittivity ϵ'_{init} represents the permittivity expected for zero electric field. The values are slightly smaller than the experimental data obtained for finite electric fields, the temperature dependence is very similar to the one obtained for small ac fields (see Fig. 4.3).

- (ii) The Rayleigh coefficient α displays a revealing temperature dependence, it characterizes the irreversible contribution of domain walls and especially PNRs. It shows a pronounced peak at low temperature, i.e. close to the freezing temperature T_{VF} , and tends to zero at high temperature. This behavior is dominated by the presence and mobility of the PNRs [119,127]. At high temperatures, no PNRs are present. Therefore, the permittivity is constant, i.e. $\alpha \approx 0$. With the transition to the relaxor state, PNRs start to form. The existence and the pinning of the PNRs lead to a field-dependent permittivity, i.e. $\alpha > 0$. With decreasing temperature the size of the PNRs increases [113,128] and as a consequence α increases. However, at the freezing temperature, the PNRs start to become immobile, therefore α decreases below the freezing temperature. Especially for the thinnest sample ($d = 27$ nm) with the largest strain this behavior is very pronounced (see Fig. 5.10, black curves). Above $T \approx 170$ K the Rayleigh coefficient is $\alpha \approx 0$ (i.e. no PNRs are present), only below $T \approx 170$ K values $\alpha > 0$ are observed (PNRs are present). It should be noted, that this temperature actually nicely agrees with the expected vanishing of the activation energy E_a for PNRs obtained by the linear extrapolation in Fig. 5.6(b). Finally, a pronounced peak at low temperature shows a maximum slightly below T_{VF} . The thicker sample (63nm) shows a similar behavior. However, due to a larger impact of domain wall pinning that has to be expected for thicker samples the onset of the peak at high temperature is not that sharp as observed for the thinner sample.

- (iii) The irreversible contribution to the permittivity is even better visible by considering the ratio $\alpha/\epsilon'_{\text{init}}$ (see Fig. 5.11) which describes the extrinsic contribution of the PNRs to the permittivity. It shows a temperature dependence comparable to that of α , the peak at low temperature is even more pronounced and the maximum is slightly shifted to lower temperature. The maximum values of $(\alpha/\epsilon'_{\text{init}})_{\text{max}} = 7.4 \times 10^{-8}$ m/V for strained NaNbO_3 films is quite comparable to values reported in literature [12,126,127,129-132] (see inset of Fig. 5.11).

(iv) Another important information is given by the frequency dispersion of the data obtained for α , ϵ'_{init} and $\alpha/\epsilon'_{\text{init}}$ in the peak regime (see measurements for different frequencies in Fig. 5.10 and 5.11). The peak position of $\alpha(T)$, ϵ'_{init} and $\alpha/\epsilon'_{\text{init}}$ is shifted to lower temperatures with decreasing frequency. Similar to the frequency dispersion of the permittivity, it clearly indicates, that the peak in α , ϵ'_{init} , and $\alpha/\epsilon'_{\text{init}}$ show a relaxor behavior. Therefore, the reversible and also the irreversible permittivity seem to be strongly affected by the properties of the PNRs in these relaxor-type ferroelectrics.

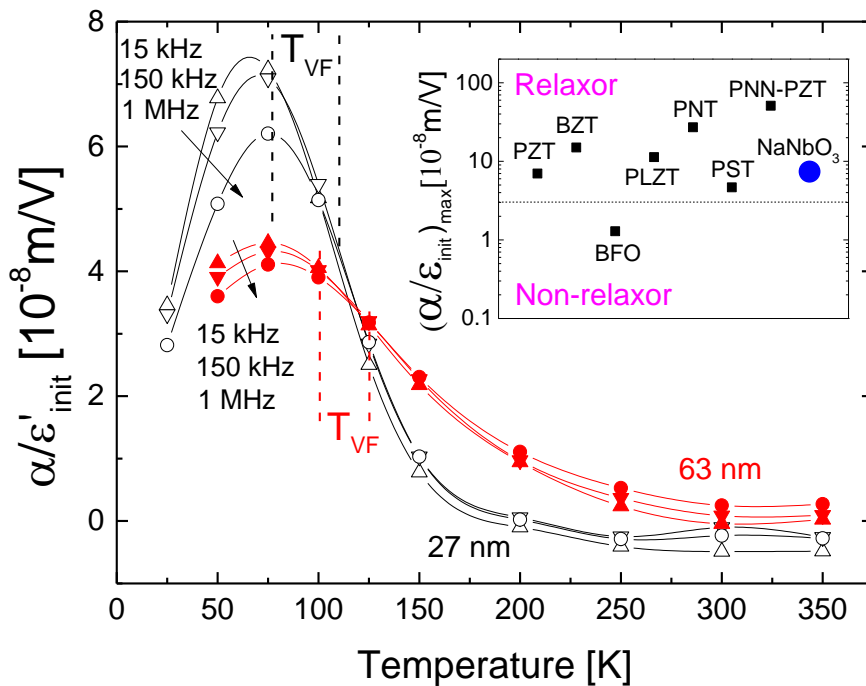


Fig. 5.11: Normalized Rayleigh parameter as function of temperature for the NaNbO_3 films with different thickness, 27 nm (open symbols) and 63 nm (solid symbols), measured at frequencies 15 kHz (triangle), 150 kHz (inverted triangle), and 1 MHz (circle). The inset shows a comparison of the maximum normalized Rayleigh parameters of strained NaNbO_3 films with literature values [12,126,127,129-132]. Except for BFO all systems are known or most likely relaxor-type ferroelectrics.

5.5. Summary

In summary of this chapter:

- (i) We demonstrated that our compressively strained NaNbO_3 films exhibit a typical relaxor-type behaviors, e.g. a broad and frequency-dispersive peak in the ϵ' -versus- T curves that are interpreted via Vogel-Fulcher and Lorentz-type analyses, respectively. The temperature T_{max} is defined as the characteristic temperature of this transition.
- (ii) This relaxor-type behavior leads to a strong electric field dependence of the permittivity. The dc tunability in the paraelectric regime is comparable to that of the tunable classical ferroelectric materials, whereas a large enhancement of the permittivity is observed if the ac-field is enhanced.
- (iii) By combining frequency dispersive and electric field (ac and dc) dependent measurements, we succeed to estimate of the size of the 'active' PNRs at the freezing temperature. According to our model, the volume of PNR depends on the applied ac field and varies from 70 to 270 nm^3 in the temperature regime of 80 – 150 K. The resulting diameter of the PNR (assuming idealized spherical PNRs) at the freezing temperature ranges from ~5.2 nm to ~8 nm for large and small fields, respectively. These values are in agreement with literature values reported for neutron scattering experiments [64,113] and TEM measurement [65] for classical relaxor ferroelectrics. The field dependence might be explained by the size reduction caused by increasing repolarization forces. Second, the activation energy E_a of the PNRs is of the order of 15 – 20 meV at 100 K. It decreases linearly with temperature to zero at 170 – 180 K, the temperature at which the irreversible contribution to the permittivity vanishes.
- (iv) All samples show a linear ac dependence of the permittivity at all temperatures and frequencies, which is in accordance with the Rayleigh law. The temperature dependence of the intrinsic (reversible) polarization ϵ'_{init} is similar to that measured at small ac fields. However, the irreversible Rayleigh coefficient α is zero at high temperature (no PNRs), and shows a pronounced peak with a maximum slightly below T_{VF} . The position, broadness, and frequency dispersion of this peak demonstrate that PNRs play a dominant role for the irreversible contribution to the permittivity.

6. Stoichiometry dependence and Na_3NbO_4 nanoprecipitates

In the previous chapter, we demonstrate, that strain can induce a phase transition from the dielectric to the ferroelectric state in NaNbO_3 at low temperature. However, the ferroelectric state turns out to be a relaxor-type ferroelectric state. The latter is most likely caused by inhomogeneities due to a slight off-stoichiometry of the NaNbO_3 film. One way to obtain a classical (i.e. non-relaxor-type) ferroelectric NaNbO_3 might be to improve the stoichiometry. This has, for instance, been demonstrated for tensily strained SrTiO_3 on DyScO_3 [13].

We actually decided to do the opposite and increase the deviation from the ideal 113-stoichiometry of NaNbO_3 . In this chapter we will demonstrate that this can be an ideal way to

- (i) retain the classical ferroelectric behavior of NaNbO_3 however with reduced transition temperature and
- (ii) obtain a fully strained NaNbO_3 film with little or no relaxation of the strain.

For this purpose, NaNbO_3 with additional Na are epitaxially grown on (110) NdGaO_3 substrates via PLD. The structural and ferroelectric properties of these $\text{Na}_{1+x}\text{NbO}_{3+\delta}$ films are investigated. We demonstrate that additionally to NaNbO_3 a second phase, Na_3NbO_4 , develops in the films if the Na-content is large enough. These Na_3NbO_4 seems to form nanoprecipitates that can lead to a larger and homogeneous in-plane compressive strain. The samples show the “classical” ferroelectric behavior with the characteristic thermal hysteresis of the permittivity and structural properties upon thermal cycling, however at much lower temperature than their unstrained counterpart.

6.1. Structural properties of strained $\text{Na}_{1+x}\text{NbO}_{3+\delta}$ films

The structural properties of the $\text{Na}_{1+x}\text{NbO}_{3+\delta}$ films and target are analyzed via x-ray diffraction (XRD). XRD powder measurements of the self-made $\text{Na}_{1+x}\text{NbO}_{3+\delta}$ targets with x ranging from 0 to 0.37 are presented in Fig. 6.1. For the targets, which are prepared with Na excess ($x > 0$) compared to the stoichiometric NaNbO_3 targets ($x = 0$), we observe the occurrence of an extra phase (labeled as “B”) additionally to the main perovskite NaNbO_3 phase (marked by “A” in Fig. 6.1). From a detailed analysis of the powder XRD data we identify phase “B” to be Na_3NbO_4 . The appearance of the Na_3NbO_4 phase for Na rich conditions is in agreement with the $\text{Na}_2\text{O-Nb}_2\text{O}_5$ phase diagram [133]. Although the intensities of the peaks of the extra phases increase with increasing amount of Na excess, they are small compared to the reflected intensity of the NaNbO_3 phase. This indicates that NaNbO_3 still represents the main phase in the off-stoichiometric targets.

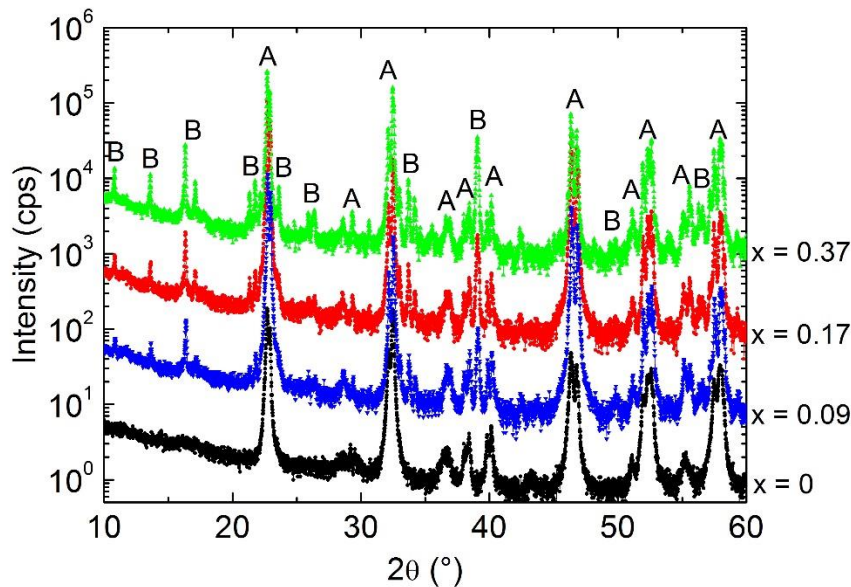


Fig. 6.1: Powder XRD measurements of $\text{Na}_{1+x}\text{NbO}_{3+\delta}$ targets prepared with Na excess compared to the stoichiometric NaNbO_3 ($x = 0$) composition. For better visibility the signals are shifted by a factor of 10 for each successive composition, the compositions x are given in the figure. Reflection peaks indicated by “A” and “B” are attributed to the NaNbO_3 perovskite and Na_3NbO_4 as the secondary phase, respectively. Adapted from [100].

Generally, stoichiometric NaNbO_3 films grow c-axis oriented on (110) NdGaO_3 substrate. This is also the case for the off-stoichiometric films. Reciprocal space maps (RSM) in the vicinity of

the asymmetric $(444)_o$ and $(260)_o$ Bragg reflections of the orthorhombic NdGaO_3 substrate demonstrate this (see Fig. 6.2(a) and (b)). The RSM patterns prove the epitaxial growth of the films on the NdGaO_3 substrate, since the in-plane components of the scattering vectors of the NdGaO_3 substrate and of the main intensity of the corresponding Bragg reflections of the NaNbO_3 film coincide.

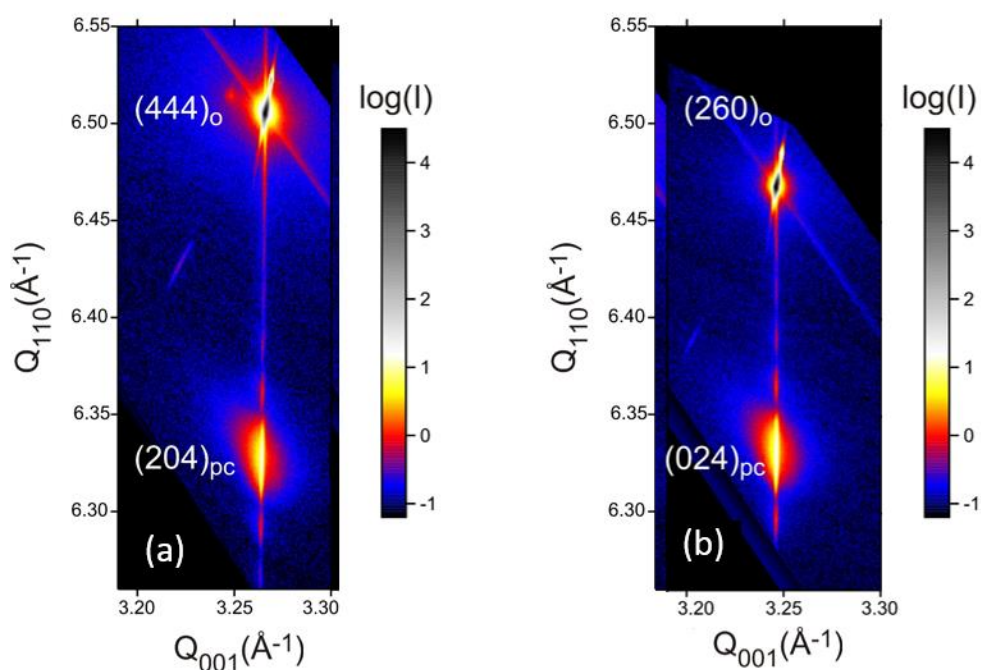


Fig. 6.2: RSM in the vicinity of the $(444)_o$ (a) and $(260)_o$ (b) Bragg reflections of the NdGaO_3 substrate demonstrate the epitaxial growth of the NaNbO_3 phase for the nominally $\text{Na}_{1.17}\text{NbO}_{3+\delta}$ film on NdGaO_3 .

High resolution XRD scans (see Fig. 6.3) recorded between $2\theta = 21^\circ$ and 24° exhibit only Bragg reflection peaks of the $(110)_o$ oriented NdGaO_3 substrate and of the $(001)_{pc}$ oriented NaNbO_3 film for all samples including those with excess Na. No foreign phase could be detected in these measurements. The reason might be simply that the additional phase forms small clusters (i.e. nanoprecipitates), which are too small for the detection via XRD. This assumption is supported by STEM images that provide a more detailed insight into the microstructure of the film and demonstrate the presence of a secondary phase, most likely Na_3NbO_4 .

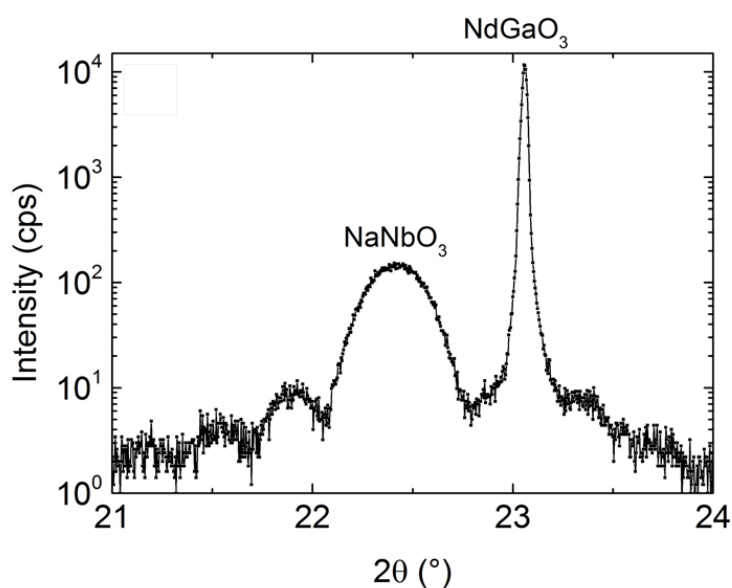


Fig. 6.3: Magnified HRXRD scans around the $(110)_o$ reflection peaks of the NdGaO_3 substrate for the nominal $\text{Na}_{1.17}\text{NbO}_{3+\delta}$ film. Contribution of the NaNbO_3 is clearly visible as well as the substrate NdGaO_3 .

Fig. 6.4(a) shows STEM picture of a film grown from an off-stoichiometric target. For its interpretation, it has to be considered that, due to their small atomic numbers, neither Na nor O can be detected in STEM, only Nb ions are visible. It is obvious from Fig. 6.4(a) that areas with different structures and compositions exist in the film. This is illustrated by the orange and blue open circles in Fig. 6.4(a). In the right part of the STEM image, the distances between Nb ions both in $[001]_o$ and in direction along the surface normal $(110)_o$ are $\sim 4 \text{ \AA}$, which corresponds to the unit cell spacing in a NaNbO_3 perovskite lattice. However, in the left part of the image another regular spot pattern appears between the two Nb ions, which has a significantly lower intensity. This indicates that in $[001]_o$ direction every second Nb ion seems to be located on an O site. These lower intensity spots are not observed in the direction normal to the surface. In STEM the electron beam passes through the whole sample slide, which means that the intensity is summarized over the whole column in $[1\bar{1}0]_o$ direction. Consequently, in order to observe the low intensity spots, Nb ions do not necessarily have to be situated on an O site. Rather they are situated in a column, which would be a pure oxygen column in the perovskite structure. With regard to the above described observation that Na_3NbO_4 has been incorporated as a foreign phase in the target, we believe that these areas marked by the subsequent orange and blue circles in Fig. 6.4(a) represent areas of Na_3NbO_4 . In contrast to the perovskite structure of NaNbO_3 , where the NbO_6 octahedra are corner

connected, Na_3NbO_4 exhibits edge-sharing NbO_6 octahedra. The difference of the two structures is illustrated in Fig. 6.4(b) and (c). It is obvious from the sketch that the correlation of the projection of the distance between two Nb containing columns d_{NaNbO_3} and $d_{\text{Na}_3\text{NbO}_4}$ for NaNbO_3 and Na_3NbO_4 , respectively, in the STEM image is given by $d_{\text{NaNbO}_3} = 2 \times d_{\text{Na}_3\text{NbO}_4}$. This agrees with the experimental observation in Fig. 6.4(a). At this point we conclude that at least our samples with larger off-stoichiometry ($x \geq 0.17$) consist of a NaNbO_3 matrix with embedded Na_3NbO_4 precipitates, i.e. a two phase system $(\text{NaNbO}_3)_{(1-y)}(\text{Na}_3\text{NbO}_4)_y$.

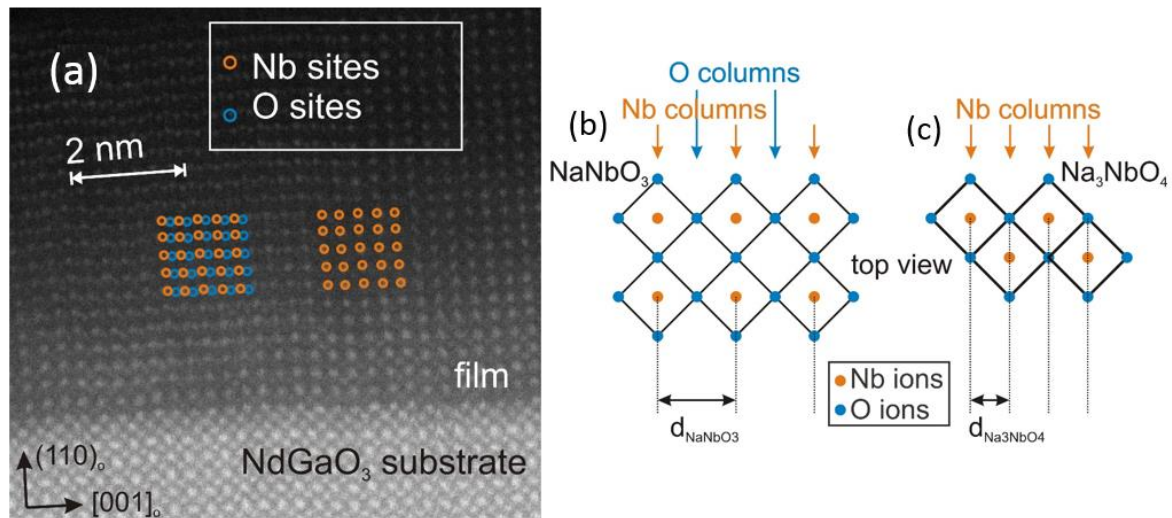


Fig. 6.4: (a)STEM image of a nominal $\text{Na}_{1+x}\text{NbO}_{3+\delta}$ film ($x = 0.17$) on NdGaO_3 demonstrates that in some regions of the film Nb ions seem to occupy O sites, which is an indication for the formation of extended precipitates of Na_3NbO_4 . (b) and (c) sketches of the corner shared and edge shared arrangements of NbO_6 octahedra in the NaNbO_3 perovskite phase and the Na_3NbO_4 phase, respectively. Note, that in (a) the open circles mark Nb ions which are located on Nb sites (orange) and seemingly on O sites (blue) of the perovskite structure, while in (b) and (c) the orange and blue circles actually label the position of the Nb and O ions, respectively, in the NaNbO_3 and Na_3NbO_4 structure.

Another interesting indication for the presence and impact of the secondary phase Na_3NbO_4 is given by high resolution Bragg-Brentano diffraction curves measured in the vicinity of the Bragg reflection peaks of the NdGaO_3 substrate (Fig. 6.5). The $\text{Na}_{1+x}\text{NbO}_{3+\delta}$ films show pronounced thickness oscillations proving smooth surface and interface. From the angular position of the Bragg peak of the reference film (stoichiometric) at about $2\theta = 46.245^\circ$, a vertical lattice spacing of the epitaxial NaNbO_3 phase of $d_{\perp} = 3.923 \text{ \AA}$ can be deduced for room temperature. Heating and cooling of the sample leads to a reversible, linear, and small increase of the lattice parameter with increasing temperature which agrees relatively good

with the temperature dependence of unstrained material, however with slightly larger values for the c-axis (see Fig. 6.5(b)).

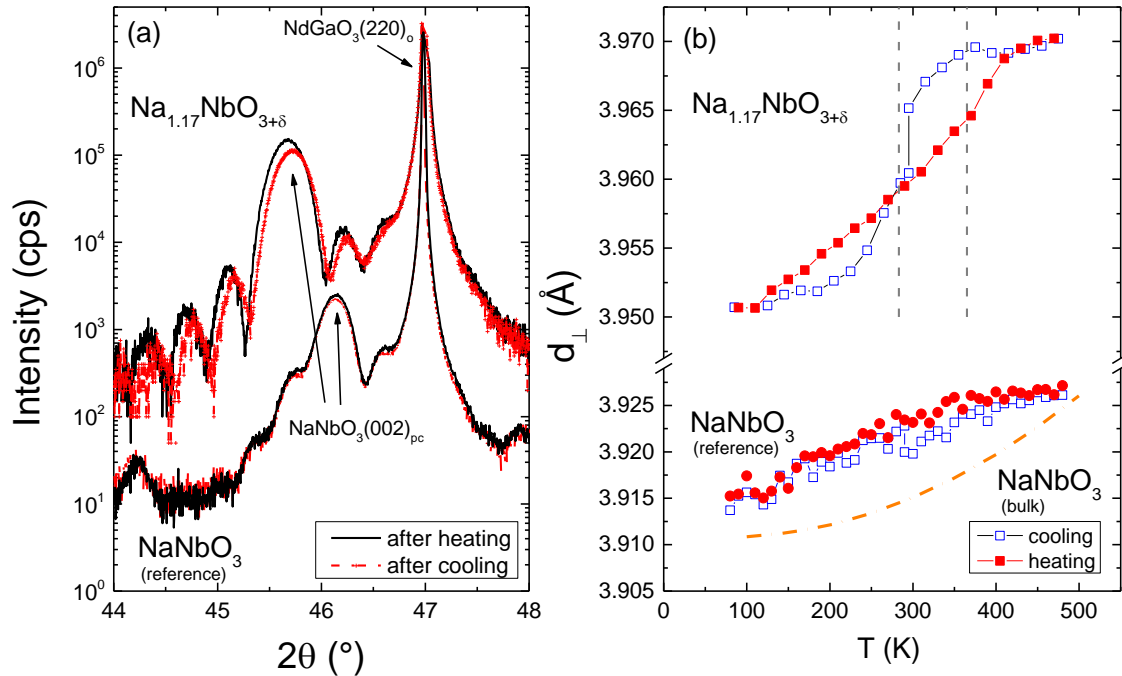


Fig. 6.5: (a) Magnified HRXRD scans of the stoichiometric reference sample NaNbO_3 (lower curves) and sample $\text{Na}_{1.17}\text{NbO}_{3+\delta}$ (upper curves, the intensity is shifted by a factor of 100) recorded at room temperature around the $(220)_o$ reflection peak of the NdGaO_3 substrate after heating to 400K (black curve) and after cooling to 80 K (red curve). (b) Temperature dependence of the vertical lattice parameter of the NaNbO_3 phase for the stoichiometric reference sample (NaNbO_3) and for the $\text{Na}_{1.17}\text{NbO}_{3+\delta}$ film for cooling (open blue symbols) and heating (solid red symbols). The dashed-dotted line (orange) represents the simulating lattice parameter along out-of-plane for unstrained NaNbO_3 [134]. The dashed lines mark the temperature of the hysteretic ferroelectric phase transition, which is discussed below (see for instance Figs. 6.6 and 6.8). Note, that in case of the dielectric measurements the temperature is directly measured at the sample, while for the XRD experiments the temperature of the sample holder is recorded, which may lead to a small difference in the recorded temperature and the actual sample temperature.

However, the nominally off-stoichiometric sample $\text{Na}_{1.17}\text{NbO}_{3+\delta}$ behaves differently. It shows:

- (i) a larger lattice spacing d_{\perp} which is attributed to less strain relaxation in the film, i.e. a “homogeneous” in-plane compressive strain,
- (ii) a stronger temperature dependence of d_{\perp} compared to that of the reference sample, and

(iii) a hysteretic change of the lattice parameter upon thermal cycling (Fig. 6.5(b)).

Especially the last observation points to a hysteretic structural transition of the off-stoichiometric sample.

6.2. Electric properties of strained $\text{Na}_{1.17}\text{NbO}_{3+\delta}$ film

In the following, we will discuss the electronic properties of the samples. We will concentrate on the behavior of the nominal $(\text{NaNbO}_3)_{0.915}(\text{Na}_3\text{NbO}_4)_{0.085}$ film (i.e. $\text{Na}_{1.17}\text{NbO}_{3+\delta}$, $x = 17\%$), which shows an extremely interesting phenomenon similar to that of polycrystalline NaNbO_3 but distinguishable to only slightly off-stoichiometric or stoichiometric samples.

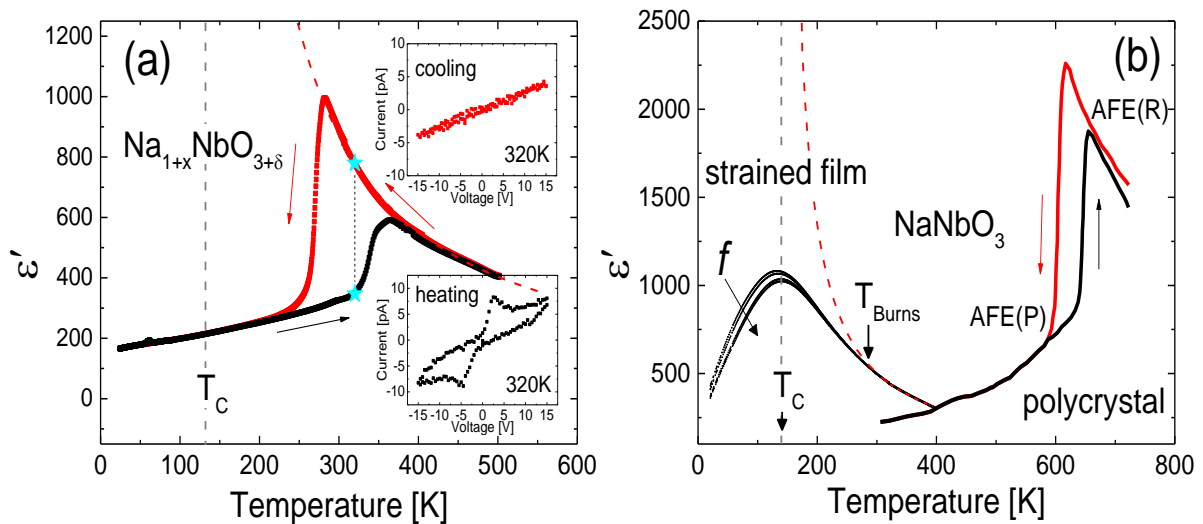


Fig. 6.6: (a) Temperature dependence of the nominal $(\text{NaNbO}_3)_{0.915}(\text{Na}_3\text{NbO}_4)_{0.085}$ film ($\text{Na}_{1.17}\text{NbO}_{3+\delta}$, $x = 17\%$) measured at 100 kHz and an electric field $E_{ac} = 0.2 \text{ V}/\mu\text{m}$. The thermal cycling shows an anomalous hysteretic behavior, which is defined by a transition from the dielectric to the ferroelectric state that occurs at different temperatures for cooling and heating. The arrows indicate the direction of the temperature change, the dashed line shows the Curie-Weiss fit with a Curie-Weiss temperature $T_{cW} \approx 132 \text{ K}$. The insets show the current-voltage characteristics recorded at 320 K for cooling (red) and heating (black) demonstrate the dielectric and ferroelectric state of the off-stoichiometric sample $\text{Na}_{1.17}\text{NbO}_{3+\delta}$, respectively. For comparison, the frequency dispersion of a strained stoichiometric NaNbO_3 film (27nm thick) measured at 15 kHz, 150 kHz, 1 MHz, and 1.5 MHz, is shown in (b). Here, the dashed line represents a Curie-Weiss fit with a Burns temperature $T_{\text{Burns}} \approx 286 \text{ K}$ and a Curie-Weiss temperature $T_{cW} \approx 140 \text{ K}$. Additionally the thermal cycling dependence of the permittivity of the polycrystalline NaNbO_3 [17] is presented in (b). Here the arrows indicate the direction of thermal cycling process.

Fig. 6.6 illustrates a comparison of the temperature dependence of the $\text{Na}_{1.7}\text{NbO}_{3+6}$ film, a typical representative of a nominally stoichiometric NaNbO_3 film, and an unstrained NaNbO_3 polycrystal. Both films are deposited on $(110)\text{NdGaO}_3$ and possess a thickness of 27 nm. The results measured along $[1\bar{1}0]\text{NdGaO}_3$ for both films are discussed in this chapter. In contrast to the stoichiometric NaNbO_3 film, the $(\text{NaNbO}_3)_{0.915}(\text{Na}_3\text{NbO}_4)_{0.085}$ film shows:

- (i) A huge anomalous thermal hysteresis upon cooling and heating. The peak position in permittivity, i.e. T_{max} , is shifted by ~ 82 K, the difference in the maximum permittivity, i.e. ϵ'_{max} , for cooling and heating exceeds 400 for a large temperature regime around room temperature. The reference sample (Fig. 6.6(b)) shows no hysteretic behavior at all. However, the unstrained NaNbO_3 polycrystal does show a quite similar thermal hysteresis, but at much higher temperature (i.e. around 620 – 660 K).
- (ii) Both peaks in the permittivity of $(\text{NaNbO}_3)_{0.915}(\text{Na}_3\text{NbO}_4)_{0.085}$ are well defined and sharp, whereas the NaNbO_3 film shows the broad peak, which is typical for the phase transition from the dielectric to a relaxor-type ferroelectric state [9-11].
- (iii) The $(\text{NaNbO}_3)_{0.915}(\text{Na}_3\text{NbO}_4)_{0.085}$ sample shows no frequency dispersion, which again indicates the absence of relaxor-type behavior in this sample. In contrast, the stoichiometric NaNbO_3 film displays the typical frequency dispersion of a relaxor-type ferroelectric.

Before discussing the unusual hysteretic behaviors in detail, we briefly concentrate on the ferroelectric phase transition and the different ferroelectric phases of the off-stoichiometric sample $(\text{NaNbO}_3)_{0.915}(\text{Na}_3\text{NbO}_4)_{0.085}$.

The current-voltage characteristics (IVC) present an ideal tool to distinguish between the ferroelectric and the dielectric state. The insets of Fig. 6.6 show IVCs measured at the same temperature, i.e. 320K, in the regime of the hysteresis for cooling and heating. Upon cooling (red) a linear correlation between the current and the voltage indicates that the sample is in the dielectric state. Whereas the IVC measured at 320K upon heating (black) shows a small hysteresis and two peaks, which represent the switching current of the polarization. Thus within the branches of the hysteresis, the sample seems to be dielectric upon cooling, but ferroelectric upon heating. This observation is supported by the Curie-Weiss behavior according to $\epsilon'(T) = C/(T - T_{\text{CW}})$, with Curie constant $C = 1.56 \times 10^5$ K and Curie-Weiss temperature $T_{\text{CW}} \approx 132$ K. The Curie-Weiss fit agrees perfectly with the data obtained at high temperatures (above the peak) for heating and cooling (see Fig. 6.6). The value of the Curie

constant indicates that the film represents a displacement-type ferroelectric [30]. The relatively large difference of the Curie-Weiss temperature T_{CW} and the temperature of maximum permittivity T_{max} is not unusual for displacement-type ferroelectrics. Finally, there is the question whether, similar to the reference thin film, the ferroelectric state of the $(\text{NaNbO}_3)_{0.915}(\text{Na}_3\text{NbO}_4)_{0.085}$ sample represents a relaxor-type ferroelectric state. One argument against a relaxor-type state is the absence of the frequency dispersion that is typically observed in relaxor ferroelectrics at the transition from the dielectric to the ferroelectric state (i.e. around T_{max}). Another indication is represented by the sharpness of the peak at the transition. For that purpose, the transition range is described by a Lorentz simulation $(\epsilon'_{max} - 1)/\epsilon' = (T - T_{max})^\gamma / 2\sigma^2$ [62], with γ representing the degree of the dielectric relaxation. In contrast to the stoichiometric NaNbO_3 film (Fig. 6.6(b)), which shows a diffuse transition with $\gamma \approx 1.86$, we obtain values of $\gamma \approx 0.99$ on heating and $\gamma \approx 0.98$ on cooling for $(\text{NaNbO}_3)_{0.915}(\text{Na}_3\text{NbO}_4)_{0.085}$. A classic ferroelectric phase transition is described by $\gamma \approx 1$, whereas values of $\gamma \approx 1.5 - 2$ are associated with a relaxor-type ferroelectric transition, which indicates the existence of a 'classical' (i.e. non-relaxor) ferroelectric state in the $(\text{NaNbO}_3)_{0.915}(\text{Na}_3\text{NbO}_4)_{0.085}$ sample.

Based on the discussion above, we summarize that both peaks in the permittivity of the off-stoichiometric sample $\text{Na}_{1.17}\text{NbO}_{3+\delta}$ display a phase transition from a classic ferroelectric to a dielectric instead of that from a relaxor-type ferroelectric to a dielectric, which was observed in our stoichiometric NaNbO_3 films. We will now concentrate on the anomalous thermal hysteresis of permittivity of the $(\text{NaNbO}_3)_{0.915}(\text{Na}_3\text{NbO}_4)_{0.085}$ sample.

A thermal hysteresis has been reported for a few systems. These are, for instance, single crystals of NaNbO_3 [16,135] and BaTiO_3 [136], polycrystalline NaNbO_3 [17], polycrystalline tetragonal tungsten bronzes materials [30,137], Langmuir–Blodgett-deposited polymer films [138], or $(\text{PbTiO}_3)_y(\text{BiZn}_{0.5}\text{Ti}_{0.5}\text{O}_3)_{1-y}$ [139], $(\text{NaNbO}_3)_y(\text{SrZrO}_3)_{1-y}$ [45], or $(\text{NaNbO}_3)_x(\text{CaZrO}_3)_{1-x}$ [140] solid solutions.

Generally, there exist three possible explanations for the thermal hysteresis, i.e.

- (i) a first-order structural phase transition [16,141,142],
- (ii) the presence of two sets of active cation sites in combination with a weak superstructure that changes from an incommensurate to a commensurate structure on cooling [30,137], and

(iii) a 2-dimensional (2D) size effect [138].

First, in our case, we observe a huge difference in both T_{\max} and ϵ'_{\max} . The size of the hysteresis and the fact that our films are relatively thick compared to the Langmuir–Blodgett layers which showed the 2D size effect let us exclude option (iii), i.e. the 2D size effect. Second, in unstrained NaNbO_3 , a commensurate to incommensurate transition is known to occur at a temperature around 443 K leading to a featured anomaly [17]. However, this effect is also small and it does not show a thermal history. Therefore, we also rule out option (ii).

The thermal anomaly in $(\text{NaNbO}_3)_{0.915}(\text{Na}_3\text{NbO}_4)_{0.085}$ film shows quite similar feature compared to the thermal hysteresis obtained in polycrystalline NaNbO_3 (see Fig. 6.6(b)). Moreover, we obtained a hysteretic structural change exactly at the temperature where the thermal hysteresis in the permittivity takes place (see Fig. 6.5(b)). Therefore, only the first explanation in terms of a hysteretic structural transition might serve as an explanation. In case of the unstrained polycrystalline NaNbO_3 there exists a phase transition from the antiferroelectric P phase to the antiferroelectric R phase that takes place at about 600 – 628 K [17]. In our case, we measure only one component of the polarization, i.e. the in-plane polarization of an epitaxial film. Therefore, the ferroelectric state might appear differently in these experiments compared to the analysis of polarization of the polycrystalline sample. Nevertheless, we do see a phase transition (ferroelectric to dielectric) which is very similar in appearance, however at much lower temperature (i.e. room temperature) in our strained off-stoichiometric film

Consequently, the existing compressive strain seems to successfully reduce the thermal hysteresis from 620-660 K of the polycrystalline NaNbO_3 to more or less room temperature for the strained nominal $(\text{NaNbO}_3)_{0.915}(\text{Na}_3\text{NbO}_4)_{0.085}$ thin film (see Fig. 6.6). The absence of the relaxor behavior in the $(\text{NaNbO}_3)_{0.915}(\text{Na}_3\text{NbO}_4)_{0.085}$ sample nicely indicates that there is no significant relaxation of the compressive strain which was observed in stoichiometric NaNbO_3 thin films [9-11]. In combination with the RSM (Fig. 6.2) and XRD (Fig. 6.5(b)) measurements, we conclude that our $(\text{NaNbO}_3)_{0.915}(\text{Na}_3\text{NbO}_4)_{0.085}$ sample is more strained than NaNbO_3 thin films with comparable thickness. This might be caused by the stabilizing or buffering effect of the Na_3NbO_4 nanoprecipitates which most likely are homogeneous distributed in the NaNbO_3 film. This might also hold for the “purity” of the NaNbO_3 phase.

6.3. Rayleigh analysis of the strained $\text{Na}_{1.17}\text{NbO}_{3+\delta}$ film

In order to support this explanation (especially the delay of the phase transition upon cooling), we performed detailed Rayleigh analysis on the heating and cooling cycle. Fig. 6.7 shows typical examples of the electric field dependence of the permittivity for the cooling and heating cycle. The ac electric field was varied in steps of $0.05 \text{ V}/\mu\text{m}$ between 0.1 and $1 \text{ V}/\mu\text{m}$. The data display a perfect linear relation between the permittivity and E_{ac} , which can be described by the classical Rayleigh law [125] $\epsilon' = \epsilon'_{init} + \alpha E_{ac}$, where ϵ'_{init} represents the initial (reversible) permittivity at zero electric field and α the Rayleigh coefficient that describes the irreversible properties of the polarization. In classical ferroelectrics ϵ'_{init} represents contribution to the permittivity arising from the intrinsic lattice polarization and the reversible domain wall motions, whereas α describes mainly the presence and the pinning of ferroelectric domain walls [126]. Since the domain walls only exist in the ferroelectric state, α can be used to characterize the ferroelectric state.

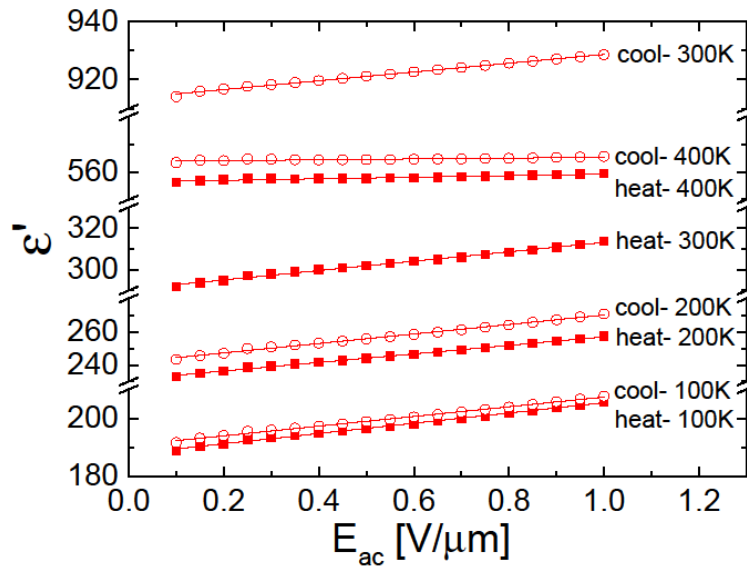


Fig. 6.7: Electric field dependence of the permittivity measured at 100 kHz and different temperatures on both heating (solid symbols) and cooling (open symbols) for the sample of $(\text{NaNbO}_3)_{0.915}(\text{Na}_3\text{NbO}_4)_{0.085}$. The lines represent linear fits according to the Rayleigh law.

The resulting initial permittivity ϵ'_{init} and the normalized Rayleigh coefficient α/ϵ'_{init} for the cooling and heating cycle of nominal $(\text{NaNbO}_3)_{0.915}(\text{Na}_3\text{NbO}_4)_{0.085}$ are given in Fig. 6.8. The

intrinsic (reversible) contribution ϵ'_{init} is very similar to ϵ' shown in Fig. 6.6. This was to be expected, since the electric field used for the measurement of ϵ' was quite small, i.e. 0.2 V/ μm .

However, the normalized irreversible polarization $\alpha/\epsilon'_{\text{init}}$ (Fig. 6.8(b)) shows some very interesting features. The value of $\alpha/\epsilon'_{\text{init}}$ ranges from 0 to 2.2×10^{-8} m/V, which is comparable to the range of values given for pinning effect in the literature [12,126,127,129-132]. However, it is clearly smaller than the value $(\alpha/\epsilon'_{\text{init}})_{\text{max}} = 7.4 \times 10^{-8}$ m/V that was obtained for the stoichiometric NaNbO_3 film that showed relaxor-type behavior (see Fig. 6.9). This might be taken as another indication, that in this case no PNRs are present in this film.

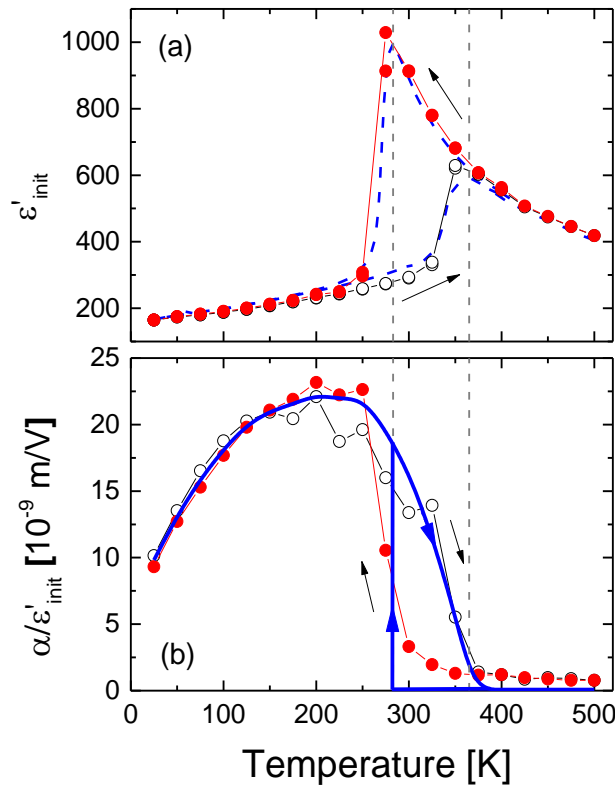


Fig. 6.8: Temperature dependence of the initial permittivity ϵ'_{init} (a) and the normalized Rayleigh parameters $\alpha/\epsilon'_{\text{init}}$ (b) for cooling (solid symbols) and heating (open symbols) for the $(\text{NaNbO}_3)_{0.915}(\text{Na}_3\text{NbO}_4)_{0.085}$ film. For comparison, the permittivity measured at $E_{\text{ac}} = 0.2$ V/ μm is added by the blue dashed line in (a). The blue solid line in (b) serves as a guide for the eye for the idealized hysteretic temperature dependence. The two vertical lines mark the position of the transition from dielectric to ferroelectric behavior for cooling and heating, respectively.

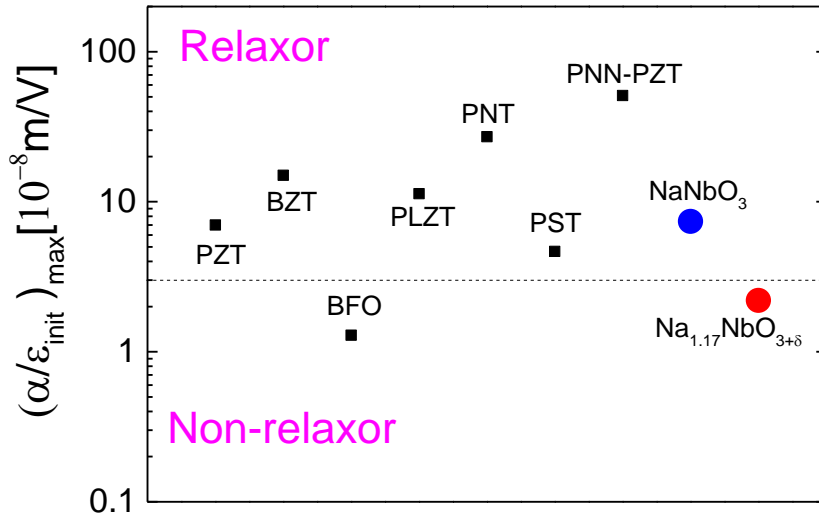


Fig. 6.9: A comparison of the maximum normalized Rayleigh parameters of the $(\text{NaNbO}_3)_{0.915}(\text{Na}_3\text{NbO}_4)_{0.085}$ film (red circle), the stoichiometric relaxor-type NaNbO_3 film (blue circle), with literature values for various relaxor and non-relaxor type ferroelectrics [12,126,127,129-132]. Except for BFO and $(\text{NaNbO}_3)_{0.915}(\text{Na}_3\text{NbO}_4)_{0.085}$ all systems are known or most likely relaxor-type ferroelectrics.

Obviously, $\alpha \approx 0$ in the dielectric state above the phase transition. In the ferroelectric state, irreversibility sets in, e.g. domains are present and domain wall pinning contributes to the irreversibility. The typical temperature dependence in the ferroelectric state is dome-like [7-11]. This is caused by the fact that at the phase transition ferroelectric domains start to exist, however, the domain wall pinning is weak. With decreasing temperature, the pinning increases, therefore α increases. Finally, at low temperature, domain walls start to become immobile. As a consequence, α decreases again. Thus, the dome-like shape of $\alpha/\epsilon'_{\text{init}}$ resembles the classical behavior of a ferroelectric. This is the behavior observed for the heating cycle. However, for the cooling cycle, we observe a delay of the transition and then an abrupt increase of the Rayleigh coefficient just at the transition to the ferroelectric state. This behavior (idealized by the sketch in Fig. 6.8(b)) is a clear indication for the delayed phase transition upon cooling, and, thus, represents another fingerprint for the explanation of the thermal hysteresis in terms of a delayed phase transition compared to that observed in unstrained bulk material at higher temperature. The temperatures of the phase transition agree quite nicely with the temperature of the structural transition observed in the film (see Fig. 6.5).

6.4. Summary

In summary of this chapter:

- (i) NaNbO_3 film with excess of Na can be grown epitaxially on $(110)\text{NdGaO}_3$.
- (ii) As a result of the excess Na, these films are composed of two different phases, i.e. NaNbO_3 and Na_3NbO_4 . The majority phase is NaNbO_3 , the Na_3NbO_4 phase seems to form precipitates with a diameter of a few nanometers that are most likely homogeneously embedded in the NaNbO_3 phase.
- (iii) The Na_3NbO_4 nanoprecipitates seem to stabilize the film. The majority phase NaNbO_3 is homogeneously strained throughout the film. The resulting out-of-plane lattice parameter is larger compared to that of the strained stoichiometric NaNbO_3 films.
- (iv) The off-stoichiometric NaNbO_3 film shows a phase transition around room temperature which is hysteretic upon thermal cycling. This phase transition is visible in
 - (a) the structural analysis and
 - (b) the electronic analysis in form of a hysteretic transition from a dielectric (at high temperature) to a ferroelectric (at low temperature) state.

The phase transition resembles the hysteretic transition from the R to the P antiferroelectric state observed in unstrained NaNbO_3 . Although we cannot prove the antiferroelectric state via our electronic measurements, that are restricted to the analysis of the in-plane polarization, we believe that this is a perfect demonstration of

- (a) strain conservation in our film via nanoprecipitate and
- (b) the shift of the transition to lower temperature via compressive strain.

7. Conclusions

Oxides represent very important components for modern electronics among others due to their prominent ferroelectric properties. However, since they show these extraordinary features especially at the ferroelectric phase transition typically far from room temperature, it is necessary to manipulate these systems to shift this behavior towards operating temperature, i.e. room temperature. For epitaxially grown films this can be achieved via strain.

In this thesis, the structural and electronic properties of epitaxially strained $\text{Na}_{1+x}\text{NbO}_{3+\delta}$ thin films grown on NdGaO_3 are discussed. The results are analyzed in terms of existing as well as novel models. The incorporated anisotropic strain and the deviation from the nominal stoichiometry are proved to play major roles for the modification of the electronic properties in these films. The essences of these observations are:

- (i) Standard XRD, especially RSM measurements, indicate that $\text{Na}_{1+x}\text{NbO}_{3+\delta}$ without and with excess of Na can be grown epitaxially on (110) NdGaO_3 . All $\text{Na}_{1+x}\text{NbO}_{3+\delta}$ films (up to $d \approx 140$ nm) are strained, however, a plastic strain relaxation sets in already for relatively thin films ($d \approx 10 - 15$ nm). With increasing Na excess, a secondary phase forms, i.e. Na_3NbO_4 . The majority phase is still NaNbO_3 , however Na_3NbO_4 seems to form precipitates with a diameter of a few nanometers that are most likely homogeneously embedded in the NaNbO_3 phase. Astonishingly, a nominally off-stoichiometric $\text{Na}_{1.17}\text{NbO}_{3+x}$ film is more strained than the stoichiometric NaNbO_3 films. This is most likely due to the buffering and stabilizing effects of the Na_3NbO_4 nanoprecipitates.
- (ii) The compressive strain leads to a ferroelectric phase transition at low temperature. As a result, for instance the permittivity at room temperature is significantly increased.

In case of the nominally stoichiometric NaNbO_3 films this phase transition takes place at a temperature of 125 – 147 K and is a transition from the dielectric state at high temperature to a relaxor-type ferroelectric state at low temperature. This phase transition is either a new phase transition induced by the strain or a known phase transition (e.g. the transition at ~ 630 K) shifted to lower temperature due to the strain. The transition temperature depends on the strain (see (iii) below) and strain relaxation.

In case of the off-stoichiometric film with nominal composition $\text{Na}_{1.17}\text{NbO}_{3+\delta}$, the compressive strain leads to a phase transition around room temperature which is hysteretic upon thermal cycling. This phase transition is visible in (a) the structural analysis and (b) the electronic analysis. It perfectly resembles the hysteretic transition from the R to the P antiferroelectric state observed in unstrained NaNbO_3 at 620 – 660 K. Although we cannot prove the antiferroelectric state via our electronic measurements, that are restricted to the analysis of the in-plane polarization, we believe that this is a perfect demonstration of (a) strain conservation in our film via nanoprecipitates and (b) the shift of the transition to lower temperature via compressive strain.

- (iii) The orthorhombic structure of the substrate leads to an anisotropy in-plane strain and, thus, anisotropic ferroelectric properties. The anisotropy of the permittivity (up to $\epsilon'(L)/\epsilon'(S) \approx 2.1$ for the nominally stoichiometric NaNbO_3 films), the maxima in the permittivity, and the transition temperature depend on the orientation of the electric field with respect to the crystallographic orientation of the film and the substrate. However, our results indicate that the “classical model” for the mismatch based on energy minimization and the room temperature lattice of unstrained NaNbO_3 cannot explain the shift of T_C with the strain. This model actually tries to match the two not perfect square (quasi-square) lattices of the substrate and the film. A new “square lattice” model is proposed, which assumes that the film adapts a square shaped in-plane structure at the interface to the substrate during the growth at elevated temperature at ~ 1000 K which is then strained according to the anisotropic lattice of the substrate. In this model, the perfect square lattice of the growing film is matched on the quasi-square lattice of the substrate. The new model nicely fits the experimental results.
- (iv) Normally the strain is supposed to cause a minute compositional deviation from the perfect stoichiometry. The resulting inhomogeneity in the composition is assumed to lead to the formation of PNRs which are the basis for the relaxor-type behavior at low temperature. We demonstrated that our compressively strained, nominally stoichiometric NaNbO_3 films exhibit a typical relaxor-type behaviors, e.g. a broad and frequency-dispersive peak in the ϵ' -versus- T curves that are interpreted via Vogel-Fulcher and Lorentz analyses. The temperature T_{max} is defined as the characteristic temperature of this transition. This relaxor-type behavior leads to a strong electric field dependence of the permittivity. The dc tunability of up to 6% for $1 \text{ V}/\mu\text{m}$ in the

paraelectric regime is comparable to that of the tunable classical ferroelectric materials, whereas an unusually large enhancement of the permittivity of up to 29% is observed if the ac-field is enhanced by $1 \text{ V}/\mu\text{m}$.

By combining frequency dispersive and electric field (ac and dc) dependent measurements, we succeeded to estimate the size of the 'active' PNRs at the freezing temperature. According to our model, the volume of the PNRs depends on the applied ac field and varies from 70 to 270 nm^3 in the regime of the freezing temperature ($80 - 150 \text{ K}$). The resulting diameter of the PNR (assuming idealized spherical PNRs) at the freezing temperature ranges from $\sim 5.2 \text{ nm}$ to $\sim 8 \text{ nm}$ for large and small fields, respectively. These values are in agreement with literature values for classical relaxor-type ferroelectrics.

We believe that our observations help to understand the correlation between strain engineering and stoichiometry in ferroelectric thin films. The increase of off-stoichiometry strongly modifies the structural and ferroelectric properties of oxide thin films. It does not only strongly affect the transition temperature to the ferroelectric state and, thus, all ferroelectric properties. It can also lead to a change of the behavior of the material in the ferroelectric state ranging from the classical ferroelectric behavior (observed for samples with perfect stoichiometry [13]), relaxor-type behavior (slightly off-stoichiometric sample due to strain), to classical ferroelectric behavior (for large off-stoichiometry) with a secondary phase Na_3NbO_4 .

In conclusion, not only the possibility to engineer the ferroelectric properties via strain, but also the prominent relaxor properties of the strained NaNbO_3 films or thermal hysteretic behaviors of $\text{Na}_{1.17}\text{NbO}_{3+\delta}$ thin film represent interesting opportunities for basic research and understanding as well as possible applications of this type of ferroelectrics. The idea of introducing off-stoichiometry additionally to epitaxial growth also opens a new horizon of engineering a '3D' strain in comparison to the classical in-plane strain (via mismatch of the lattice or thermal expansion coefficient) or out-of-plane strain (via vertical aligned nanocomposites).

References

- [1] J. Valasek, Phys. Rev. **17**, 475 (1921).
- [2] G. Busch and P. Scherrer, Naturwissenschaft **23**, 737 (1935).
- [3] W. Känzig, Ferroelectrics **74**, 285 (1987).
- [4] J. F. Scott, Science **315**, 954 (2007).
- [5] L. E. Cross and R. E. Newnham, Ceramics and Civilization **111**, 289 (1987).
- [6] J. H. Haeni, P. Irvin, W. Chang, R. Uecker, P. Reiche, Y. L. Li, S. Choudhury, W. Tian, M. E. Hawley, B. Craigo, A. K. Tagantsev, X. Q. Pan, S. K. Streiffer, L. Q. Chen, S. W. Kirchoefer, J. Levy, and D. G. Schlom, Nature **430**, 758 (2004).
- [7] R. Wördenweber, E. Hollmann, R. Kutzner, and J. Schubert, J. Appl. Phys. **102**, 044119 (2007).
- [8] R. Wördenweber, J. Schubert, T. Ehlig, and E. Hollmann, J. Appl. Phys. **113**, 164103 (2013).
- [9] R. Wördenweber, J. Schwarzkopf, E. Hollmann, A. Duk, B. Cai, M. Schmidbauer, Appl. Phys. Lett. **103**, 132908 (2013).
- [10] Biya Cai, J. Schwarzkopf, E. Hollmann, M. Schmidbauer, M. O. Abdel-Hamed, and R. Wördenweber, J. Appl. Phys. **115**, 224103 (2014).
- [11] Biya Cai, J. Schwarzkopf, E. Hollmann, D. Braun, M. Schmidbauer, T. Grellmann, R. Wördenweber, Phys. Rev. B **93**, 224107 (2016).
- [12] J. F. Ihlefeld, C. M. Folkman, S. H. Baek, G. L. Brennecke, M. C. George, J. F. Carroll III, and C. B. Eom, Appl. Phys. Lett. **97**, 262904 (2010).
- [13] Che-Hui Lee, V. Skoromets, M. D. Biegalski, S. Lei, R. Haislmaier, M. Bernhagen, R. Uecker, Xiaoxing Xi, V. Gopalan, X. Martí, S. Kamba, P. Kužel and D. G. Schlom, Appl. Phys. Lett. **102**, 082905 (2013).
- [14] N. A. Pertsev, A. G. Zembilgotov, and A. K. Tagantsev, Phys. Rev. Lett. **80**, 1988 (1998).
- [15] N. A. Pertsev, A. K. Tagantsev, and N. Setter, Phys. Rev. B **61**, R825 (2000); **65**, 219901(E) (2002).
- [16] G. Shirane, R. Newnham, and R. Pepinsky, Phys. Rev. **96**, 581 (1954).
- [17] Hanzheng Guo, Hiroyuki Shimizu, and Clive A. Randall, Appl. Phys. Lett. **107**, 112904 (2015).
- [18] R. Wördenweber, *Ferroelectric Thin Layers, Comprehensive Semiconductor Science and Technology* (Elsevier, Amsterdam, 2011).
- [19] Igor Levin, Martin C. Stennett, Gabrielle C. Miles, David. I. Woodward, Anthony R. West, and Ian M. Reaney, Appl. Phys. Lett. **89**, 122908 (2006).
- [20] T. M. McQueen, D. V. West, B. Muegge, Q. Huang, K. Noble, H. W. Zandbergen and R. J. Cava, J. Phys.: Condens. Matter **20**, 235210 (2008).

-
- [21] Hiroshi Irie, Masaru Miyayama, and Tetsuichi Kudo, *J. Appl. Phys.* **90**, 4089 (2001).
- [22] V. M. Goldschmidt, *Die Naturwissenschaften* **14**, 477 (1926).
- [23] G. Goodman, *J. Am. Ceram. Soc.* **36**, 368 (1953).
- [24] M. E. Lines, A. M. Glass, *Principles and Applications of Ferroelectrics and Related Materials* (Clarendon Press, Oxford, 1977).
- [25] G. H. Olsen, U. Aschauer, N. A. Spaldin, S. M. Selbach, and T. Grande, *Phys. Rev. B* **93**, 180101(R) (2016).
- [26] P. B. Jamieson, S. C. Abrahams, and J. L. Bernstein, *J. Chem. Phys.* **48**, 5048 (1968).
- [27] P. B. Jamieson, S. C. Abrahams, and J. L. Bernstein, *J. Chem. Phys.* **50**, 4352 (1969).
- [28] X. H. Zheng and X. M. Chen, *J. Mater. Res.* **17**, 1664 (2002).
- [29] X. H. Zheng and X. M. Chen, *Solid State Commun.* **125**, 449 (2003).
- [30] X. L. Zhu and X. M. Chen, *Appl. Phys. Lett.* **96**, 032901 (2010).
- [31] B. Aurivillius, *Ark. Kemi* **1**, 499 (1950).
- [32] E. C. Subbarao, *J. Phys. Chem. Solids* **23**, 665 (1962).
- [33] E. C. Subbarao, *J. Am. Ceram. Soc.* **45**, 166 (1962).
- [34] C. F. Pulvari and A. S. Delapaz, *J. Appl. Phys.* **37**, 1754 (1966).
- [35] Yuji Noguchi, Muneyasu Suzuki, Yuuki Kitanaka, Shunsuke Teranishi, and Masaru Miyayama, *Appl. Phys. Lett.* **93**, 032904 (2008).
- [36] Y. Saito, H. Takao, T. Tani, T. Nonoyama, K. Takatori, T. Homma, T. Nagaya, M. Nakamura, *Nature* **432**, 84 (2004).
- [37] Y. I. Yuzyuk, R. A. Shakhovoy, S. I. Raevskaya, I. P. Raevski, M. El Marssi, M. G. Karkut, and P. Simon, *Appl. Phys. Lett.* **96**, 222904 (2010).
- [38] V. Lingwal and N. S. Panwar, *J. Appl. Phys.* **94**, 4571 (2003).
- [39] S. K. Mishra, N. Choudhury, S. L. Chaplot, P. S. R. Krishna, and R. Mittal, *Phys. Rev. B* **76**, 024110 (2007).
- [40] H. D. Megaw, *Ferroelectrics* **7**, 87 (1974).
- [41] E. Cross, *Nature* **432**, 24 (2004).
- [42] M. C. Morris, H. F. McMurdie, E. H. Evans, B. Paretzkin, H. S. Parker, N. C. Panagiotopoulos, and C. R. Hubbard, *“Standard X-ray Diffraction Powder Patterns”* Natl. Bur. Stand. (U.S.) Monograph No. 18 (National Bureau of Standards, Gaithersburg, 1981).
- [43] A. Vailionis, H. Boschker, W. Siemons, E. P. Houwman, D. H. A. Blank, G. Rijnders, and G. Koster, *Phys. Rev. B* **83**, 064101 (2011).
- [44] Peng Li, Shuxin Ouyang, Guangcheng Xi, Tetsuya Kako, and Jinhua Ye, *J. Phys. Chem. C* **116**, 7621 (2012).
- [45] Hanzheng Guo, Hiroyuki Shimizu, Youichi Mizuno, and Clive A. Randall, *J. Appl. Phys.* **117**, 214103 (2015).
-

-
- [46] M. Dawber, K. M. Rabe, J. F. Scott, *Rev. Mod. Phys.* **77**, 1083 (2005).
- [47] N. Setter, D. Damjanovic, L. Eng, G. Fox, S. Gevorgian, S. Hong, A. Kingon, H. Kohlstedt, N. Y. Park, G. B. Stephenson, I. Stolitchnov, A. K. Taganstev, D. V. Taylor, T. Yamada, and S. Streiffer, *J. Appl. Phys.* **100**, 051606 (2006).
- [48] T. Saito, H. Adachi, T. Wada, and H. Adachi, *Jpn. J. Appl. Phys.* **44**, 6969 (2005).
- [49] S. Yamazoe, A. Kohori, H. Sakurai, Y. Kitanaka, Y. Noguchi, M. Miyayama, and T. Wada, *J. Appl. Phys.* **112**, 052007 (2012).
- [50] T. Mino, S. Kuwajima, T. Suzuki, I. Kanno, H. Kotera, and K. Wasa, *Jpn. J. Appl. Phys.* **46**, 6960 (2007).
- [51] W. J. Maeng, I. Jung, and J. Y. Son, *Journal of Crystal Growth* **349**, 1 (2012).
- [52] J. Schwarzkopf, M. Schmidbauer, T. Remmele, A. Duk, A. Kwasniewski, S. Bin Anooz, A. Devi, and R. Fornari, *J. Appl. Crystallogr.* **45**, 1015 (2012).
- [53] L. E. Cross, *Ferroelectrics* **76**, 241 (1987).
- [54] D. Damjanovic, *Rep. Prog. Phys.* **61**, 1267 (1998).
- [55] F. Jona and G. Shirane, *Ferroelectric Crystals* (Dover Publications Inc. New York, 1993).
- [56] C. Kittel, *Introduction to Solid State Physics* (8th ed. Wiley, 2005).
- [57] W. Cochran, *Adv. Phys.* **10**, 401 (1961).
- [58] Shozo Sawada, Shoichiro Nomura, Shin'ichi Fujii, and Ikushi Yoshida., *Phys. Rev. Lett.* **1**, 320 (1958).
- [59] G. A. Smolenskii and V. A. Isupov, *Zh. Tekh. Fiz.* **24**, 1375(1954).
- [60] G. A. Samara, *J. Phys.: Condens. Matter*, **15**, 367 (2003).
- [61] H. Vogel, *Phys. Z.* **22**, 645 (1921); G. S. Fulcher, *J. Am. Ceram. Soc.* **8**, 339 (1925).
- [62] A. A. Bokov and Z.-G. Ye, *Solid State Commun.* **116**, 105 (2000).
- [63] E. Brown, C. R. Ma, J. Acharya, B. H. Ma, J. W, and J. Li, *ACS Appl. Mater. Interfaces* **6**, 22417 (2014).
- [64] I.-K. Jeong, T. W. Darling, J. K. Lee, Th. Proffen, R. H. Heffner, J. S. Park, K. S. Hong, W. Dmowski, and T. Egami, *Phys. Rev. Lett.* **94**, 147602 (2005).
- [65] D. S. Fu, H. Taniguchi, M. Itoh, S.-Y. Koshihara, N. Yamamoto, and S. Mori, *Phys. Rev. Lett.* **103**, 207601 (2009).
- [66] B. E. Vugmeister, *Phys. Rev. B* **73**, 174117 (2006).
- [67] G. A. Smolenskii, V. A. Isupov, A. I. Agranovskaya, and S. N. Popov, *Sov. Phys. Solid State*, **2**, 2906 (1960).
- [68] D. Viehland, S. J. Jang, L. E. Cross, and M. Wuttig, *J. Appl. Phys.* **68**, 2916 (1990).
- [69] L. E. Cross, *Ferroelectrics*, **151**, 305 (1994).
- [70] B. E. Vugmeister and M. D. Glinchuk, *Rev. Mod. Phys.* **62**, 993 (1990).
-

-
- [71] E. V. Colla, E. Yu. Koroleva, N. M. Okuneva, S. B. Vakhrushev, Phys. Rev. Lett. **74**, 1681 (1995).
- [72] A. Levstik, Z. Kutnjak, C. Filipič, and R. Pirc, Phys. Rev. B **57**, 11204 (1998).
- [73] R. Pirc and R. Blinc, Phys. Rev. B **60**, 13470 (1999).
- [74] V. Bobnar, Z. Kutnjak, R. Pirc, R. Blinc, and A. Levstik, Phys. Rev. Lett. **84**, 5892 (2000).
- [75] A. E. Glazounov and A. K. Tagansev, Ferroelectrics **221**, 57 (1999).
- [76] V. Westphal, W. Kleemann, and M. D. Glinchuk, Phys. Rev. Lett. **68**, 847 (1992).
- [77] R. Fisch, Phys. Rev. B **67**, 094110 (2003).
- [78] D. S. Fu, H. Taniguchi, M. Itoh and S. Mori, Chapter3, *Advances in Ferroelectrics* (InTech, 2012).
- [79] S. N. Dorogovtsev and N. K. Yushin, Ferroelectrics **112**, 18 (1990).
- [80] S. B. Vakhrushev, B. E. Kvyatkovskiy, A. A. Naberezhnov, N. M. Okuneva, and B. Toperverg, Physica B **156-157**, 90 (1989).
- [81] D. Viehland, S. J. Jang, L. E. Cross, and M. Wuttig, Phys. Rev. B **46**, 8003 (1992).
- [82] K. Binder and K. Schroder, Solid State Commun. **18**, 1361 (1976).
- [83] Y. Imry and S. K. Ma, Phys. Rev. Lett. **35**, 1399 (1975).
- [84] A. A. Bokov, Z.-G. Ye, J. Mater. Sci. **41**, 31 (2006).
- [85] K. A. Muller, W. Berlinger, and E. Tossati, Z. Phys. B **84**, 277 (1991).
- [86] M. B. Smith, K. Page, T. Siegrist, P. L. Redmond, E. C. Walter, R. Seshadri, L. E. Brus, and M. L. Steigerwald, J. Am. Chem. Soc. **130**, 6955 (2008).
- [87] B. Jaffe, W. R. Cook, and H. L. Jaffe, *Piezoelectric ceramics* (Academic Press, London and New York, 1971).
- [88] A. M. Glazer and S. A. Mabud, Acta Crystallogr. B **34**, 1065 (1978).
- [89] Wanlin Zhu, Ichiro Fujii, Wei Ren, and Susan Trolier-McKinstry, J. Appl. Phys. **109**, 064105 (2011).
- [90] G. H. Haertling, J. Am. Ceram. Soc. **82**, 797 (1999).
- [91] Rudiger-A. Eichel, J. Am. Ceram. Soc., **91**, 691 (2008).
- [92] C. A. Randall, A. S. Bhalla, T. R. ShROUT, and L. E. Cross, J. Mater. Res. **5**, 829 (1990).
- [93] M. W. Lufaso, and P. M. Woodward, Acta Cryst. B **57**, 725 (2001).
- [94] J. G. Bednorz and K. A. Muller, Phys. Rev. Lett. **52**, 2289 (1984).
- [95] C. Ang, Z. Yu, P. M. Vilarinho, and J. L. Baptista, Phys. Rev. B **57**, 7403 (1998).
- [96] Darrell G. Schlom, Long-Qing Chen, Chang-Beom Eom, Karin M. Rabe, Stephen K. Streiffer, and Jean-Marc Triscone, Annu. Rev. Mater. Sci. **37**, 589 (2007).
- [97] A. Duk, "Relationships between strain, ferro- and piezoelectric properties in functional oxide thin films" Ph.D. dissertation, Humboldt University of Berlin, 2013.

-
- [98] R. Dirsyte, J. Schwarzkopf, G. Wagner, J. Lienemann, M. Busch, H. Winter, and R. Fornari, *Appl. Surf. Sci.* **255**, 8685 (2009).
- [99] J. Sellmann, J. Schwarzkopf, A. Kwasniewski, M. Schmidbauer, D. Braun, A. Duk, *Thin Solid Films* **570**, 107 (2014).
- [100] Jan Sellmann, "Impact of strain and composition on structural and piezo-/ferroelectric properties of epitaxial NaNbO_3 and $\text{K}_x\text{Na}_{1-x}\text{NbO}_3$ thin films and superlattices grown by PLD", Ph.D. dissertation, Technical University of Berlin, 2015.
- [101] M. Schmidbauer, P. Schäfer, S. Besedin, D. Grigoriev, R. Köhlerb and M. Hanke, *J. Synchrotron Rad.* **15**, 549 (2008).
- [102] Produktinfos, Allresist, 2014, http://www.allresist.com/wp-content/uploads/sites/2/2014/02/allresist_produkinfos_ar-p630-690_englisch.pdf.
- [103] O. G. Vendik, S. P. Zubko, and M. A. Nikol'skii, *Technical Physics* **44**, 349 (1999); O. G. Vendik, and M. A. Nikol'skii, *Technical Physics* **46**, 112 (2001).
- [104] S. S. Gevorgian, T. Martinsson, P. L. Linner, and E. L. Kollberg, *IEEE Trans. Microwave Theory Tech.* **44**, 896 (1996).
- [105] E. Chen and S. Y. Chou, *IEEE Trans. Microwave Theory Tech.* **45**, 939 (1997).
- [106] A. Infortuna, P. Muralt, M. Cantoni, and N. Setter, *J. Appl. Phys.* **100**, 104110 (2006).
- [107] Dinghua Bao, Sung Kyun Lee, Xinhua Zhu, M. Alexe, and D. Hesse, *Appl. Phys. Lett.* **86**, 082906 (2005).
- [108] M. Schmidbauer, A. Kwasniewski and J. Schwarzkopf, *Acta Cryst. B* **68**, 8 (2012).
- [109] J. Schwarzkopf, D. Braun, M. Schmidbauer, A. Duk, and R. Wördenweber, *J. Appl. Phys.* **115**, 204105 (2014).
- [110] D. Bolten, O. Lohse, M. Grossmann, and R. Waser, *Ferroelectrics* **221**, 251(1999).
- [111] O. Lohse, M. Grossmann, U. Boettger, D. Bolten, and R. Waser, *J. Appl. Phys.* **89**, 2332 (2001).
- [112] R. Blinc, *Advanced Ferroelectricity* (Oxford University Press, New York, 2011).
- [113] G. Xu, G. Shirane, J. R. D. Copley and P. M. Gehring, *Phys. Rev. B* **69**, 064112 (2004).
- [114] P. B. Groszewicz, H. Breitzke, R. Dittmer, E. Sapper, W. Jo, G. Buntkowsky, and J. Rödel, *Phys. Rev. B* **90**, 220104(R) (2014).
- [115] R. Blinc, V. Laguta, and B. Zalar, *Phys. Rev. Lett.* **91**, 247601 (2003).
- [116] G. Xu, Z. Zhong, Y. Bing, Z.G. Ye, C. Stock, and G. Shirane, *Phys. Rev. B* **70**, 064107 (2004).
- [117] N. Liu, R. Dittmer, R. W. Stark, and C. Dietz, *Nanoscale*, **7**, 11787 (2015); V. V. Shvartsman, W. Kleemann, T. Lukasiewicz, and J. Dec, *Phys. Rev. B*, **77**, 054105 (2008); V. V. Shvartsman, W. Kleemann, J. Dec, Z. K. Xu, and S. G. Lu, *J. Appl. Phys.*, **99**, 124111 (2006).

-
- [118] T. Shi, L. Xie, L. Gu, and J. Zhu, *Scientific Reports* **5**, 8606 (2015).
- [119] S. Prosandeev, D. W. Wang, A. R. Akbarzadeh, B. Dkhil, and L. Bellaiche, *Phys. Rev. Lett.* **110**, 207601 (2013).
- [120] H. W. Jang, A. Kumar, S. Denev, M. D. Biegalski, P. Maksymovych, C. W. Bark, C. T. Nelson, C. M. Folkman, S. H. Baek, N. Balke, C. M. Brooks, D. A. Tenne, D. G. Schlom, L. Q. Chen, X. Q. Pan, S. V. Kalinin, V. Gopalan, and C. B. Eom, *Phys. Rev. Lett.* **104**, 197601 (2010).
- [121] S. Wada, H. Adachi, and H. Kakemoto, H. Chazono, Y. Mizuno, H. Kishi and T. Tsurumi, *J. Mater. Res.* **17**, 457 (2002).
- [122] Z. Kighelman, D. Damjanovic, and N. Setter, *J. Appl. Phys.* **90**, 4682 (2001).
- [123] D. Viehland, S. J. Jang, L. E. Cross, and M. Wuttig, *J. Appl. Phys.* **69**, 414 (1991).
- [124] R. Pirc and R. Blinc, *Phys. Rev. B* **76**, 020101 (R) (2007).
- [125] L. Rayleigh, *Philos. Mag.* **23**, 225 (1887); D. Jiles, *Introduction to Magnetism and Magnetic Materials* (Chapman and Hall, London, 1991).
- [126] D. V. Taylor, and D. Damjanovic, *J. Appl. Phys.* **82**, 1973 (1997).
- [127] B. H. Ma, Z. Q. Hu, S. S. Liu, S. Tong, M. Narayanan et al. *Appl. Phys. Lett.* **102**, 202901 (2013).
- [128] Y. P. Shi and A.K. Soh, *Appl. Phys. Lett.* **99**, 092908 (2011).
- [129] J. Miao, J. Yuan, H. Wu, S. B. Yang, B. Xu, L. X. Cao, and B. R. Zhao, *Appl. Phys. Lett.* **90**, 022903 (2007).
- [130] Mao Ye, Haitao Huang, Tao Li, Shanming Ke, Peng Lin, Biaolin Peng, Manfang Mai, Qiu Sun, Xiang Peng, and Xierong Zeng, *Appl. Phys. Lett.* **107**, 202902 (2015).
- [131] Xiaohua Sun, Xiuneng Li, Shuang Hou, Caihua Huang, Jun Zou, Meiya Li, Tianyou Peng, Xing-zhong Zhao, *Appl. Phys. A* **114**, 777 (2014).
- [132] F. Griggio, S. Jesse, W. Qu, A. Kumar, O. Ovchinnikov, D. S. Tinberg, S. V. Kalinin, and S. Trolrier-McKinstry, *J. Appl. Phys.* **110**, 044109 (2011).
- [133] M. W. Shafer and R. Roy, *J. Am. Ceram. Soc.* **42**, 482 (1959).
- [134] V. S. Bondarev, A. V. Kartashev, M. V. Gorev, I. N. Flerov, E. I. Pogorel'tsev, M. S. Molokeesov, S. I. Raevskaya, D. V. Suzdalev, and I. P. Raevskii, *Phys. Solid State* **55**, 821 (2013).
- [135] L. E. Cross and B. J. Nicholson, *Phil. Mag.*, **46**, 453 (1955).
- [136] Walter J. Merz, *Phys. Rev.* **76**, 1221 (1949).
- [137] Marta Prades, Héctor Beltrán, Nahum Masó, Eloisa Cordoncillo, and Anthony R. West, *J. Appl. Phys.* **104**, 104118 (2008).
- [138] A. V. Bune, V. M. Fridkin, Stephen Ducharme, L. M. Blinov, S. P. Palto, A. V. Sorokin, S. G. Yudin and A. Zlatkin, *Nature*, **391**, 874 (1998).
-

-
- [139] Ma. R. Suchomel and P. K. Davies, *Appl. Phys. Lett.* **86**, 262905 (2005).
- [140] Hiroyuki Shimizu, Hanzheng Guo, Sebastian E. Reyes-Lillo, Youichi Mizuno, Karin M. Rabe and Clive A. Randall, *Dalton Trans.* **44**, 10763 (2015).
- [141] A. M. Glazer and H. D. Megaw, *Acta Cryst.* **A29**, 489 (1973).
- [142] S. K. Mishra, R. Mittal, V. Yu. Pomjakushin, and S. L. Chaplot, *Phys. Rev. B* **83**, 134105 (2011).

Acknowledgements

I would like to first thank Prof. Roger Wördenweber who is my supervisor during my Ph. D study. He patiently guided me into the field of 'Ferroelectric', carefully taught me how to manage these characterization devices, heartily instructed me to keep optimistic when I suffered from the work in the laboratory, and earnestly tutored me to be always curious and passionate to the work I am interested. He also helped me a lot in my daily life, the topics in our dairy morning coffee-time cover not only science, but breaking news in the world, sports, national customs, and even politics. Without his supervision, I cannot achieve what I had done in the past 4 years.

I want to show my deep appreciations to Prof. Andreas Offenhäusser (the dean of Peter Grünberg Institute (PGI-8), Jülich Research Center) for giving me the chance to work at PGI-8. I am also deeply grateful to Dr. Eugen Hollmann for his support. Especially, the instruction of the bonder, XRD measurement and cleanroom work, the help for RBS measurements, the smart solutions on the design of the sample holder, and some valuable discussions and suggestions with respect to my work. I also want to express my gratitude to Rolf Kutzner for his support on triggering varieties of technical problems and these joke moments during the work. I also want to thank Dr. Stefan Trellenkamp for the help of E-beam writing lithography. Moreover, I am thankful to other colleagues, Tino Ehlig, Thomas Grellmann, Kyrylo Greben, Yang Dai, Alexandr Markov, Junmiao Wang, and Nikolaus Wolf for not only the nice questions and discussions but also the great soccer, barbeque, and carnival time. The international and friendly environment made by you benefits me a lot to work and live well at Jülich.

I am very thankful to our collaborating group at Leibniz Institute for Crystal Growth, Berlin, Germany. Their contributions play an important role in my Ph. D thesis. I cordially acknowledge Dr. Jutta Schwarzkopf for MOCVD deposition, great discussions, patient explanations and constructive suggestions, Dr. Jan Sellmann for PLD deposition, Dorothee Braun for AFM test, Christoph Feldt and Martin Schmidbauer for XRD tests, and Toni Markurt for TEM measurements.

I sincerely appreciate my friends. They shared the living tips, made parties for celebrations, did varieties of sport in our spare time, and helped me when I encountered problems. Without them, I cannot have such amazing 4 years in Germany.

I want to present my special thanks to China Scholarship Council (CSC) for the financial support during my whole Ph. D period. This scholarship gives me a golden chance to get my Ph. D degree in Germany.

The last but not least, I want to show my greatest acknowledgements to my family. My parents are always supportive behind me. They comforted me when I was frustrated, encouraged me when I felt unconfident, and motivated me when I were struggling. I must show my deepest gratitude to my wife, Xiaoqian Jiang who is also a Ph. D student at FZJ. Thank her for accompanying me in my life. Without her care, patience, encouragement, and support, I cannot accomplish my Ph. D thesis.

Statutory declaration in lieu of an oath

I hereby declare in lieu of an oath that I have completed the present Ph. D thesis entitled "*Manipulating the Structural and Electronic Properties of Epitaxial NaNbO₃ Films via Strain and Stoichiometry*" independently and without illegitimate assistance from third parties. I have use no other than the specified sources and aids. In case that the thesis is additionally submitted in an electronic format, I declare that the written and electronic versions are fully identical. The thesis has not been submitted to any examination body in this, or similar, form.

Biya Cai
Aug. 30, 2016

CURRICULUM VITAE

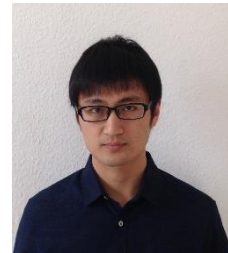
Biya Cai

Address: No.12 Grün Street

Jülich, Germany

Phone: (+49)176_8152_0417

Email: caibiya@hotmail.com or b.cai@fz-juelich.de



PERSONAL INFORMATION

Nationality: Chinese

Gender: Male

Birth Date: 05/10/1987

Marital: Married (no kids)

Webpage: https://www.researchgate.net/profile/Biya_Cai

EDUCATION

2012.11-2016.11 Ph.D, Physics. Cologne University (registering university) & Forschungszentrum Jülich (**working place**). 1-point (sehr gut, A⁺)

2009.9-2012.7 M.E, Materials Science and Engineering. China University of Geosciences, Beijing (CUGB)

2005.9-2009.7 B.E, Materials Science and Engineering. China University of Geosciences, Beijing(CUGB)
GPA 3.63 (5/90)

RESEARCH EXPERIENCE

2012.11-2016.11 “Tuning/Engineering ferroelectric properties of oxides films via strain” Ph. D Degree Dissertation, Forschungszentrum Jülich (FZJ) & Cologne University

2010.6-2012.7 “Preparation of Potassium Sulfate and Aluminum Sulfate by Sulfuric Acid Dissolved Kalsilite” Master Degree Dissertation, Intern National Laboratory of Mineral Materials (CUGB)

2009.7-2010.5 “Hydration Kinetics of Aluminate Cement containing Magnesium Aluminate Spinel” Intern National Laboratory of Mineral Materials (CUGB)

2008.12-2009.6 “Preparation of Potassium Sulfate and Calcium Carbonate by The Reaction of Phosphogypsum and Spent Carbonated Liquor” Bachelor Degree Dissertation, Intern National Laboratory of Mineral Materials (CUGB)

2007.6-2007.9 “The Ultra-fine Pulverization of Fritillaria Power Compound” The Power Engineering Laboratory of Tsinghua University

HONORS & AWARDS

2009.7 Outstanding Graduates, Outstanding Bachelor Degree Thesis, CUGB

2005.9-2009.7 Professional First-class Scholarship, CUGB(2 times)
Professional Second-class Scholarship, CUGB(4 times)

2012.7 Outstanding Graduates, Outstanding Master Degree Thesis, CUGB

2012.11-2016.11 Stipend from China Scholarship Council (CSC)

PUBLICATION & PATENTS

Biya Cai, J. Schwarzkopf, C. Feldt, J. Sellmann, T. Markurt, R. Wördenweber. Impact of Na_3NbO_4 nanoprecipitates on the conservation of strain and the giant thermal hysteretic ferroelectricity in strained NaNbO_3 films epitaxially grown on (110) NdGaO_3 . Submitted to *Phys. Rev. B*

Biya Cai, J. Schwarzkopf, E. Hollmann, D. Braun, M. Schmidbauer, T. Grellmann, R. Wördenweber. Electronic characterization of polar nanoregions in relaxor-type ferroelectric NaNbO_3 films. *Phys. Rev. B* 93, 224107 (2016), *IF* = 3.736

Biya. Cai, J. Schwarzkopf, E. Hollmann, M. Schmidbauer, M. O. Abdel-Hamed, and R. Wördenweber. Anisotropic ferroelectric properties of anisotropically strained epitaxial NaNbO_3 films. *J. Appl. Phys.* 115, 224103 (2014). *IF* = 2.18

R. Wördenweber, J. Schwarzkopf, E. Hollmann, A. Duk, **Biya. Cai**, M. Schmidbauer. Impact of compressive in-plane strain on the ferroelectric properties of epitaxial NaNbO_3 films on (110) NdGaO_3 . *Appl. Phys. Lett.* 103, 132908 (2013). *IF* = 3.3

Hongwen Ma, Shuangqing Su, Jing Yang, **Biya Cai**, Meitang Liu, Wengui Yao and Hui Peng. Preparation of potassium sulfate from K-feldspar by hydrothermal alkaline method: reaction principle and process evaluation. *CIESC Journal.* 65, 2363 (2014).

Jinhong Li, **Biya Cai**, Wuwei Feng, Yuqin Liu and Hongwen Ma, Investigations on phase constitution, mechanical properties and hydration kinetics of aluminous cements containing magnesium aluminate spinel. *Ceramics International.* 39, 8393 (2013). *IF* = 2.61

Shuangqing Su, Hongwen Ma, Jing Yang, **Biya Cai**, and Pan Zhang, Preparation of potassium sulfate from microcline powder. *Acta Mineralogica Sinica.* 33, 83 (2013).

Biya Cai, Jinhong Li, Hongwen Ma, Xiaoqian Jiang. Hydration kinetics of aluminate cement containing magnesium aluminate spinel. *Advanced Materials Research.* 295-297, 945(2011).

Biya Cai, Shuangqing Su, Hongwen Ma, and Meitang Liu, The preparation of potassium sulfate by sulfuric acid dissociation of kalsilite powder. *Chinese Society for Mineralogy, Petrology and Geochemistry Conference*, 2011

Biya Cai, Shuangqing Su, Hongwen Ma. Method for preparing industrial aluminum sulfate by using aluminum-silicon filter cakes left by extracting potassium from potassium feldspar. *Chinese Patent.* CN102583479 B, Dec. 3, 2014.

Hongwen Ma, Guoqing jin, Meitang Liu, Xiaoting Liu, Shituo Li, **Biya Cai**, Yanliang Cai, Huanzhong Cai. Technology for preparing potassium sulfate with potassium-rich mother liquid and phosphogypsum. *Chinese Patent.* CN102372292 B, Nov. 27, 2013.

Shuangqing Su, **Biya Cai**, Hongwen Ma, Zheng Luo, Meitang Liu. Technique for preparing agricultural potassium sulfate by utilizing kaliophilite powder. *Chinese Patent*. CN102167365 B, Apr. 10, 2013.

Shuangqing Su, **Biya Cai**, Hongwen Ma, Method for synthesizing 4A-type molecular sieve by utilizing aluminum-silicon tailings obtained in process of carrying out potassium extraction on potassium feldspar. *Chinese Patent*. CN102583429 A, Jul. 18, 2012.

CONFERENCE & SCHOOL

1. Oral presentation, International Winterschool on Bioelectronics 2013, Kleinwalsertal, Austria, 2013-03-13 to 2013-03-17
2. Oral presentation, International Workshop “Bioelectronics”, Kleinwalsertal, Austria, 2014-09-07 to 2014-09-13
3. Poster presentation, Deutsche Physikalische Gesellschaft (DPG) Spring Meeting of the Condensed Matter Division, Berlin, Germany, 2015-03-15 to 2015-03-20
4. Poster presentation, International School of Oxide Electronics 2015, Cargèse, France, 2015-10-12 to 2015-10-24

HOBBY

basketball, football, badminton